University of Southampton Research Repository

Thesis: Matthew Lee Hammond (2018) "Assessing Trends and Associated Uncertainties in Global Ocean Chlorophyll Using Bayesian Spatio-Temporal Techniques", University of Southampton, School of Ocean and Earth Science, PhD Thesis, pagination.

UNIVERSITY OF SOUTHAMPTON

FACULTY OF NATURAL AND ENVIRONMENT SCIENCES

Ocean and Earth Science

Volume 1 of 1

Assessing Trends and Associated Uncertainties in Global Ocean Chlorophyll Using Bayesian Spatio-Temporal Techniques

by

Matthew Lee Hammond

Thesis for the degree of Doctor of Philosophy

August 2018

UNIVERSITY OF SOUTHAMPTON

ABSTRACT

FACULTY OF NATURAL AND ENVIRONMENTAL SCIENCES

Ocean and Earth Science

Thesis for the degree of Doctor of Philosophy

ASSESSING TRENDS AND ASSOCIATED UNCERTAINTIES IN GLOBAL OCEAN CHLOROPHYLL USING BAYESIAN SPATIO-TEMPORAL TECHNIQUES

Matthew Lee Hammond

Climate change is predicted to affect oceanic phytoplankton abundance with impacts on fisheries and feedbacks on climate. The presence, magnitude, and even direction of long-term trends in phytoplankton abundance over the past few decades is still debated in the literature. The challenges affecting these studies include the low signal-to-noise ratio, the large degree of natural variability, and the shortness of the satellite ocean colour record, which is itself a composite of multiple shorter records. Previous work, however, has typically focused on using linear temporal models to determine the presence of trends in chlorophyll, where each grid cell is considered independently. To improve the assessment of trends a statistical model that explicitly models the relationship between neighbouring grid cells is used. A hierarchical Bayesian spatio-temporal model is fitted to global ocean colour data (1997 – 2013). This results in a notable improvement in accuracy in model fit, an order of magnitude smaller global trend, and larger uncertainty when compared to a model without spatial correlation. To help separate long-term trends from natural variability, trends from coupled physical-biogeochemical models are incorporated in to the model as Bayesian priors. The introduction of priors tends to reduce the magnitude and uncertainty of trend estimates, although the amount is deemed to be not statistically different from zero in any of the regions considered. Finally, the model is used to analyse the effect of taking into account discontinuities on estimated chlorophyll trends. The discontinuities considered are those relating to the launch and termination of individual ocean colour sensors. Considering discontinuities leads to statistically different trends in most regions, which can have a reversed sign as well as increased uncertainty. The improvement in trend estimate accuracy, and the more realistic representation of their uncertainty, emphasizes the solution that spatio-temporal modelling offers for studying global long-term change.

Table of Contents

Table of Tables

Table of Figures

Academic Thesis: Declaration of Authorship

I, ...

declare that this thesis and the work presented in it are my own and has been generated by me as the result of my own original research.

....

....

I confirm that:

1. This work was done wholly or mainly while in candidature for a research degree at this University;
2. Where any part of this thesis has previously been submitted for a degree or any other qualification at this University or any other institution, this has been clearly stated;
3. Where I have consulted the published work of others, this is always clearly attributed;
4. Where I have quoted from the work of others, the source is always given. With the exception of such quotations, this thesis is entirely my own work;
5. I have acknowledged all main sources of help;
6. Where the thesis is based on work done by myself jointly with others, I have made clear exactly what was done by others and what I have contributed myself;
7. Parts of this work have been published as: *Hammond, M. L., Beaulieu, C., Sahu, S. K., & Henson, S. A. (2017). Assessing trends and uncertainties in satellite-era ocean chlorophyll using space-time modeling. Global Biogeochemical Cycles, 31(7), 1103-1117. DOI: 10.1002/2016gb005600*
   And: *Hammond, M. L., Beaulieu, C., Henson, S. A., and Sahu S. K. (2018) Assessing the Presence of Discontinuities in the Ocean Color Satellite Record and Their Effects on Chlorophyll Trends and Their Uncertainties, Geophysical Research Letters, 45. DOI: 10.1029/2017GL076928.*

Signed: ....

Date: ....

Acknowledgements

I would like to thank all three of my supervisors: Claudie, Steph, and Sujit. Who have helped me tremendously these past three years and have developed me into the scientist I am today. Thank you Sujit for helping me wrap my head around the more complex parts of the theory. Thank you, Steph, especially for these final months where you went out of your way to help me get everything out of the door. Special thanks to Claudie for all her guidance, from the moment I arrived in Southampton, on making the most out of my life in science. My best wishes to Emil.

I'd also like to thank my parents who inspired and supported me all the way to the present. And finally, my thanks to Angela, your importance to me cannot be expressed in words.

Definitions and Abbreviations

CDOM – Coloured Dissolved Organic Matter

Chl – Chlorophyll-a Concentration

CMIP – Coupled Model Intercomparison Project

CPR – Continuous Plankton Recorder

CZCS – Coastal Zone Color Scanner

DMS – Dimethyl Sulphide

ENSO – El Niño Southern Oscillation

ESA – European Space Agency

GSM – Garver, Siegel, Maritorena Model

HDI – Highest Density Interval

IPCC – Intergovernmental Panel on Climate Change

M-scenario – MERIS/MODIS Discontinuity Scenario

MS-scenario – MERIS/MODIS & SeaWiFS Discontinuity Scenario

MSV-scenario – MERIS/MODIS & SeaWiFS & VIIRS Discontinuity Scenario

MV-scenario – MERIS/MODIS & VIIRS Discontinuity Scenario

MCMC – Markov Chain Monte Carlo

MERIS – Medium Resolution Imaging Spectrometer

MODIS – Moderate Resolution Imaging Spectroradiometer

N-scenario – No Discontinuity Scenario

NOAA – National Oceanic and Atmospheric Administration

NRMSE – Normalised Root Mean Square Error

OC-CCI – Ocean Colour Climate Change Initiative

PP – Primary Productivity

S-scenario – SeaWiFS Discontinuity Scenario

SeaWiFS – Sea-Viewing Wide Field-of-View Sensor

SST – Sea Surface Temperature

VIIRS – Visible Infrared Imaging Radiometer Suite

Chapter 1: Introduction

1.1 The Importance of Phytoplankton

Phytoplankton are microscopic photosynthetic plants that drift near the surface of oceans and other water bodies (Doney et al., 2006; Hays et al., 2005). In this study the focus is on oceanic phytoplankton which are near ubiquitous within the upper ocean and consist of thousands of species with their own ecological niches (Sournia et al., 1991). Phytoplankton growth depends on temperature, the availability of light, and the availability of nutrients, primarily nitrogen, phosphorous, and iron (Behrenfeld et al., 2006; Doney et al., 2006). Phytoplankton form the foundation of all marine ecosystems and their productivity represents approximately half of the global total primary production (PP) (Behrenfeld et al., 2001; Field et al., 1998), despite making up less than 1 % of the total photoautotrophic biomass on the planet (Bryant, 2003). The proxy chlorophyll-a concentration (chl) is used in studies of phytoplankton abundance, as it can be reliably measured from satellites (Gregg et al., 2003), and is considered an essential climate variable (Bojinski et al., 2014). This thesis will be concerned with estimating trends in chl which should allow better evaluation of the numerous potential impacts of changes in phytoplankton abundance.

Phytoplankton represent a bottom up control on the marine food web, and are mechanistically linked with fishery yield, thus any change in their distribution or abundance will have a strong effect on future marine fish stocks (Cheung et al., 2010; Friedland et al., 2012; Stock et al., 2017) (an example model projection can be found in Figure 1.1). This is particularly important in the most productive, overfished regions where bottom-up control predominates (Mcowen et al., 2015). In these regions trophic amplification can exaggerate small magnitude changes at base trophic levels, causing a greater impact on higher trophic levels (Cheung et al., 2010). Modelling studies of climate change predict a gradual global decrease in fish production capacity, although social and economic factors are also expected to be important (e.g. Galbraith et al., 2017). Climate change effects are also predicted to cause significant decreases in fish stocks at low latitudes, where many countries are dependent on the strength of their fisheries (Chassot et al., 2010; Cheung et al., 2010). These regions already have a low yield, by comparison to colder higher latitude ecosystems (Friedland et al., 2012). Two thirds of the countries with fisheries most vulnerable to climate change impacts are dependent on their domestic fisheries for fish supply (Ding et al., 2017). Due to the effects of phytoplankton abundance changes on marine resources, and thus on humanity, assessing long-term trends in chl should be considered a high priority.

Changes in phytoplankton abundance also have the potential to directly interact with climate, due to the capacity of phytoplankton to uptake CO_2 and, in certain species, to produce aerosols (Levasseur et al., 2013; López-Urrutia et al., 2006). Phytoplankton, via their role in the biological carbon pump, are considered a key determinant of atmospheric CO_2 concentrations on long time scales i.e. 1000s of years (Volk & Hoffert, 2013). The role of Phytoplankton in carbon cycling is to take up surface ocean inorganic carbon and biologically fix it during photosynthesis. A portion of this is then converted to dissolved organic carbon in the process of respiration. This biologically fixed carbon forms most of the particles that sink into the ocean interior, primarily from zooplankton feeding, excretion, and aggregation. This forms the soft-tissue biological pump, or carbon export production (Volk & Hoffert, 2013). Phytoplankton also comprise the main component of the hard-tissue biological pump, primarily from calcium carbonate production by coccolithophores, and their subsequent sinking into the ocean interior upon death (Sarmiento & Gruber, 2006). Difficulties directly measuring the export flux of organic matter make estimating the climate change impact on the biological pump challenging (Doney, 1999; Henson et al., 2011). Despite this, the general expectation is that in stratified nutrient limited areas, temperature induced increases in stratification will further increase nutrient limitation, reducing productivity and carbon export (Bopp et al., 2001; Bopp et al., 2013; Steinacher et al., 2009). Changes in phytoplankton species composition will also affect the biological pump. Increases in nutrient limitation can increase the abundance of smaller phytoplankton, as they are more efficient at taking up nutrients, when compared to larger phytoplankton (Moore et al., 2013; Vichi et al., 2011). These community shifts can modify the efficiency of carbon export, particularly of the hard carbon pump. All these contributing effects need to be considered to assess changes in the carbon cycle, but it is clearly important to have an accurate constraint on phytoplankton abundance changes.

1.2 Phytoplankton Global Controls

Climate change is expected to impact global phytoplankton abundance, and distribution, primarily through changes in temperature. Sea Surface Temperature (SST) changes will directly affect metabolic rates and, through changes in stratification, indirectly affect light and nutrient availability (Doney et al., 2006). SST is predicted to increase over both the near-term and long-term (e.g. Collins et al., 2013; Kirtman et al., 2013). Over the period 1970 - 2010 the top 75 m of the global ocean has increased in temperature at a rate of 0.11˚C per decade (Rhein et al., 2013). These changes are projected to continue in the future, with global temperature increases by the year 2100 estimated to be 1.5 – 5.0˚C, relative to pre-industrial times (Rogelj et al., 2012). Climate change is also predicted to affect wind and ocean circulation across the globe (e.g. England et al., 2014; Moore et al., 2015), with further potential impacts on phytoplankton abundance.

Changes in the degree of stratification are expected to be the primary mechanistic route leading to changes in phytoplankton. Stratification is controlled by buoyancy forcing (i.e. due to changing heat and freshwater fluxes) and surface winds, and can affect phytoplankton abundance by controlling the availability of solar irradiance and nutrients (Figure 1.2) (Doney, 2006; Durack et al., 2012). Light is attenuated exponentially within the water column and thus increased stratification will increase available irradiance. However, if the mixed layer is too deep light levels may be insufficient to sustain photosynthesis, as occurs seasonally in high latitude regions (Doney, 2006). Conversely, a weak density gradient between surface and depth, associated with low stratification, can increase nutrient supply (Behrenfeld et al., 2006). Thus, future warming could either positively or negatively affect phytoplankton abundance depending on the limiting factor in that region. In regions where nutrients are already limited, an increase in stratification will decrease nutrient supply to the surface ocean, increasing nutrient stress for phytoplankton (Bopp et al., 2001). In regions where light is limiting an increase in the quantity of phytoplankton is expected, as more stratified waters keep phytoplankton closer to the surface, increasing light availability (Doney, 2006). These controls show a broadly latitudinal dependence, where lower latitudes tend to be nutrient limited and high latitudes are light limited. This is likely to result in a latitudinal pattern in phytoplankton abundance changes, with decreases in phytoplankton towards the equator and increases at high latitudes, although it remains to be determined whether the expected changes can be observed.

Phytoplankton are unicellular and unable to regulate their temperature, making them particularly sensitive to temperature changes affecting biological rates, including enzyme reactions (e.g. Eppley, 1972; Grimaud et al., 2017). It has been shown that light-limited growth, light-saturated growth, and the optimal irradiance for growth are all highly sensitive to temperature (Edwards et al., 2016). SST increases this century could cause poleward shifts in species and decrease species diversity, as high temperatures may limit growth (Boatman et al., 2017; Thomas et al., 2012). Like SST driven changes in stratification, SST impacts on growth could result in a latitudinal pattern in phytoplankton abundance changes which is currently poorly understood.

1.3 Trends in Observational and Modelling Studies

Observational data allow studies of the abundance and distribution of phytoplankton as well as how these are changing. Of the observational data types, the large spatial coverage and temporal resolution of ocean colour satellite records make them one of the best approaches to understanding the current climate effects on global phytoplankton abundance (e.g. McClain, 2009; Siegel et al., 2013). In situ data are also available although they are much sparser, temporally and spatially. The availability of satellite data means many studies have been conducted, however there does not appear to be any consensus on the nature of a global trend in phytoplankton abundance. Using data from Coastal Zone Colour Scanner (CZCS) (1979 - 1986) and Sea-Viewing Wide Field-of-View Sensor (SeaWiFS) (1998 - 2002), a positive global average trend was reported by Antoine et al. (2005). Using solely SeaWiFS data Behrenfeld et al. (2006) (data from 1997 - 2006) and Vantrepotte & Mélin (2011) (data from 1997 - 2007) found an overall decrease in chl and PP. Studies considering temporal correlation in their statistical analyses show either a low magnitude positive trend or that no global trend can yet be distinguished from noise; the following four studies are examples of such. A low magnitude global positive trend was reported by Saulquin et al. (2013) with data from SeaWiFS (September 1997 - December 2010) and Medium Resolution Imaging Spectrometer (MERIS) (April 2002 - April 2012). A similar trend was found by Gregg & Rousseaux (2014) using data covering 1998 - 2012 from SeaWiFS and Moderate Resolution Imaging Spectroradiometer (MODIS), although an updated study (1998 - 2015) found no significant trend (Gregg et al., 2017). Using SeaWiFS data (September 1997 - December 2008) and a more robust statistical analysis Beaulieu et al. (2013) show that no global trend can be distinguished from noise.

More consensus has been reached in studies of ocean colour trends in certain regions. The best example of this is in the subtropical gyres which represent the largest oceanic ecosystem despite having a lower than average productivity (McClain et al., 2004). Multiple studies, using data from the SeaWiFS instrument, support an expansion of these regions over time (Irwin & Oliver, 2009; Polovina et al., 2008; Vantrepotte & Mélin, 2011). However, there is disagreement over whether this expansion is happening at an increasing or decreasing rate. Decreases in chl have also been reported in most oligotrophic gyres by Signorini et al. (2015) using data from the SeaWiFS and MODIS sensors. However, in a study using in situ data, Saba et al. (2010) reported an increase in PP at sites in both the North Pacific and North Atlantic subtropical gyres of 2 % yr^{-1} between 1989 and 2007. Whilst there appears to be some degree of consensus in these regions it is clear that more work needs to be done globally to improve the understanding of trends.

In situ data records can be substantially longer than satellite records, allowing the analysis of trends over a longer timescale. A study of compiled historical (1899 - 2000) in situ ocean transparency data by Boyce et al. (2010) showed a large decline of ~1 % yr^{-1}. However, the lack of uniformity in the collection techniques and the extreme degree of decline has led to criticism of this work (e.g. Rykaczewski & Dunne, 2011; Siegel et al., 2013). These criticisms were subsequently addressed with very similar results (Boyce et al., 2014). Wernand et al. (2013) used historical observations of the Forel-Ule scale (a discrete semi-quantitative scale describing the greenness of the ocean) to reconstruct, in combination with a radiative transfer model, ocean surface chl over the period 1889 - 1999. Their analysis did not reveal a global trend over this period, although they did note several regional trends with increases in the Atlantic Ocean, and decreases in the Indian Ocean and in the Pacific.

Biogeochemical models can be used to project future phytoplankton abundance trends as a response to climate change, as well as to confirm historical trends. Many biogeochemical model studies focus on PP, rather than specifically phytoplankton abundance. A hindcast (1960 - 2006) simulation, using prescribed atmospheric forcing, by Laufkötter et al. (2013) showed a PP decrease of 6.5 %. Modelling projections of future changes until 2100, each with different marine ecosystems parameterizations, have shown PP decreases of 2 - 20 % (Steinacher et al., 2010), 8.6 ± 7.9 % (Figure 1.3) (Bopp et al., 2013), and 2 - 16 % (Fu et al., 2015). Such projections have also shown little consistency in the sign of the predicted changes (Laufkötter et al., 2015). Other modelling approaches have been used, including an empirical model directly linking climate indicators and phytoplankton changes which showed a 0.7 - 8.1 % increase in global PP, over the 190 years preceding 2050 (Sarmiento et al., 2004). It should be noted that all these model projections show considerable regional variability, where trends in individual regions may be the opposite direction to the global trend, as well as variability between specific phytoplankton functional types (e.g. Krumhardt et al., 2017). Despite this high degree of variability, most studies do suggest some degree of decline in PP. Constraining changes in observations should help us understand climate change impacts on phytoplankton abundance and allow for reduced uncertainty in climate projections.

1.4 Challenges in Chl Trend Detection

The ability to determine trends in phytoplankton abundance is hampered by many inherent observational difficulties. These problems include the short record length, the low signal-to-noise ratio, the presence of gaps in the data, and the large degree of natural variability on seasonal to decadal timescales inherent in chl (e.g. Beaulieu et al. 2013; Henson et al., 2010; Mélin, 2016; Saulquin et al., 2013). Interannual variability represents interactions within the climate system, i.e. those not directly caused by outside forcing. Examples that affect large regions of the globe include: ENSO (El Niño Southern Oscillation), the Pacific Decadal Oscillation, and the North Atlantic Oscillation (Ducklow et al., 2009). These systems themselves may also undergo changes under climate change, including in intensity, frequency, or a permanent shift to one phase (Christensen et al., 2013). Seasonal variability in phytoplankton arises from changes in light and nutrient availability, and zooplankton abundance, primarily resulting from changes in solar irradiation throughout the year. The amplitude of variability in solar irradiation, and thus phytoplankton abundance, increases away from the equator. Seasonal variability has been shown in many cases, particularly at high latitudes, to dominate over other variations and trends (Dandonneau et al., 2004).

These difficulties mean that producing an analysis based solely on data from one ocean colour sensor is hampered by the short lifespan of sensors. Any trends using the data from a single sensor cannot necessarily be attributed to climate change, as they may have incorporated part of the decadal variability signal (Hawkins & Sutton, 2012). It has been suggested that an average record length of 31.5 years is required to distinguish a climate change driven chl trend from natural variability, due to the large magnitude of natural variability and relatively weak trends (Figure 1.4) (Henson et al., 2010; 2016). Boyce & Worm (2015) found that published phytoplankton abundance trends showed less variability and a lower magnitude when estimated from longer records. A further issue with the use of ocean colour data is that the start of the current multi-sensor period (i.e. from the launch of SeaWiFS) includes a particularly strong El Niño event in 1997/1998. This produced a strong bias in trends detected over this period, as seen by comparison with the MERIS dataset (Saulquin et al., 2013).

Multi-sensor datasets can be used to compensate for the relative shortness of individual ocean colour sensors. Multi-sensor datasets use various methods to combine the available ocean colour sensors into a single record (e.g. Lavender et al., 2015; Maritorena & Siegel, 2005; Saulquin et al., 2013). The four main ocean colour sensors commonly used to create such records are: SeaWiFS (September 1997 - December 2010), MERIS (April 2002 - April 2012), MODIS (July 2002 - present), and Visible Infrared Imaging Radiometer Suite (VIIRS) (Jan 2012 - present). However, if the spatially and temporally varying differences between datasets are not accounted for they can bias and/or increase uncertainty of trend estimates (Djavidnia et al., 2010; Gregg & Casey, 2010). The maximum available length of multi-sensor chl records is currently approximately 20 years.

In summary, it is hard to determine global trends in phytoplankton abundance given the large natural variability, low trend magnitude, and lack of consistent long-term observations. While there is more agreement between studies of individual regions, they still suffer from the same problems. The fact that observational studies are mostly limited to satellite data, and the short record length that these inherently entail, means that it is difficult to distinguish any trend from interannual variability with certainty. This thesis will concern using more rigorous statistical techniques than employed thus far in order to improve this assessment.

1.5 Interpretation of Chlorophyll Trends

Additional problems lie in the interpretation of chl trends. Ocean colour derived chl is assumed to be a proxy of phytoplankton biomass, and thus trends in chlorophyll are often taken to directly represent trends in phytoplankton biomass. There are two potential issues in this interpretation: first that chl trends may instead be representing changes in phytoplankton physiology rather than biomass and second that ocean colour chl trends ignore sub-surface changes.

Changes in phytoplankton physiology, particularly changes in intracellular pigmentation, may lead to chl trends that are independent of changes in phytoplankton abundance/biomass. A recent study has suggested that the effect of photo-acclimation under changing light conditions, related to stratification, is significant (Behrenfeld et al., 2016). Although this effect remains to be fully quantified globally it should still be considered in the interpretation of chl trends.

Additionally, satellite data inherently only detects near surface phytoplankton populations, meaning any changes at depth are likely to be obscured. Saba et al. (2010) show that at two sites within subtropical gyres the vast majority of chl change is occurring below the surface. At these sites ocean colour data sets consistently underestimate chl changes when compared to in situ data. This effect is particularly strong in these regions due to the relationship between chlorophyll changes and deeper physical dynamics (Saba et al., 2010). It is possible that a similar effect may be occurring in other ocean regions with similar physical controls.

When interpreting trends in ocean colour chl they must not be directly inferred as changes in phytoplankton abundance or biomass. Instead they should be interpreted with the consideration of changes in phytoplankton physiology and in the sub-surface ocean.

1.6 The Opportunity Offered by Spatio-temporal Statistical Models

Much of the previous work on chl trends, including most of those listed in Section 1.3, use simple linear temporal models that do not effectively use all the information provided by observations. Specifically, most of these estimates of chl trends have been based on analysis at the level of individual grid cells, or bulk averages within predefined regions, ignoring the spatial relationship within the data during the analysis. Any observation taken with a spatial (or temporal component) like most geographical data, or nearly all remotely sensed data, exhibit relationships in the data based on the closeness of data points in space (or time). Data points that are close in space (or time) are more similar than those further apart; ignoring this fact and assuming they are independent should be avoided, as it provides an unrealistic simplifying assumption (Cressie & Wikle, 2011; Wikle, 1998). In most time-series analysis, the temporal relationship is usually considered as a form of temporal autoregression. However, spatial correlation has not been previously used, to my knowledge, in the analysis of chl trends. Including this feature in a statistical analysis offers the potential to improve detection power by borrowing strength from neighbouring observations (Chandler & Scott, 2011). Traditionally these techniques have not been widely used due to their computational demands when considering large datasets, although this ability is now available (Banerjee et al., 2008; Sahu & Bakar, 2012). Spatio-temporal models have been applied more widely in studies of air pollution and its effects, although not in the analysis of chl data (e.g. Rushworth et al., 2014; Sahu & Bakar, 2012). In more general terms an analysis of chl that considers spatial correlation would likely better reflect the physical reality, where chl evolves in a spatially and temporally correlated fashion, improving long-term trend estimates and assessments of their uncertainty. Therefore, this study focuses on assessing the probabilities of long-term trends in satellite ocean chl time-series using a Bayesian hierarchical spatio-temporal approach allowing spatial correlation to be considered. By using the Bayesian spatio-temporal model an improvement in the accuracy of chl trend estimates is expected, alongside a more complete account of their uncertainty.

1.7 Structure of the Following Work

The structure of the remaining body of work is as follows. Chapter 2 details the data and hierarchical Bayesian spatio-temporal model used. Chapter 3 details the analysis of trends in global chl data using the hierarchical Bayesian spatio-temporal model and compares this to a similar model without spatial correlation terms. Chapter 4 investigates using information from coupled physical-biogeochemical models to improve trend estimation, by using multiple sources, again within a hierarchical Bayesian spatio-temporal model framework. Chapter 5 details an analysis using this statistical framework to assess the effect of taking discontinuities into account when analysing chl trends in multi-sensor satellite records. In Chapter 6 a summary is made of all the preceding work, summarizing the findings, highlighting their implications, and finally making suggestions about how this work can be built upon in the future.

Chapters 3 - 5 are written as independent, but related works, that have been, or are written to be, released in scientific journals. As such there may be some degree of overlap between the introductions, methods, and conclusions in these works and those of the overall thesis. All references have been compiled at the end of the thesis.

1.8 Figures

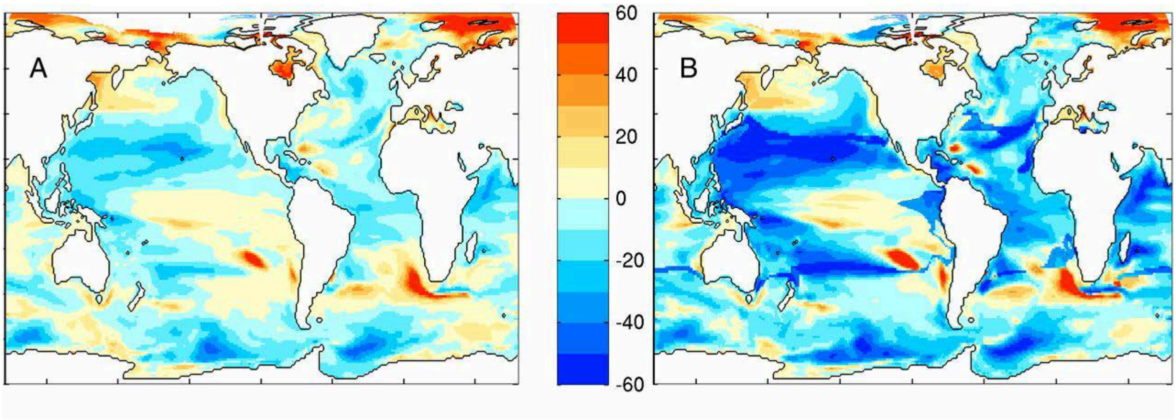

Figure 1.1 Projected percentage changes between 1951 - 2000 and 2051 - 2100 in (a) net primary productivity and (b) fish catch potential under an RCP8.5 scenario. Note that fish catch potential changes are coincident but larger than changes in net primary productivity (Source: Stock et al., 2017)

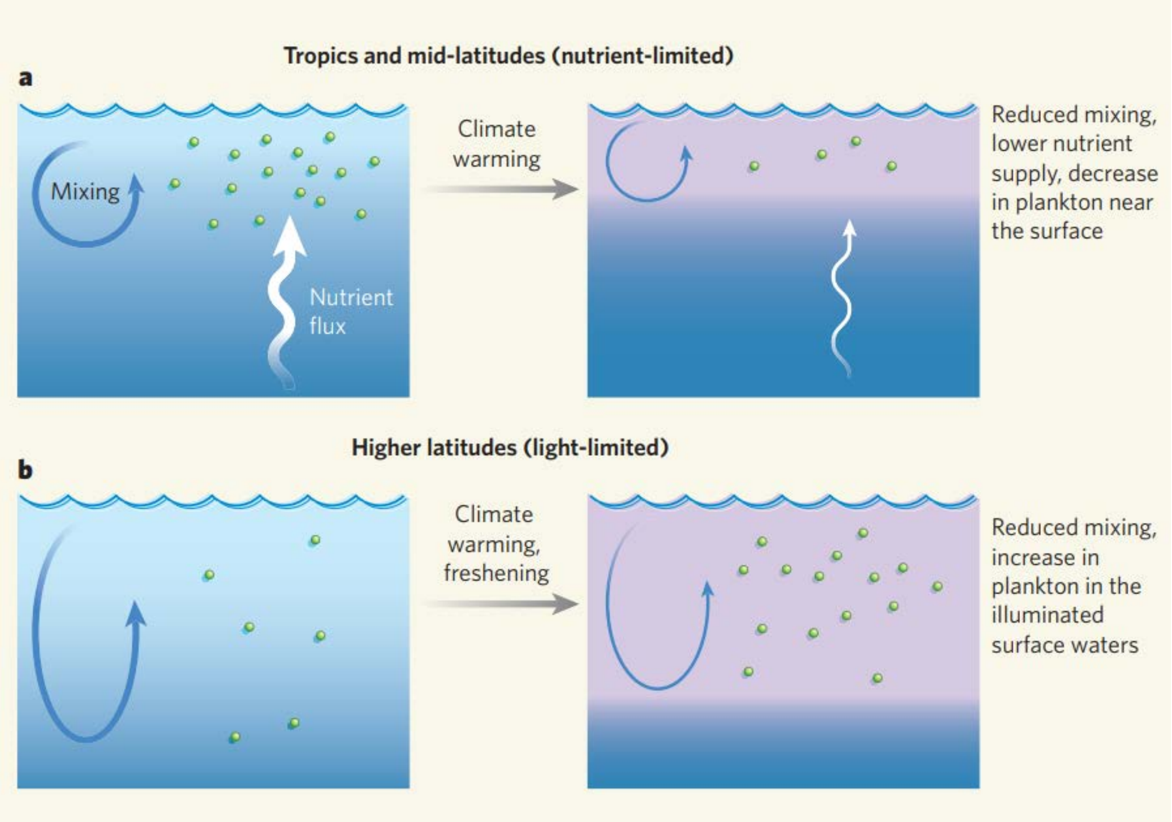

Figure 1.2 The predicted response of phytoplankton to a warming-induced increase in stratification. (a) increased stratification in nutrient limited low latitude regions is expected to reduce nutrient supply, decreasing phytoplankton abundance. (b) increased stratification in light limited high latitude regions is expected to alleviate light limitation and increase phytoplankton abundance. (Source: Doney, 2006)

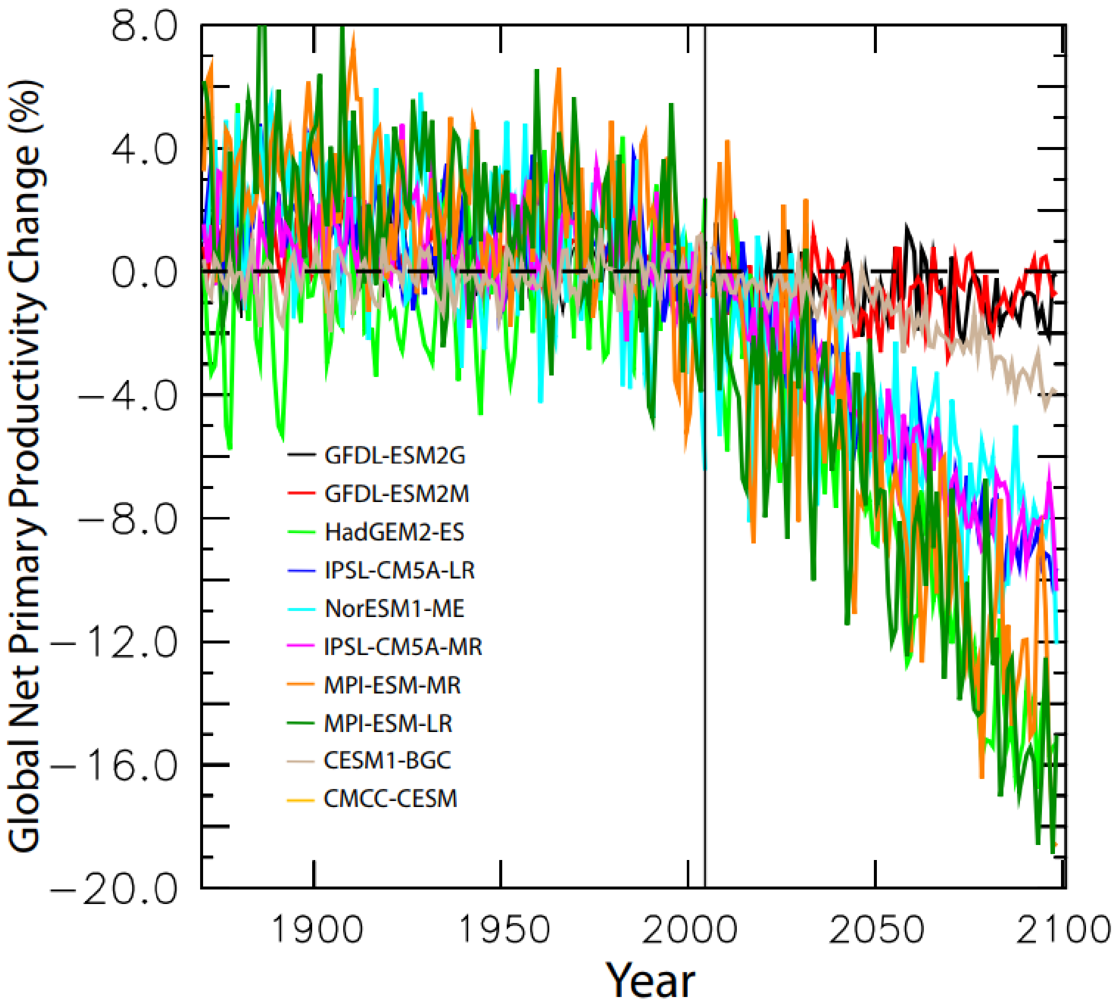

Figure 1.3 Time-series of global net primary productivity in 10 CMIP5 model simulations covering 1870 - 2100 using historical and RCP8.5 simulations, showing the large uncertainty in projections of net primary productivity. (Source: Bopp et al., 2013)

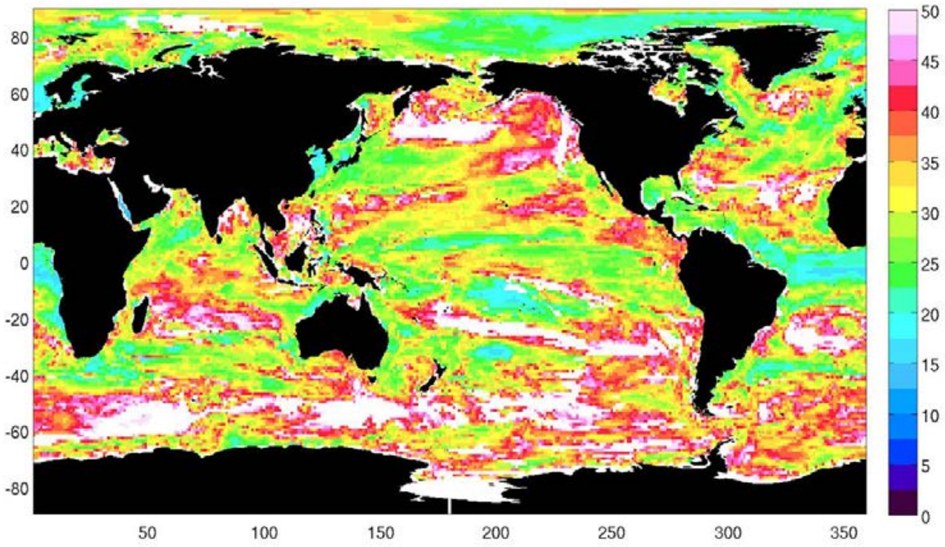

Figure 1.4 The number of years of data required to distinguish a climate change driven chl trend from natural variability. White areas indicate that less than half of the models used agree on the sign of trend. (Source: Henson et al., 2016)

Chapter 2: Materials & Methods

2.1 Data

The chl data in Chapter 3 are sourced from the ESA OC-CCI v2.0 dataset (Lavender et al., 2015; available at: http://www.esa-oceancolour-cci.org/). This dataset combines data from the SeaWiFS, MERIS, and MODIS sensors to create a continuous, bias-corrected time-series running from September 1997 - December 2013 inclusive. The chl data in Chapters 4 & 5 are sourced from the ESA OC-CCI v3.1 dataset (likewise available at: http://www.esa-oceancolour-cci.org/). Figure 2.1a shows the different time-series for the two datasets. The v2.0 dataset shows higher chl values before the introduction of the MERIS and MODIS sensors and lower values afterwards. The v3.1 dataset uses additional data from MERIS, MODIS, and Visible Infrared Imaging Radiometer Suite (VIIRS) to extend the time-series up to and including December 2016, alongside updates to calibration, algorithms, and the bias-correction method (Grant et al., 2017). The ESA project uses band-shifting and bias-correction techniques to combine data from the individual sensors. Each ocean colour sensor detects a different set of wavelengths or “bands”, band-shifting refers to methods to match bands between different ocean colour sensors, in ESA OC-CCI this is done using a bio-optical model inversion (Mélin & Sclep, 2012; 2015). Bias-correction is used to remove gross differences between sensors, including: radiometric sensor technical specifications, calibration strategies, and algorithms (used to converted water-leaving radiances to chl values). In the ESA OC-CCI dataset bias-correction is performed by adjusting radiances at the pixel level to reduce the difference between SeaWiFS and the other sensors; a time window with increased central weight is used to correct seasonal biases (Chuprin et al., 2017; Djavidnia et al., 2010; Grant et al., 2017).

For this study further data treatment is also used. First the ESA OC-CCI dataset is downscaled from a 1/24° grid to a 1° grid by averaging within 1° boxes. Each box contains a total of 576 (i.e. 24 x 24) grid cells centred on the points of the 1° grid, thus a maximum of 576 points will be averaged from the original dataset to create a grid cell in the downscaled dataset. This is a maximum as some grid cells in the original dataset will contain no data, most typically around areas of high cloud coverage such as high latitudes and equatorial regions (see Figure 2.2). Additionally, grid cells near land use a reduced number of the original dataset grid cells. This occurs primarily around islands as coastal data is not used in this analysis (see below), as well as some continental areas which are sufficiently close to the non-coastal regions. Downscaling is used to match the grid spacing of the SST dataset (see below) and to prevent the dataset being too large to be computed. The effect of this downscaling on the analysis is assessed in Figure 2.3 and below in Section 2.2. Chl values have a log-normal distribution, i.e. after a log-transformation chl data show a normal distribution (Campbell, 1995). Therefore after downscaling, the chl data are log-transformed, which should allow more accurate estimation of chl values by the statistical model (Section 2.2).

The ESA OC-CCI v3.1 dataset does contain missing values even after the downscaling process and using monthly average values. These seem to be primarily focused in high latitude regions, with a smaller proportion in the eastern equatorial Atlantic. In Northern high-latitudes the grid-cell maximum missing data is 18 %, in Southern high-latitudes the maximum is 28 %. The cause for this missing data is likely attributable to persistent cloud cover in winter. The reader should refer to Section 2.2 which includes details of how the model handles missing data.

The ESA OC-CCI project also characterises the uncertainty and bias of their chl estimates within 14 optical water classes by deviation from matched in situ observations (Grant et al., 2017). The average deviation, log-transformed, for the v3.1 dataset is 0.17 mg m^{-3}, whilst the average bias, again log-transformed, is 0.0035 mg m^{-3}. Whilst the bias may be considered negligible, the average deviation is quite large, which could be attributed to the sparsity of in situ matchups. The deviation does show seasonal variations on the order of 0.005 mg m^{-3} but no longer-term variation, which would have the potential to affect trend estimates.

Biogeochemical model output, used in Chapter 4, comes from the IPCC Coupled Model Intercomparison Project (CMIP5) models (sourced from https://esgf-node.llnl.gov/projects/cmip5/). Models and ensembles with monthly chl output run under the RCP8.5 (2006 - 2100) and historical (1860 - 2005) scenarios were used (see Table 2.1 for full details of the models used). The RCP8.5 scenario represents a high emissions scenario where radiative forcing is approximately 8.5 Wm^{-2} in the year 2100 (Taylor et al., 2012). The historical scenario is a run covering the period 1850 - 2005 with imposed forcings (including atmosphere, solar, and land use) based on observations (Taylor et al., 2012). RCP8.5 and historical outputs are combined, then data outside the period 1979 - 2033 is omitted. This provides a continuous dataset centring on the period of continuous ocean colour observations but with additional length either side (the selected period is three times the total length of the ocean colour record) to help isolate interannual variability. Models may use different poles, variable grid spacing, or other grid distortions, the model grid outputs were thus interpolated to match the 1° grid spacing used in the satellite data (Bopp et al., 2013; Giorgetta et al., 2013). The chl data values are lognormal transformed as in the observational datasets.

In Chapter 5, the analysis is also performed on data from the GlobColour dataset (available at: http://globcolour.info/) to act as a comparison to the results from the ESA OC-CCI dataset. Figure 2.1b shows the different time-series for the two datasets. The ESA OC-CCI v3.1 typically shows lower values of chl than the GlobColour dataset, particularly in the post-2012 period which may be associated with the introduction of the VIIRS sensor. The differences between the two datasets likely arise from the different merging processes used. The GlobColour dataset, like the ESA OC-CCI v3.1 dataset merges data from the SeaWiFS, MERIS, MODIS, and VIIRS sensors. Unlike the ESA OC-CCI dataset, the GlobColour dataset merges the individual sensors using the Garver, Siegel, Maritorena Model (GSM) process, without any explicit bias correction (Maritorena & Siegel, 2005; Maritorena et al., 2002; Maritorena et al., 2010). The GSM process combines a semi-analytical model and the water-leaving radiance observations, i.e. the observations directly made by ocean colour sensors. The normalised water-leaving radiances, from the individual sensors, are combined into a multi-source spectrum for each pixel. The multi-source spectrum is then inverted with a semi-analytical ocean colour model, which describes the relationship between these water-leaving radiances and inherent optical properties of seawater, including backscattering and absorption coefficients (Maritorena et al., 2002; 2010). Case 1 (open ocean) data are used as coastal regions are not considered (see below). Like the ESA OC-CCI data, GlobColour chl values are lognormal transformed.

SST is included as a covariate (see details in Section 2.2). SST data are sourced from the NOAA optimum interpolation v2 data product, which is provided on a 1° grid (Reynolds et al., 2002; available at: http://www.esrl.noaa.gov/psd/data/gridded/data.noaa.oisst.v2.html). In addition, Chapter 4 uses SST output from the same CMIP5 models as above, interpolated to match the 1° grid spacing of the satellite data, to act as a covariate for modelled chl. All of the datasets used are provided as monthly means.

The data are separated into 54 biogeochemical provinces, as defined by Longhurst (1995; 1998) according to characteristic biogeochemical factors and physical forcings. Coastal and polar waters, as defined in Longhurst (1998), are excluded from this analysis due to issues with the availability and quality of data. Ocean colour data in coastal regions have poorer data quality due to contamination by atmospheric dust and sulphates, from continental sources, as well as other constituents in the water column; these contaminants are challenging to compensate for as they vary independently of chl (Hyde et al., 2007; Mélin et al., 2007; Schollaert et al., 2003). In polar regions there is a high proportion of missing data primarily due to cloud and ice cover; cloud has increased over recent years and can cover up to 90 % of the sky (Bélanger et al., 2013). Polar regions also have lower data quality due to large quantities of coloured dissolved organic matter (CDOM) in river runoff and low solar angles (Lewis et al., 2016). After removing coastal and polar regions, 23 regions are used in the following analysis (see Table 2.2 which lists the province names and reference numbers).

A clustering approach based on Devred et al. (2007) was briefly explored, to more directly assess region boundaries based on the data. This method used SST, chl, latitude, longitude, and depth values in a K-means clustering analysis to define regions in the North West Atlantic. However, this approach was not carried forward in to the main analysis as the Longhurst technique is more widely established, and as the focus was on understanding the effect of spatial correlation terms within a Bayesian spatio-temporal model, the more complex clustering approach would have had only limited impact on the results. Additionally, there were concerns about directly basing provinces on the same parameters used in the trend analysis, see Section 3.5.4 for a fully detailed analysis of the region selection.

2.2 Methods

2.2.1 Regression Model

A hierarchical Bayesian spatio-temporal model is fitted to chl data in each of the remaining 23 Longhurst regions. The model structure is outlined below (see Table 2.3 for a list of all parameter definitions) and in the representative diagram, Figure 2.4. In the first level, the relationship between true and observed chl is described:

$$Z_{n,t} = O_{n,t} + \varepsilon_{n,t} \qquad (1)$$

where $Z_{n,t}$ is the observed chl at location n and at month t. The observed valued is composed of the corresponding true chl value $O_{n,t}$, and a white noise process $\varepsilon_{n,t}$ which represents random measurement error. This error is assumed to be independently normally distributed with a zero mean and unknown pure error variance: σ_ε^2, i.e. $\varepsilon_{1,t}, \dots, \varepsilon_{N,t} \sim \left(N(\mathbf{0}, \sigma_\varepsilon^2 \boldsymbol{I}_n)\right)$ for all t. The true chl value is assumed to follow the regression model:

$$O_{n,t} = \boldsymbol{x}'_{n,t}\boldsymbol{\beta} + \boldsymbol{a}'_n \boldsymbol{w}_t \qquad (2)$$

composed of the covariates (including intercept) $\boldsymbol{x}_{n,t}$, the regression coefficients $\boldsymbol{\beta} = (\beta_0, \beta_{Trend}, \beta_{SST}, \beta_{M1}, \dots, \beta_{M12})$, and the term $\boldsymbol{a}'_n \boldsymbol{w}_t$ representing spatial and temporal correlation, calculated in the second level (defined in detail below). The covariates include time, month (represented as factor levels whereby each month of the year has its own constant that is added or subtracted from all years), and SST. Time represents the temporal trend, the monthly factor is used to isolate the seasonal cycle, and SST is included due to its strong influence on chl variability (e.g. Behrenfeld et al., 2006, Martinez et al., 2009). The regression coefficients correspond to the covariates as follows: β_0 to the intercept, β_{Trend} to the trend, β_{SST} to SST, and $\beta_{M1}, \dots, \beta_{M12}$ to the monthly factor levels. This is a linear model, a valid assumption for the trend here, as chl trends are expected to be small over this timescale, particularly compared to environmental variability (see Appendix A.3). Chapter 5 explores using an additional covariate to account for discontinuities in the multi-sensor record. Note that the monthly factor is not included in the Pacific Subarctic Gyres Province (East) (Region 18) in Chapters 4 & 5 (i.e. for the ESA OC-CCI v3.1 dataset).

2.2.2 Monthly Factor in the Pacific Subarctic Gyres Province (West)

During testing the model was found to produce anomalous results in the Pacific Subarctic Gyres Province (West) (Region 18) when using the ESA OC-CCI v3.1 dataset. In order to resolve this the monthly factor was omitted in this region when using the ESA OC-CCI v3.1 dataset only. This is expected to lead to a small decrease in model fit accuracy in this region. This region appears to be problematic due to shifting phenology over the study period. In this region, unlike others, the month with peak chl seems to favour either the summer, autumn, or winter, and seems to oscillate between these, depending on year (Figure 2.5). Modelling this region with a seasonal cycle constant for all years leads to a large error in the fit and thus to anomalous results. However, this does not appear to affect the results of Chapters 4 & 5 in the other regions.

2.2.3 Gaussian Predictive Process

In the second level of the hierarchical Bayesian model, a Gaussian Predictive Process type model is used to calculate the spatio-temporal random effects. This process type is used as it allows improved computational speed when applied to large spatio-temporal datasets, as used in this study (Banerjee et al., 2008; Finley et al., 2009; Sahu & Bakar, 2012). This model type calculates the spatio-temporal process (random effects) $\boldsymbol{\eta}_t$ at the knot sites, a subset $\boldsymbol{m}$ of the observation locations $\boldsymbol{n}$, to provide the reduced set of random effects $\boldsymbol{w}_t$.

2.2.4 Spatio-Temporal Random Effects

Model-based kriging is used after each inversion in order to expand the reduced spatial covariance matrix to the complete set of observation locations. The process for this is as follows. First, the model is fitted at the knot locations and then the model is used to predict at a new location, i.e. one of the original observation sites, using Bayesian rules. Here, the regression coefficients and the spatio-temporal effect are unknown and are sampled using MCMC. The spatio-temporal effect is calculated at the observation location by applying kriging, specified with a joint distribution for the spatio-temporal effect at all observation locations. The kriging requires evaluation of the conditional expectation of the predicted observation location based on all the other locations. This conditional expectation is incorporated in to the prediction model with unknown parameters replaced by MCMC iterations. The observation location is then sampled at each iteration by using the MCMC values of the parameters. Finally, averaging of the MCMC samples of the observation site are used in order to obtain point and interval estimates.

The spatio-temporal random effects between the knot and observation locations are given by $\boldsymbol{a}_n'\boldsymbol{w}_t$ where $\boldsymbol{a}_n'$ is:

$$\boldsymbol{a}_n' = \boldsymbol{C}_n'\boldsymbol{S}_w^{-1} \tag{3}$$

where $\boldsymbol{C}_n'$ is the correlation vector of the spatial random effects between the $\boldsymbol{n}$ observation locations and the $\boldsymbol{m}$ knot locations, and $\boldsymbol{S}_w$ is the correlation matrix of the reduced set of random effects ($\boldsymbol{w}_t$).

The random effects, specified at the knot sites, are expressed as:

$$\boldsymbol{w}_t = \rho\boldsymbol{w}_{t-1} + \boldsymbol{\gamma}_t \tag{4}$$

where $\boldsymbol{w}_{t-1}$ are the random effects in the month immediately prior to t, ρ is the unknown autoregressive term assumed to be in the interval (-1,1), and $\boldsymbol{\gamma}_t$ is the M dimensional Gaussian process: $N(\boldsymbol{0}, \boldsymbol{\Sigma}_{\mathrm{w}})$, where $\boldsymbol{\Sigma}_{\mathrm{w}} = \sigma_{\mathrm{w}}^2\boldsymbol{S}_{\mathrm{w}}$ (σ_{w}^2 is the site invariant spatial variance). The initial condition $\boldsymbol{w}_0 \sim N(0, \sigma_0^2\,\mathrm{S}_0)$ completes the auto-regressive model (Equation 4).

Knot sites are defined on an equally spaced grid, with a separation of 4.5°, based on a compromise between speed and accuracy. Due to the variety of biogeochemical province shapes, grid points lying outside the region are removed. This leaves a near constant ratio between number of observations and knot sites in each region, leading to a constant effect on model fit between regions.

The correlation matrix $\boldsymbol{S}_{\mathrm{w}}$ is obtained using the Matérn correlation function (Handcock & Stein, 1993; Handcock & Wallis, 1994):

$$\kappa(n_i, n_j; \Phi, \nu) = \frac{1}{2^{\nu-1}\Gamma(\nu)}\left(2\sqrt{\nu}\|n_i - n_j\|\Phi\right)^{\nu} K_{\nu}\left(2\sqrt{\nu}\|n_i - n_j\|\Phi\right), \qquad \Phi > 0, \nu > 0 \tag{5}$$

where $\Gamma(\nu)$ is the standard gamma function, K_ν is the modified Bessel function (second kind) with order ν, and $\|n_i - n_j\|$ is the distance between two sites n_i and n_j. The parameter ν represents smoothness of the random field, and is assigned a value of 0.5, representing an exponential covariance function. The decay parameter Φ controls how correlation decays as the distance between two sites becomes larger and is assigned a value based on testing. To determine the ideal value of Φ, a range of different values are tested in a small subset of regions. Selection is based on removing 10 % of the data prior to fitting the model and then comparing fitted and observed values, for the removed 10 %, with the metric Normalised Root Mean Square Error (NRMSE).

$$NRMSE = \frac{\sqrt{\frac{\sum_{n=1}^{N}\sum_{t=1}^{T}\left(\hat{O}_{n,t} - Z_{n,t}\right)^2}{NT}}}{\bar{Z}} \qquad (6)$$

The selected test regions are the North Atlantic Subtropical Gyre Province (East) (Region 14), the North Pacific Tropical Gyre Province (6), and the Tasman Sea Province (Region 23), which cover a range of region sizes. An optimum value of Φ is then selected based on a compromise between model fit and computational speed. This selection process results in an optimum value of $\Phi = 2 \times 10^{-3}$, representing spatial correlation becoming negligible after approximately 1500 km. In the Western Tropical Atlantic Province (Region 10), when using the ESA OC-CCI v2.0 dataset in Chapter 3, a value of $\Phi = 2.1 \times 10^{-3}$ is used, due to issues with convergence of the MCMC algorithm, this is not expected to have a large effect on the model fit (see Figure 2.3).

The importance of original data resolution on the spatial correlation decay parameter (Φ) and model fit are shown in Figure 2.3. Two datasets in the Tasman Sea Province (Region 23) were compared, one at a resolution as close to the original as possible (1/12)°, which is half the original resolution of the ESA OC-CCI data, as the original resolution led to an integer overflow problem in the spTimer package. The second dataset used is with the 1° resolution, which is the downscaled version of the ESA OC-CCI dataset used in this study. The best fit is found at a lower spatial correlation decay radius in the original data although the difference in fit is only ~15 % between the data types at this radius. This occurs as the improvement in fit levels out after a certain spatial correlation radius, about 1000 km in the (1/12)° resolution data and 1500 km in the 1° resolution data.

2.2.5 Posterior Distribution

The following equation is used to specify the (logarithm of the) posterior distribution:

$$
\begin{aligned}
&\log \pi(\boldsymbol{\theta}, \boldsymbol{w}, \boldsymbol{z}^{*} | \boldsymbol{z}) \\
&\qquad \propto -\frac{NT}{2} \log \sigma_{\varepsilon}^{2} \\
&\qquad -\frac{1}{2\sigma_{\varepsilon}^{2}} \sum_{t=1}^{T} (\boldsymbol{Z}_t - \boldsymbol{x}_t \boldsymbol{\beta} - \boldsymbol{a}' \ \boldsymbol{w}_t)' (\boldsymbol{Z}_t - \boldsymbol{x}_t \boldsymbol{\beta} - \boldsymbol{a}' \ \boldsymbol{w}_t) - \frac{mT}{2} \log \sigma_{w}^{2} - \frac{T}{2} \log |\boldsymbol{S}_{\mathrm{w}}| \\
&\qquad -\frac{1}{2\sigma_{\eta}^{2}} \sum_{t=1}^{T} (\boldsymbol{w}_t - \rho \boldsymbol{w}_{t-1})' \boldsymbol{S}_{\mathrm{w}}{}^{-1} (\boldsymbol{w}_t - \rho \boldsymbol{w}_{t-1}) - \frac{m}{2} \log \ \sigma_{0}^{2} \\
&\qquad -\frac{1}{2} \log |\boldsymbol{S}_0| - \frac{1}{2} \boldsymbol{w}_0 \boldsymbol{S}_0^{-1} \boldsymbol{w}_0 + \log \pi \, (\boldsymbol{\theta}) \qquad (7)
\end{aligned}
$$

Where $\boldsymbol{\theta}$ denotes the parameters: $\boldsymbol{\beta}$, ρ, σ_{ε}^{2}, σ_{w}^{2}, σ_{0}^{2}, Φ, and ν. T is the total duration, in months, of the dataset. NT is the total number of observations (in space and time). $\boldsymbol{z}$ is the observed data and $\boldsymbol{z}^{*}$ the missing data. $\boldsymbol{S}_0$ is the initial spatial correlation matrix. The reader should refer to Bakar & Sahu (2015) for the specification of the full conditional distributions used in the Gibbs sampling.

This approach provides a full posterior distribution for each parameter fitted in the model. However, the focus is the trend parameter whose best estimate corresponds to the posterior mode and whose uncertainty is represented by a 95 % credible interval, which is defined as the 95 % highest posterior density interval (HDI) (Kruschke, 2015). Each value in the 95 % HDI has a higher likelihood than the values outside and the values within the HDI have a total probability of 95 % (Kruschke, 2015).

2.2.6 Priors

The third level of the model represents the prior distributions of the parameters used in the first two levels. These priors can be left vague representing little to no prior understanding or include detailed information from other sources. In this work, vague priors are used, except in Chapter 4 where information from biogeochemical-physical models is used. Vague priors are used for the biogeochemical parameters to reflect the lack of consensus in published chl trends, see Section 1.3, whereby observational trends cover a range of positive to negative trends on the order of a few percent per year across most regions of the globe. Even less information is known about the other parameters so vague priors are used for all parameters.

A sensitivity analysis, for a range of mean and variance values in a normal prior parameter distribution, was analysed to see their effect on the predictive model choice criterion (PMCC), in the Tasmanian Sea Province region (Region 23) (Tables 2.4 & 2.5). The results of this analysis showed relatively little effect on the PMCC except for prior distributions with extreme high mean and extreme low variance values. The prior distributions used in the following chapters for ρ and $\boldsymbol{\beta}$ are set to $N(0{,}100)$, representing a mean of zero, not biasing the trends (or other parameters) in any direction, and a variance of 100 so that distributions are relatively flat on the order of a few percent per year. Chapter 4 explores using CMIP5 model data to provide alternative values for the prior distribution of β_{Trend}, and has a more detailed analysis of the effect of prior terms in a narrower range of prior values, based on actual information. Prior distributions for the precision parameters ($1/\sigma_{\varepsilon}^{2}$ and $1/\sigma_{w}^{2}$) are specified with a gamma distribution $\Gamma(2,1)$, to provide a proper prior distribution for each component and to guarantee a proper posterior, following Bakar & Sahu (2015).

2.2.7 Convergence

The MCMC algorithm is run for 40,000 iterations to estimate the parameter values. The first 1,000 iterations are discarded as burn-in. Checks for convergence were done across all the regions, scenarios, and parameters. A demonstrative subset is included here using the trend parameter for the MSV-scenario, as this is the slowest converging parameter and the most complex scenario (17 covariates). Appendix A.1 shows trace plots for the trend parameter when spatial correlation is considered for the ESA v2.0 dataset for all regions, with the number highlighting the results from the Geweke convergence diagnostic (Geweke, 1992), these indicate that all regions show convergence under the slowest converging case. Similar diagnostic results are found for the other datasets and models.

2.3 Tables

Table 2.1 Models used, their marine biogeochemical component, associated references, and number of ensemble runs.

Model Names	Bioegeochemical Model	Reference	Number of Ensembles
CMCC-CESM	PELAGOS	Vichi et al. (2007)	1
CNRM-CM5	PISCES	Aumont & Bopp (2006), Séférian et al. (2012)	1
GFDL ESM2G	TOPAZ2	Dunne et al. (2013)	1
GFDL ESM2M	TOPAZ2	Dunne et al. (2013)	1
GISS E2 H CC	NOBM	Gregg & Casey (2007)	1
GISS E2 R CC	NOBM	Gregg & Casey (2007)	1
HadGEM2 CC	Diat-HadOCC	Palmer and Totterdell (2001)	3
HadGEM2 ES	Diat-HadOCC	Palmer and Totterdell (2001)	4
IPSL CM5A LR	PISCES	Aumont & Bopp (2006), Séférian et al. (2012)	4
IPSL CM5A MR	PISCES	Aumont & Bopp (2006), Séférian et al. (2012)	1
IPSL CM5B LR	PISCES	Aumont & Bopp (2006), Séférian et al. (2012)	1
MPI ESM LR	HAMOCC5.2	Ilyina et al. (2013)	3
MPI ESM MR	HAMOCC5.2	Ilyina et al. (2013)	1
MRI ESM1	MRI.COM3	Nakano et al. (2011)	1

Table 2.2 List of region names and their reference numbers.

Region Number	Region Name
1	Eastern Tropical Atlantic Province
2	Indian Monsoon Gyres Province
3	Indian South Subtropical Gyre Province
4	North Atlantic Tropical Gyral Province
5	North Pacific Equatorial Countercurrent Province
6	North Pacific Tropical Gyre Province
7	Pacific Equatorial Divergence Province
8	South Atlantic Gyral Province
9	West Pacific Warm Pool Province
10	Western Tropical Atlantic Province
11	Gulf Stream Province
12	Kuroshio Current Province
13	North Atlantic Drift Province
14	North Atlantic Subtropical Gyral Province (East)
15	North Atlantic Subtropical Gyral Province (West)
16	North Pacific Polar Front Province
17	North Pacific Subtropical Gyre Province (West)
18	Pacific Subarctic Gyres Province (East)
19	Pacific Subarctic Gyres Province (West)
20	South Pacific Subtropical Gyre Province
21	South Subtropical Convergence Province
22	Subantarctic Province
23	Tasman Sea Province

Table 2.3 Definition of parameters used in the equations.

Character	Definition
$\boldsymbol{a}_n'$	Kriging coefficients between the random effects at the observation and knot locations
$\boldsymbol{C}_n'$	Cross-correlation vector of the spatial random effects
$\boldsymbol{I}_n$	Identity matrix of order n
K_ν	Modified Bessel function
M	Total number of knot locations
m	Knot locations
N	Total number of observation locations
n	Observation locations
O	True chl values
$\hat{O}$	Estimated true chl values
$\boldsymbol{S}_w$	Spatial correlation matrix of the reduced set of spatiotemporal random effects
$\boldsymbol{S}_0$	Initial spatial correlation matrix
T	Total duration of time-series (months)
t	Time (months)
$\boldsymbol{w}$	Reduced set of spatiotemporal random effects at knot locations
$\boldsymbol{x}$	Design matrix
Z	Observed chl values
$\bar{Z}$	Regional mean of observed chl values
$\boldsymbol{\beta}$	Parameters (intercept and covariates)
$\boldsymbol{\gamma}$	m dimensional Gaussian process
ε	Random pure error
$\boldsymbol{\eta}$	Spatio-temporal random effects at observation locations
$\boldsymbol{\theta}$	The parameters: $\boldsymbol{\beta}$, ρ, σ_0^2, σ_ε^2, σ_w^2, Φ, ν
ν	Smoothness of the random field in spatial correlation
ρ	Unspecified autoregressive term
σ_0^2	Initial variance condition
σ_ε^2	Unknown pure error variance
σ_w^2	Site invariant spatial variance
Φ	Spatial correlation parameter

Table 2.4 Example sensitivity analysis, for a range of mean and variance values in a normal prior parameter distribution and their effect on the predictive model choice criterion (PMCC), in the Tasmanian Sea Province region (Region 23). See section 2.2 for discussion. The values used in the following chapters are a mean of 0 % yr^{-1} and a variance of 100.

	Prior Variance				
	0.1	1	10	100	1000
Prior Mean (% yr^{-1})	PMCC				
-16	4142.2	4053.28	4053.12	4052.11	4051.92
-8	4077.8	4052.47	4051.75	4054.83	4052.74
-4	4063.08	4053.26	4052.46	4051.87	4052.38
-2	4056.13	4051.42	4051.94	4050.55	4052.88
0	4052.62	4051.55	4050.9	4052.09	4052.87
2	4052.48	4052.38	4052.5	4051.98	4053.23
4	4052.4	4050.96	4050.45	4051.36	4054.63
8	4061.43	4051.34	4052.05	4053.54	4052.45
16	4113.99	4050.84	4054.37	4052.15	4053.55

Table 2.5 Example sensitivity analysis, for a range of mean and variance values in a normal prior parameter distribution and their effect on the trend estimate, from the Tasmanian Sea Province region (Region 23). This shows relatively little effect on the trend value except for prior distributions with extreme high mean and extreme low variance values. The table reports trend values in % yr^{-1}, they are calculated in units of log(mg m^{-3}) per month. The values used in the following chapters are a mean of 0 % yr^{-1} and a variance of 100 % yr^{-1}.

	Prior Variance (% yr^{-1})				
	0.1	1	10	100	1000
Prior Mean (% yr^{-1})	Trend Estimate (% yr^{-1})				
-16	0.071	-0.17	-0.19	-0.20	-0.20
-8	-0.069	-0.18	-0.19	-0.19	-0.20
-4	-0.15	-0.19	-0.19	-0.19	-0.19
-2	-0.17	-0.20	-0.19	-0.19	-0.19
0	-0.22	-0.20	-0.19	-0.20	-0.19
2	-0.25	-0.19	-0.19	-0.20	-0.19
4	-0.29	-0.20	-0.20	-0.19	-0.19
8	-0.36	-0.21	-0.20	-0.20	-0.21
16	-0.512	-0.22	-0.20	-0.19	-0.19

2.4 Figures

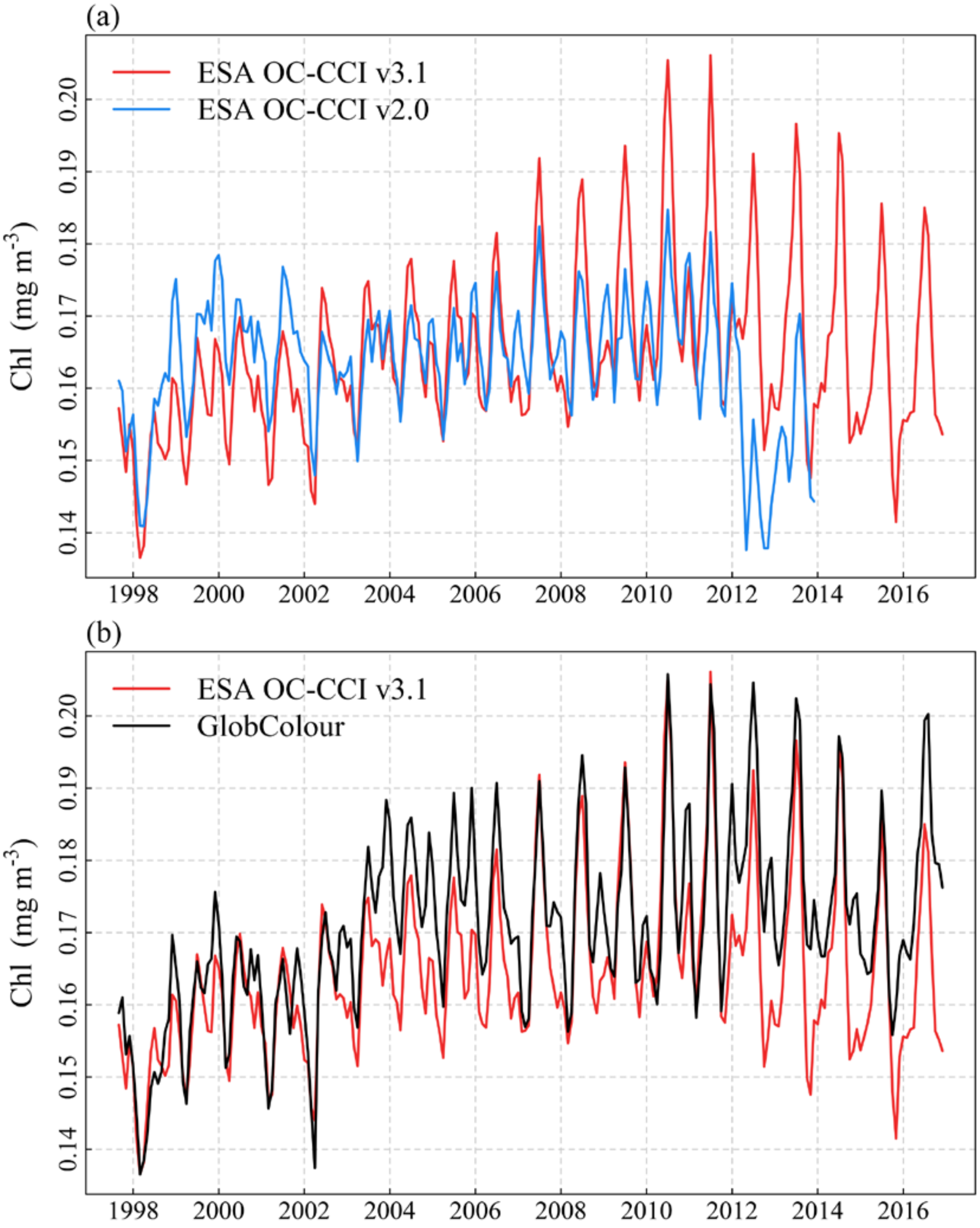

Figure 2.1 Global median chl time-series for the three chl datasets used. (a) shows the two versions of ESA OC-CCI used: v2.0 and v3.1. The v2.0 dataset shows higher chl values before the introduction of the MERIS and MODIS sensors and lower values afterwards. (b) compares ESA OC-CCI v3.1 against an alternative merged satellite-derived ocean colour dataset, GlobColour. ESA OC-CCI v3.1 typically shows lower values of chl than the GlobColour dataset, particularly in the post-2012 period, potentially associated with the introduction of the VIIRS sensor.

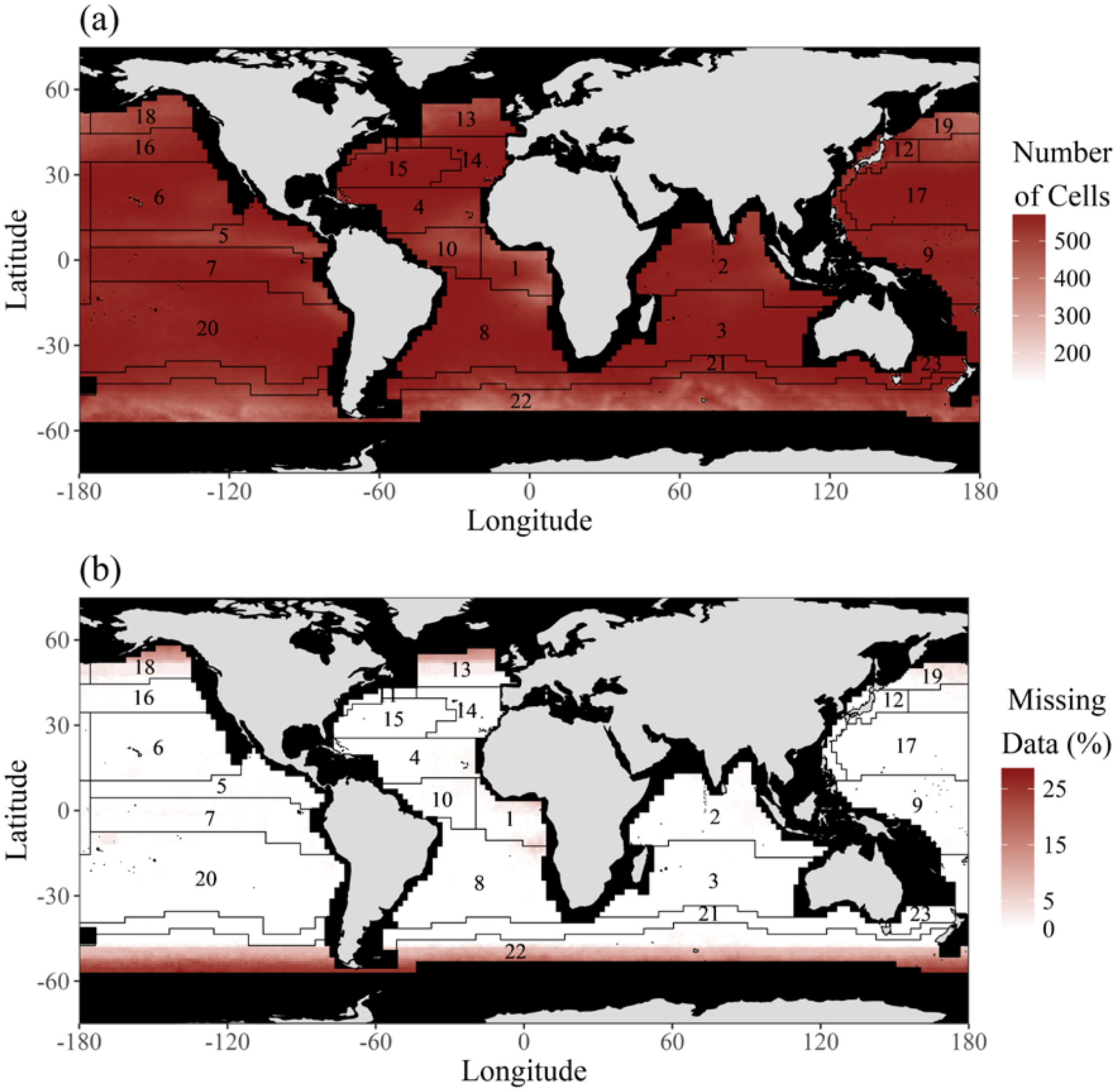

Figure 2.2 (a) The average number of grid cells used in the averaging of the ESA OC-CCI v3.1 during the downscaling process. There are a maximum of 576 (i.e. 24 x 24) grid cells, which decreases due to missing data represented in (b). Missing data are mostly found in eastern equatorial and high-latitude regions, due to the high degree of seasonal cloud cover. The names of regions are defined in Table 2.2.

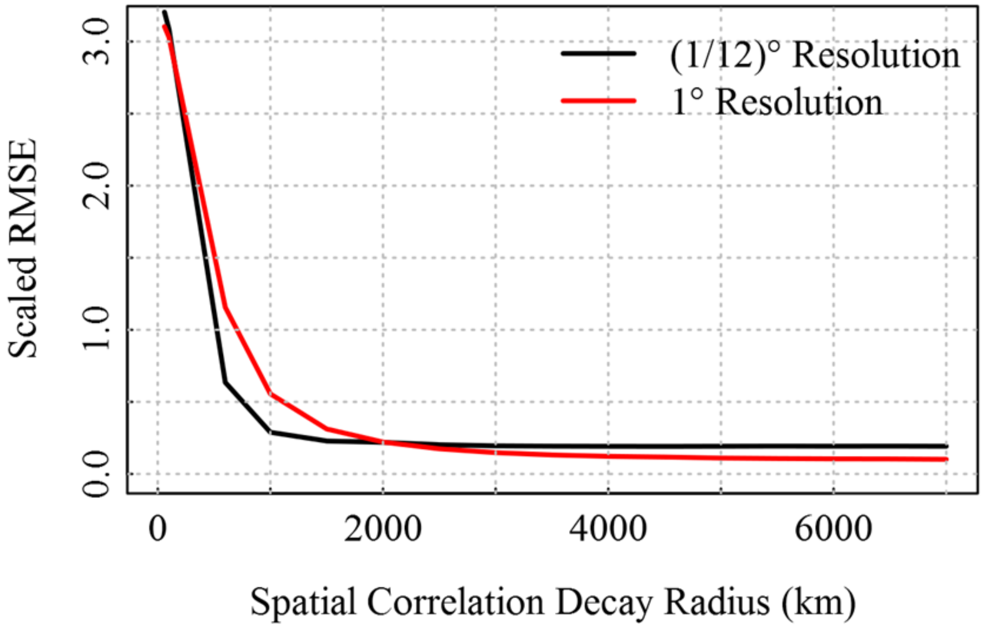

Figure 2.3 The scaled RMSE plotted against the spatial correlation decay radius for two data types in the Tasman Sea Province (Region 23) to test the importance of original data resolution on the spatial correlation decay parameter (Φ). The (1/12)° resolution used here is half the original resolution of the ESA OC-CCI data, as the original resolution led to an integer overflow problem in the spTimer package. The 1° resolution is the downscaled version of the ESA OC-CCI dataset used in this study. See section 2.2 for interpretation.

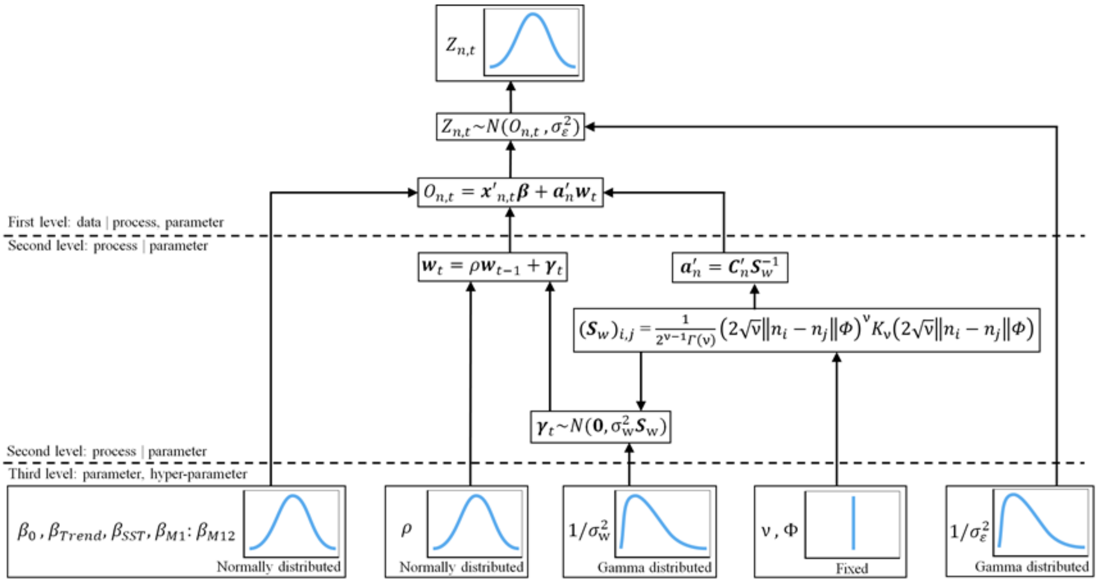

Figure 2.4 Flowchart describing the three levels of the model and linkages among the processes, parameters and hyper-parameters. At the first level, the model describes the process generating the chl data, in which the chl observations are represented by a linear regression model, white noise, and a spatio-temporal process. At the second level, the spatio-temporal process is calculated based on the parameters. At the third level, the prior distributions of the parameters are described with the use of hyper-parameters. See Section 2.2 and Table 2.3 for definition of model parameters.

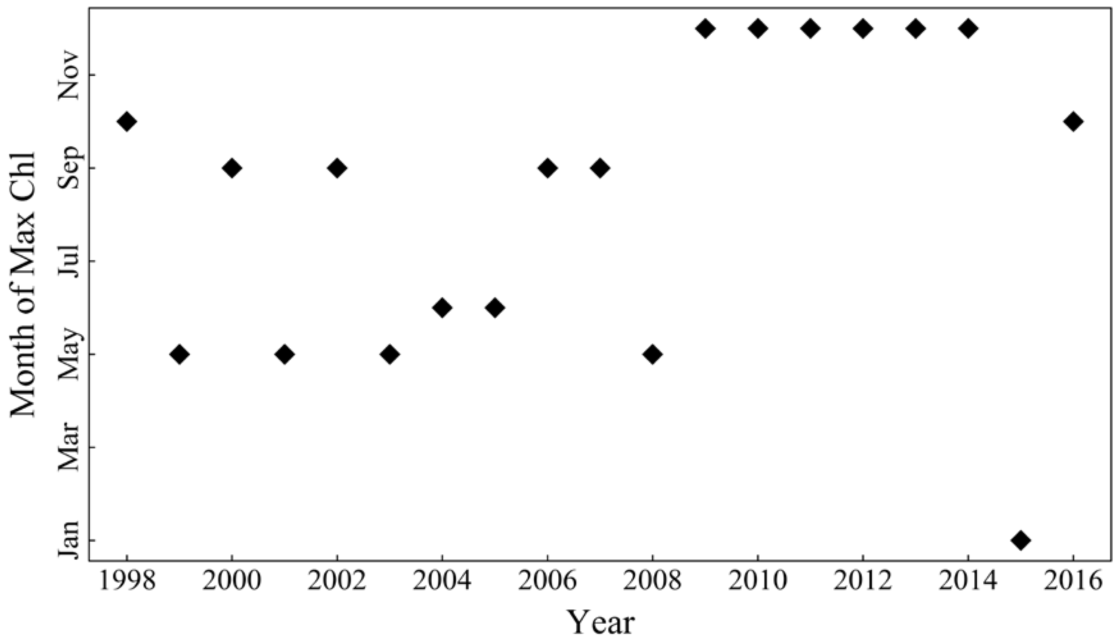

Figure 2.5 The annual month of maximum average chl in the Pacific Subarctic Gyres Province (West) (Region 18) for all complete years in the ESA OC-CCI v3.1 dataset (1998 - 2016). Prior to 2009 the month of maximum chl oscillates between summer and autumn, before shifting to December in the years 2009 - 2014.

Chapter 3: Assessing Trends and Uncertainties in Satellite-era Ocean Chlorophyll Using Space-time Modelling

This chapter has been previously published in Global Biogeochemical Cycles as:

Hammond, M. L., Beaulieu, C., Sahu, S. K., & Henson, S. A. (2017). Assessing trends and uncertainties in satellite-era ocean chlorophyll using space-time modeling. Global Biogeochemical Cycles, 31(7), 1103-1117. DOI: 10.1002/2016gb005600

MLH was responsible for the analysis and writing. CB & SKS were responsible for guidance with the statistical technique and theory. CB & SAH were responsible for guidance with the theory and interpretation of biogeochemistry.

3.1 Abstract

The presence, magnitude, and even direction of long-term trends in phytoplankton abundance over the past few decades is still debated in the literature, primarily due to differences in the data sets and methodologies used. Recent work has suggested that the satellite chlorophyll record is not yet long enough to distinguish climate change trends from natural variability, despite the high density of coverage in both space and time. Previous work has typically focused on using linear models to determine the presence of trends, where each grid cell is considered independently from its neighbours. However, trends can be more thoroughly evaluated using a spatially resolved approach. Here a Bayesian hierarchical spatio-temporal model is fitted to quantify trends in ocean chlorophyll from September 1997 to December 2013. The approach used in this study explicitly accounts for the dependence between neighbouring grid cells, which allows us to estimate trend by 'borrowing strength' from the spatial correlation. By way of comparison, a model without spatial correlation is also fitted. This results in a notable loss of accuracy in model fit. Additionally, an order of magnitude smaller global trend, and larger uncertainty, is seen when using the spatio-temporal model: -0.023 ± 0.12 % yr^{-1} as opposed to -0.38 ± 0.045 % yr^{-1} when the spatial correlation is not taken into account. The improvement in accuracy of trend estimates, and the more complete account of

their uncertainty emphasizes the solution that space-time modelling offers for studying global long-term change.

3.2 Introduction

Phytoplankton produces approximately half of the global total primary production (PP), forming the foundation of all marine ecosystems (Field et al., 1998). Quantifying how phytoplankton abundance may be affected by climate change is key to predicting the magnitude and direction of future changes in fisheries and marine ecosystems (Hoegh-Guldberg et al., 2014). The distribution of phytoplankton is primarily controlled by the degree of stratification, which in turn, affects nutrient supply and light exposure (Doney, 2006). Global warming has the potential to increase stratification, affecting phytoplankton distribution and abundance. A useful proxy for stratification is Sea Surface Temperature (SST), which is predicted to increase over both the near-term and long-term (e.g. Collins et al., 2013; Kirtman et al., 2013). Climate change is also predicted to affect wind and ocean circulation patterns, and decrease sea-ice volumes (e.g. England et al., 2014; Moore et al., 2015), with uncertain effects on phytoplankton.

To date, the most comprehensive information on phytoplankton abundance and distribution comes from the proxy chlorophyll-a concentration (chl) measured by ocean colour satellites at a high spatial and temporal resolution. Previous attempts to determine the presence of trends in ocean colour data have produced a wide range of results. For example, a global average positive trend was reported by Antoine et al. (2005), using data from both the Coastal Zone Color Scanner (CZCS) (1979 – 1986) and the first 4 years of the Sea-Viewing Wide Field-of-View Sensor (SeaWiFS) data (1998 – 2002). Using solely SeaWiFS data, Behrenfeld et al. (2006) (over the period 1997 – 2006) and Vantrepotte & Mélin (2011) (over the period 1997 – 2007) found that PP and chl show a decrease over much of the global ocean. Studies that consider temporal autocorrelation in their statistical analyses show either a low magnitude positive trend or that no global trend can yet be distinguished from noise. For example, a low magnitude global positive trend was reported by Saulquin et al. (2013) combining data from SeaWiFS (September 1997 to December 2010) and the Medium Resolution Imaging Spectrometer (MERIS) (April 2002 to April 2012) instruments. In another analysis, using solely SeaWiFS data (September 1997 to December 2008), Beaulieu et al. (2013) show that no global trend can be distinguished from noise, for which a time-series of approximately 40 years length would be required (Henson et al., 2010). This length could represent a minimum as the presence of discontinuities in the record may increase the number of years required to detect a given trend (Beaulieu et al., 2013).

In a compilation of historical, in situ, ocean transparency data Boyce et al. (2010) showed a decline of approximately 1 % yr^{-1} over the past 100 years. There have been criticisms of the methodology used, due to the lack of uniformity in collection techniques and the large rate of decrease reported (e.g. Rykaczewski & Dunne, 2011; Siegel et al., 2013). However, these criticisms were addressed in a subsequent work, which produced very similar findings (Boyce et al., 2014).

The major challenges affecting trend detection in chl include the low signal-to-noise ratio, observational gaps, and the large degree of natural variability inherent in the system (e.g. Saulquin et al., 2013). In addition, the use of simple linear temporal models in recent studies does not effectively use all the information provided by observations, ignoring the effects of spatial correlation. Including this feature in the model offers the potential to improve detection power by borrowing strength from neighbouring observations (Chandler & Scott, 2011). More generally, a spatially resolved model would better reflect the physical reality, where chl evolves in a spatially and temporally correlated fashion, and improve long-term trend estimates and their uncertainty. Therefore, this study focuses on assessing the probabilities of long-term trends in ocean chl using a) the longer time-series provided by the ESA OC-CCI (the Ocean Colour project in the Climate Change Initiative of the European Space Agency) data and b) a Bayesian hierarchical spatio-temporal approach allowing spatial correlation to be considered. By using the Bayesian spatio-temporal model an improvement in the accuracy of chl trend estimates, and a more complete account of their uncertainty, is expected.

3.3 Materials & Methods

3.3.1 Data

The chl data come from version 2.0 of the ESA OC-CCI project (Lavender et al., 2015; available at: http://www.esa-oceancolour-cci.org/). This combines data from the SeaWiFS, MERIS, and the Moderate Resolution Imaging Spectroradiometer (MODIS) sensors in order to create a continuous, bias-corrected time-series running from September 1997 to December 2013 inclusive. The resulting time-series is approximately 50 % longer than the longest individual dataset (SeaWiFS, after removal of post-2007 data due to telemetry issues). The ESA project uses band-shifting and bias-correction techniques to combine data from the individual sensors. For this study the resultant dataset is downscaled from a 1/24° grid to a 1° grid by averaging within 1° boxes. The chl values are then log-transformed after Campbell (1995). To help explain natural variability in the chl data, SST is included as a covariate. SST data are sourced from the NOAA optimum interpolation v2 data product (Reynolds et al., 2002; available at: http://www.esrl.noaa.gov/psd/data/gridded/data.noaa.oisst.v2.html). Monthly means are used in both datasets.

The data are divided into 54 regions, as defined by Longhurst (1995; 1998) according to characteristic physical forcing and biogeochemical factors. Coastal and polar waters are excluded from this analysis due to issues with data availability and quality. Coastal regions are omitted from the analysis due to higher uncertainties in ocean colour data arising from constituents in the water column, and issues removing contamination from atmospheric dust and sulphates from continental sources. Polar regions are excluded due to the high proportion of missing data, primarily due to cloud cover, which can cover 90 % of the sky during ice-free periods and has increased over recent years (Bélanger et al., 2013). Both these effects vary independently of chl and are thus challenging to compensate for (Hyde et al., 2007; Mélin et al., 2007; Schollaert et al., 2003). Coastal and polar regions are defined as in Longhurst (1998). This leaves 23 regions in which the analysis is performed, see Table 2.2.

3.3.2 Model Formulation

A hierarchical Bayesian spatio-temporal model is fitted separately to chl data in each of the 23 Longhurst regions used in this analysis. The key equations are presented below (see Table 2.3 for a list of all parameter definitions) and a representative diagram is included in Figure 2.4. In the first level, the model describes the relationship between the true and the observed chl:

$$Z_{n,t} = O_{n,t} + \varepsilon_{n,t} \qquad (1)$$

where $Z_{n,t}$ is the observed chl at location n and at month t. This is composed of the corresponding true chl value $O_{n,t}$, and a white noise process $\varepsilon_{n,t}$ which arises primarily due to random measurement error. This error is assumed independently normally distributed with a zero mean and unknown pure error variance: σ_ε^2, i.e. $\varepsilon_{1,t}, \dots, \varepsilon_{N,t} \sim \left(N(\mathbf{0}, \sigma_\varepsilon^2 \boldsymbol{I}_n)\right)$ for all t. The true chl value is represented by the following regression model:

$$O_{n,t} = \boldsymbol{x}'_{n,t}\boldsymbol{\beta} + \boldsymbol{a}'_n\boldsymbol{w}_t \tag{2}$$

composed of the covariates (including intercept) $\boldsymbol{x}_{n,t}$, the regression coefficients $\boldsymbol{\beta}$, and the term $\boldsymbol{a}'_n\boldsymbol{w}_t$ representing spatial and temporal correlation, the second level, defined in detail below. The covariates include time, month (represented as factor levels whereby each month of the year has its own additional term, i.e. a value constant for all years, is added or subtracted for each month), and SST. Time is used to estimate the temporal trend, the monthly factor to isolate the seasonal cycle, and SST is included due to its strong influence on chl variability.

In the second level, a Gaussian Predictive Process type model is used to calculate the spatio-temporal random effects. This process is used to improve computational speed for the large sets of spatio-temporal data in this study, (Banerjee et al., 2008; Finley et al., 2009; Sahu & Bakar, 2012). This model type calculates the spatio-temporal process (random effects) $\boldsymbol{\eta}_t$ at the knot sites, a subset $\boldsymbol{m}$ of the observation locations $\boldsymbol{n}$, providing the reduced set of random effects $\boldsymbol{w}_t$. The Gaussian Predictive Process reduces computational time by decreasing the size of the spatial covariance matrix, which must be inverted at each iteration of the Gibbs sampling Markov Chain Monte Carlo (MCMC) algorithm. Model-based kriging is then used to expand the reduced spatial covariance matrix to the complete set of observation locations after the inversion at each iteration. The spatio-temporal random effects between the knot and observation locations are given by $\boldsymbol{a}'_n\boldsymbol{w}_t$ where $\boldsymbol{a}'_n$ is:

$$\boldsymbol{a}'_n = \boldsymbol{C}'_n\boldsymbol{S}_w^{-1} \tag{3}$$

where $\boldsymbol{C}'_n$ is the correlation vector of the spatial random effects between the $\boldsymbol{n}$ observation locations and the $\boldsymbol{m}$ knot locations, and $\boldsymbol{S}_w$ is the correlation matrix of the reduced set of random effects ($\boldsymbol{w}_t$).

The correlation matrix $\boldsymbol{S}_\mathrm{w}$ is obtained using the Matérn correlation function (Handcock & Stein, 1993; Handcock & Wallis, 1994):

$$\kappa\left(n_i, n_j; \Phi, \nu\right) = \frac{1}{2^{\nu-1}\Gamma(\nu)}\left(2\sqrt{\nu}\|n_i - n_j\|\Phi\right)^{\nu} K_\nu\left(2\sqrt{\nu}\|n_i - n_j\|\Phi\right), \qquad \Phi > 0, \nu > 0 \tag{4}$$

where $\Gamma(\nu)$ is the standard gamma function, K_ν is the modified Bessel function (second kind) with order ν, and $\|n_i - n_j\|$ is the distance between two sites n_i and n_j. The decay parameter Φ controls how correlation decays as the distance between two sites becomes larger and is assigned a value based on testing (see Section 2.2). The parameter ν represents smoothness of the random field, and is assigned a value of 0.5, representing an exponential covariance function.

The random effects, specified at the M knot sites, are expressed as:

$$\boldsymbol{w}_t = \rho \boldsymbol{w}_{t-1} + \boldsymbol{\gamma}_t \qquad (5)$$

where $\boldsymbol{w}_{t-1}$ are the random effects at the month immediately prior to t, ρ is an unknown autoregressive term assumed to be in the interval (-1,1), and $\boldsymbol{\gamma}_t$ is the M dimensional Gaussian process: $N(\boldsymbol{0}, \boldsymbol{\Sigma}_\mathrm{w})$, where $\boldsymbol{\Sigma}_\mathrm{w} = \sigma_\mathrm{w}^2 \boldsymbol{S}_\mathrm{w}$ (σ_w^2 is the site invariant spatial variance). The auto-regressive model (Equation 5) is completed by assuming the initial condition: $\boldsymbol{w}_0 \sim N(0, \sigma_0^2\, \mathrm{S}_0)$.

The third level of the model represents the prior distributions of the parameters used in the first two levels. Vague priors are used to reflect the lack of prior knowledge about the trend value and other parameters of the model.

3.3.3 Measures Used for Analysis

The Bayesian approach provides a full posterior distribution for each parameter fitted in the model. Here the focus is on the trend parameter whose best estimate corresponds to the posterior mode and whose uncertainty is represented by a 95 % credible interval, which is defined as the 95 % highest posterior density interval (HDI) (Kruschke, 2015). As a decision rule, if the 95 % credible interval contains the value 0 % yr^{-1} it is considered unlikely that a trend is present. The number of regions exhibiting trends thus depends on this decision rule. Credible intervals are reported as ± half the credible interval width, although this represents an approximation as the posterior distributions may contain slight asymmetries.

The true chl value $O_{n,t}$ is estimated on a log scale and per month, the reasoning for this is provided in Section 3.3.1. In the results section, trend values are reported in units of % yr^{-1} to make trend values more immediately understandable to the reader. In order to convert to these units the following transformation is used:

$$\beta_{(\%/\mathrm{yr})} = 12 \times 100\left(exp\left(\beta_{(\mathrm{log/mo})}\right) - 1\right) \tag{6}$$

where $\beta_{(\%/\mathrm{yr})}$ is the trend regression coefficient in units of % yr^{-1} and $\beta_{(\mathrm{log/mo})}$ is the trend regression coefficient in units of log(mg m^{-3}) per month.

A global average of the trend and its uncertainty are calculated in the results section to provide an overall assessment of global trends. The averaging is performed for the modal trend, as well as upper and lower 95 % credible interval boundaries, as follows:

$$\bar{\beta}_{Global} = \frac{\sum_{r=1}^{R} \beta_r A_r \bar{Z}_r}{\sum_{r=1}^{R} A_r \bar{Z}_r} \tag{7}$$

where $\bar{\beta}_{Global}$ is the global weighted average trend or credible interval boundary, R is the total number of regions (23), β_r is the regional modal posterior trend or credible interval boundary, A_r is the area of each region, and $\bar{Z}_r$ is the mean chl in each region. Weighting by average chl and area is equivalent to weighting by the average surface chl content. This is used so that regions with a higher chl content contribute a higher amount to the global average, creating a global average trend which fully considers the total change in chl content.

To assess the benefit of including spatial correlation in the model, two models are fitted using different values of Φ, optimal values are chosen using a parameter sweep method to minimise RMSE, whilst maintaining computational efficiency. The first model uses the value of Φ determined as optimal by fitting ($\Phi = 2 \times 10^{-3}$), except in the Western Tropical Atlantic Province (Region 10) where a value of $\Phi = 2.1 \times 10^{-3}$ is used (see Section 2.2). The second model uses a value of $\Phi = 1000$ which effectively removes spatial correlation. The two fits are compared using the normalised root mean squared error (NRMSE) for each region:

$$NRMSE = \frac{\sqrt{\frac{\sum_{n=1}^{N}\sum_{t=1}^{T}\left(\hat{O}_{n,t} - Z_{n,t}\right)^2}{NT}}}{\bar{Z}} \tag{8}$$

Where NT represents the total number of data points in each region and $\bar{Z}$ the mean observed chl within a region. A NRMSE of zero indicates a perfect fit. Large NRMSE values indicate misfit, but do not reveal whether the model overestimates or underestimates the observations. Thus, bias is used to provide this information. Again, a bias of zero indicates a perfect fit.

$$Bias = \sum_{n=1}^{N} \sum_{t=1}^{T} \left(\hat{O}_{n,t} - Z_{n,t} \right) \tag{9}$$

The model fit is obtained using the spTimer package in R (Bakar & Sahu, 2015).

3.4 Results

3.4.1 Model Accuracy and Trend Uncertainty

The model fit, and uncertainties in the trend estimates, are compared between the model with spatial correlation and the model without spatial correlation in each individual region (Figure 3.1 and Table 3.1). The NRMSE and bias are systematically reduced in all regions when using the spatio-temporal model, showing notable improvement in accuracy. For some regions such as the North Atlantic Tropical Gyral Province (Region 4) and the South Pacific Subtropical Gyre Province (Region 20) the NRMSE and bias are improved are at least half the size in the spatio-temporal model when compared to the model without spatial correlation. In addition, the uncertainties in the trend magnitude are larger in the spatio-temporal model in 22 of the 23 regions.

Figure 3.1 shows the larger uncertainty in the spatio-temporal model for all regions except the Subantarctic Province. In the spatio-temporal model, the widest 95 % credible intervals (i.e. highest uncertainty) are found in the Kuroshio Current Province (Region 12) and the North Atlantic Subtropical Gyral Province (East) (Region 14). The narrowest 95 % credible intervals (i.e. most robust trends) are found in the Southern Ocean: the South Subtropical Convergence Province (Region 21) and the Subantarctic Province (Region 22). There does not seem to be any relationship between the size of the 95 % credible intervals and the magnitude/sign of trend.

In both cases, the global trend and uncertainty are estimated by weighting the upper and lower 95 % credible interval boundaries, and modal posterior trend, of each region by their area and average chl, relative to a global total of these values. Weighting is used to so that regions with a higher chl content contribute more to the global average trend. The global uncertainty is three times larger in the model with spatial correlation, i.e. the 95 % credible interval width is 0.12 % yr $^{-1}$ in the model with spatial correlation and 0.045 % yr $^{-1}$ in the model without spatial correlation. Note that this excludes polar and coastal regions for which the model is not run.

3.4.2 Trend Differences

The trend magnitudes for each region obtained by the spatio-temporal model and the model without spatial correlation are presented in Table 3.1 and Figures 3.1 & 3.2. In the spatio-temporal model there is no consistent sign of trend among the regions. Instead, the oceans are divided between areas of general increase and decrease. The spatio-temporal model shows no global change: -0.023 ± 0.12 % yr $^{-1}$, as opposed to a global average decline of 0.38 ± 0.045 % yr $^{-1}$ in the model without spatial correlation, where a greater number of regions show a decline. The most noticeable differences are in northern high latitude regions and the North Pacific where positive trends are detected when including spatial correlation, as opposed to negative trends when spatial correlation is not included.

In the model with spatial correlation (Figure 3.2a), the highest latitude regions all show a positive trend. It is also notable that positive trends are both more frequent and higher in magnitude in the northern hemisphere. The strongest positive trends both lie on the eastern boundaries of basins: 0.72 ± 0.20 % yr $^{-1}$ in the North Pacific Tropical Gyre Province (Region 6) and 0.97 ± 0.28 % yr $^{-1}$ in the North Atlantic Subtropical Gyral Province (East) (Region 14). The strongest negative trends can be seen in northern hemisphere western subtropical gyral provinces, with trends of -1.1 ± 0.16 % yr $^{-1}$ in the North Atlantic (Region 15) and -2.0 ± 0.10 % yr $^{-1}$ in the North Pacific (Region 17). Most provinces in the Equatorial and Southern Atlantic, specifically the North Atlantic Tropical Gyral Province (Region 4), the South Atlantic Gyral Province (Region 8), and the Western Tropical Atlantic Province (Region 10) do not exhibit a trend (95 % credible interval). The South Pacific Subtropical Gyre Province (Region 20), the South Subtropical Convergence Province (Region 21), and the Tasman Sea Province (Region 23) also do not exhibit a trend (95 % credible interval).

In the model without spatial correlation (Figure 3.2b), 21 of the 23 regions show a negative trend, the two regions with positive trends are: the North Pacific Equatorial Countercurrent Province (Region 5) (0.67 ± 0.06 % yr $^{-1}$) and the Subantarctic Province (Region 22) (0.17 ± 0.02 % yr $^{-1}$). By contrast with the model that considers spatial correlation, every region is deemed likely to have a trend. The negative trends range from -1.5 ± 0.03 % yr^{-1} in the North Pacific Subtropical Gyre Province (West) (Region 17) to -0.10 ± 0.07 % yr^{-1} in the Pacific Subarctic Gyres Province (West) (Region 19). Although there is a considerable amount of variability in the magnitude of trends between regions there does not seem to be any discernible pattern relating to latitude.

3.5 Discussion

3.5.1 Effect of Including Spatial Correlation

Phytoplankton are correlated spatially due to physical and biogeochemical controls, as is expressed in phytoplankton blooms and oligotrophic gyres. By formally including spatial correlation, the physical reality of the problem is modelled more closely and the best use of the large amount of spatial data provided by satellite observations is made, which should help compensate for the relative shortness of the length of record.

A direct comparison of the accuracy between models with and without spatial correlation is shown in Figures 3.1b & 3.1c. Including spatial correlation provides an improved fit in all regions, without exception. In addition, its inclusion leads to more positive values of the trend, in some cases changing the sign. The global average weighted trend is an order of magnitude smaller when including spatial correlation in the model, a result of the presence of both positive and negative trends in the spatial correlation model (compared to almost entirely negative trends in the model without spatial correlation).

Despite the poorer fit, the 95 % credible intervals for the model without spatial correlation are narrower in all regions except the Subantarctic Province (Region 22). A comparison of the full posterior probability distributions of trends for the two model types in all regions is presented in Appendix A.2. The Subantarctic Province (Region 22) may present an exception as in both models the uncertainty is very narrow, representing a tightly constrained trend in this region, this may result from the high proportion of missing data in winter months. The regional difference in uncertainty amounts to a global weighted uncertainty three times larger in the model with spatial correlation, i.e. the 95 % credible interval width is 0.12 % yr^{-1} in the model with spatial correlation and 0.045 % yr^{-1} in the model without spatial correlation. By ignoring spatial correlation, each site is treated as statistically independent, ignoring the fact that neighbouring sites provide similar information. As such, using a model that does not consider spatial correlation will result in an underestimation of the uncertainty due to overuse of the same information.

By comparing average time-series for individual regions and the deviations between the observations and model fit (one example in Figure 3.3, all regions can be found in Appendix A.3 & A.4) the cause of the large differences between the two approaches can be examined. First, without spatial correlation the model consistently underestimates the observations, which may be in part a result of fitting one model for the whole region, despite annual peak chl occurring at somewhat different times of year throughout the region. By producing a model for the whole region without considering spatial correlation the peaks are essentially smoothed out. However, in some of the largest regions, such as in the South Pacific Subtropical Gyre Province (Region 20), the underestimation occurs equally throughout the year. In these regions, it may be especially important to include additional environmental indicators to explain interannual variability in chl observations when ignoring spatial correlation. The regional variance in these additional environmental factors may make up for the lack of spatial information in the simpler model. Second, and most importantly, without spatial correlation the model seems unable to capture interannual variability, particularly in months of peak chl, a very important factor in chl variability. In both models, there is a tendency to underestimate the observations. This is due to the logarithmic transform, which reduces the more extreme high values. The closer fits produced by the spatio-temporal model suggest that it results in more robust trend estimates.

3.5.2 Effect of Including the Monthly Factor and SST Covariates

To isolate the linear temporal trend from natural variability and the seasonal cycle two additional covariates are included: SST and a monthly factor. However, SST also exhibits a long-term trend, which is a proxy for the primary proposed driver of changes in chl (i.e. stratification). The seasonality of phytoplankton is also projected to show a long-term trend (Henson et al., 2013), which is likely caused by the long-term trend in SST. Thus, the estimated trends may represent the remaining trends in chl that are not directly related to changing SST. By comparing the model without spatial correlation to other studies, the trend magnitudes and directions detected in most regions of this study are found to be similar (see Section 3.5.6).

Additionally, the relationship between the SST and trend covariates was assessed in the two model types. These two models lead to different trend estimates, which could result from changes to how the two models capture the time, the monthly factor, and SST effects, rather than a change in ability to detect trends accurately. To diagnose this problem, the change in the time covariate between the two models is plotted against the change in the SST covariate (Figure 3.4). If the changes in trends between models are occurring due to a change in SST effect, the two values would be expected to show a strong correlation. This does not appear to be the case, instead there appears to be no association between the two. This suggests that the SST covariate does not contain a significant portion of the chl trend and that the estimated trend terms can be considered the total trend over the period.

The SST covariate is included to consider some of the effects of natural variability, which improves fit and allows us to obtain better trend estimates. However, the chl trend detected here is ultimately a response to external forcings and natural variability, which may include SST. This study focuses on trend detection, which aims to verify whether chl has changed in a statistical sense. Formally separating the effects of anthropogenic and natural external forcings would require an attribution study (e.g. Hegerl et al., 2010), which is outside the scope of this work.

Whilst SST is a strong driver of phytoplankton seasonality, in many regions the statistical model suffered issues with MCMC convergence if an extra seasonality term was not included, likely due to other physical driving factors that were not included in the model. The inclusion of the monthly factor may mean the SST term considers the chl response on timescales longer than seasonal, while the monthly factor primarily encapsulates the seasonal variability. The effect of the monthly factor on model fit is assessed in Table 3.2. In the majority of regions, the monthly factor leads to better model fit and thus to more robust trend estimates. There are, however, three regions where the inclusion of the monthly factor has no effect on model fit and three further regions where there is a slight detrimental effect on model fit. For consistency in trend estimates it is argued that including the monthly factor in all regions is the best procedure. The improvement in model fit, and thus in trend estimate robustness, in the majority of regions is emphasised.

The monthly factor is included in the model as a further term to help isolate the seasonal cycle and ease the estimation of trends. Seasonality was represented this way due to the use of monthly averages in the data, therefore seasonality can be no smoother than this representation, although the monthly factor is a slow computational approach as it requires fitting 11 additional covariates to represent the seasonality. An alternative approach such as harmonic regression (Lee et al., 2013) may be more appropriate, particularly if the data was of finer temporal spacing, as it will allow faster computation.

3.5.3 Model Fit

The regions with the worst fit to observations (highest NRMSE values) are, in the model with spatial correlation, the North Atlantic Tropical Gyral Province (Region 4) and the Kuroshio Current Province (Region 12). The Kuroshio Current Province (Region 12) includes coastal waters that are typically excluded from this study. Therefore, the trend estimate is likely to suffer from observational issues in coastal regions, leading to an increased uncertainty in this region. The North Atlantic Tropical Gyre Province (Region 4) could be influenced by Saharan dust either stimulating chl growth or introducing errors into the satellite data (Kaufman et al., 2005). However, this does not seem to affect the Western Tropical Atlantic Province (Region 10) in the same way.

A possible approach to improving the model lies in altering the representation of seasonality. The spatio-temporal model currently uses a fixed seasonality, where there is assumed to be no shift in the phase of the annual cycle of phytoplankton abundance during the 16 year time-series, which is at odds with previous studies which observe interannual variability (e.g. Henson et al., 2009; Racault et al., 2012) and project trends (Henson et al., 2013) in bloom phenology. Research has shown that permitting interannual change in seasonality within a model allows for more of the variability to be explained (Vantrepotte & Mélin, 2011). Allowing for interannual change in seasonality is currently incompatible with the model but it could potentially achieve a closer model fit throughout the time-series, particularly in those months and regions where blooms are expected.

Another approach to improving model fit is to consider an anisotropic spatial correlation, which depends on the direction, in addition to the distance, between two sites. In the majority of regions in this study spatial correlation shows a different pattern in the N-S and E-W directions, indicating anisotropic spatial correlation (see Figure 3.5). Allowing anisotropic spatial correlation could potentially further improve the model accuracy by better representing the effects of ocean currents. However, there is a large improvement in model fit resulting from the inclusion of isotropic spatial correlation, and any improvements beyond this are expected to be minimal.

3.5.4 Region Selection

The data are divided into Longhurst provinces, which are defined by their characteristic biogeochemical and physical forcing and thus each province should exhibit an approximately uniform trend within its borders. As a different region definition might affect the results, the region boundaries as defined in Henson et al. (2010) are explored as an alternative (see Table 3.3 and Figure 3.6). The Henson et al. (2010) biomes divide the ocean according to seasonal light limitation, oligotrophy, and annual net heat flux, similar criteria to some of the Longhurst provinces. However, they are on average larger with 14 global open ocean regions instead of 23. The most significant difference, in the results from this approach, is in the Pacific Ocean where a decreasing trend is found at high latitudes. This result is the opposite of the pattern seen in the Atlantic where there is an increasing trend at high latitudes. The difference likely occurs due to the larger boundaries incorporating sub-regions where the trend is different. This suggests that boundary selection is important, especially as one trend value represents a large portion of the ocean. As a result, Longhurst provinces are used to avoid larger regions obscuring smaller scale patterns of change. Longhurst regions also allow a faster computation time due to their typically smaller size. Any division will introduce a degree of “edge effect”, as grid cells located at the edges of the region do not consider the full range of points within their spatial correlation range. However, including information from grid cells outside a Longhurst region may result in poor estimates as the trends and behaviors there are expected to be different.

As physical and biogeochemical conditions change into the future, the location of boundaries separating different provinces is also expected to change. Recent work has considered region boundaries that are dynamic in time (e.g. Reygondeau et al., 2013). The use of predefined regions in the present study ignores the effect of potential change in region boundaries, which could affect the trend estimates. Thus, temporal changes in a dynamic region boundary would lead to a portion of the static region belonging to a different biogeochemical region with a different trend. For example, it has been noted that oligotrophic gyre regions may be expanding, reportedly in the range of 0.8 - 4.3 % yr^{-1} (Polovina et al., 2008), though a proportion of this is likely interannual variability. Thus, a relatively small change in region boundaries over the period of the ESA OC-CCI dataset may be present, although the direction of this change could be quite heavily dependent on the chosen threshold. Polovina et al. (2008) defined these regions as < 0.07 mg m^{-3}, whereas Irwin & Oliver (2009) used similar data but with a threshold defined on SST and chl < 0.08 mg m^{-3} and found regions to be stable. A modest improvement in model fit accuracy is expected from implementing dynamic boundaries, but this should be the focus of future work as care should be taken over the boundary definitions and thresholds.

3.5.5 Choice of Priors

One of the strengths of Bayesian analysis is the use of “priors” that represent, in the model framework, previous understanding of the particular topic. For this study, priors could have been formulated using independent information from previous studies on the relationship of chl with SST or the magnitudes, and directions, of chl trends. Instead, vague priors are used, i.e. the prior distributions have large variance reflecting a lack of knowledge about chl trends and other parameters estimated in the model. As the focus of this work is to assess the effect of including spatial correlation when estimating chl trends, providing prior information may inhibit a complete comparison. In future work prior information could be used for a more complete understanding of global trends.

3.5.6 Comparison with Previous Studies

For a number of regions, the trends estimated using the spatio-temporal model are of a similar magnitude to other studies, particularly to ocean colour studies carried out on a more regional scale (e.g. Saulquin et al., 2013; Siegel et al., 2013; Vantrepotte & Mélin, 2011). However, there are a few regions where trends of the opposite magnitude are estimated, particularly in the North Pacific and North Atlantic. These differences can be attributed to both the different approach and a longer time span used compared to previous studies. There are a limited number of studies considering a time span as long as considered here; these include Gregg & Rousseaux (2014) and Signorini et al. (2015), although neither uses the Longhurst region divisions. Both studies agree more closely with the trends estimated using the model without spatial correlation rather than the model with spatial correlation. This is because both Gregg & Rousseaux (2014) and Signorini et al. (2015) use regional average time-series, an approach more consistent with the model without spatial correlation presented here. When comparing the results of these two studies to the trends obtained from the model with spatial correlation, there is agreement in the Equatorial Atlantic, the South Atlantic, the South Pacific, much of the Indian Ocean, and the Southern Ocean. The most significant differences are in the subpolar North Atlantic and North Pacific, where the present study shows positive trends.

More specifically, the North Pacific shows the biggest difference from Gregg & Rousseaux (2014) and Signorini et al. (2015) where positive trends are found over the eastern and northern extents. This is most likely a result of the strong influence of the El Niño Southern Oscillation (ENSO) on chl in the region and the improved fit to interannual variability provided by the inclusion of spatial correlation in the model. It should be noted that the North Pacific Equatorial Countercurrent Province (Region 5) trend is strongly positive in both the model estimates, contrary to the trends estimated by Gregg & Rousseaux (2014). The difference is likely due to the different timescales and the different approaches used to account for seasonal variability, as Gregg & Rousseaux (2014) model trends in annual medians of monthly means. In addition, including SST within the model helps to explain the interannual variability, as ENSO is associated with large SST variation in the Pacific.

High latitude regions also consistently show positive trends in the present study, which have not been observed in other satellite studies (e.g. Gregg & Rousseaux, 2014; Vantrepotte & Mélin, 2011). However, this result is consistent with other longer-term observational studies such as Martinez et al. (2016), which showed an increase in phytoplankton abundance since the 1960s in North Atlantic Continuous Plankton Recorder data. The similarity to results from a longer-term study could indicate that the method in the present study has an improved ability to isolate a secular trend from seasonal and interannual variability. This result also follows the theoretical framework where phytoplankton abundance is affected by increasing SST, leading to decreased phytoplankton abundance in nutrient limited regions and increased phytoplankton abundance in light limited areas (Doney, 2006). However, contrary to expectations for nutrient limited regions, the SST covariate values determined by the model are positive, indicating chl is increasing with SST, in all regions (see Figure 3.7). This may suggest that in the monthly factor accounts for the majority of the variability, particularly seasonal, expected to be associated with SST.

Model projections show an overall global decrease in chl, associated with a global SST increase and associated increases in grazing except in major sea-ice forming regions, the subpolar North Pacific, and the South Pacific (Bopp et al., 2013; Cabré et al., 2015; Laufkötter et al., 2015). Hindcast models (covering 1960 - 2006) show similar results but with a more mixed pattern in the Southern Ocean, and increases in the subpolar North Atlantic (Laufkötter et al., 2013).

The regional patterns of decline detected in the present study do not correspond to the pattern of trends detected in a longer-term compilation of multiple observational sources by Boyce et al. (2014). This disparity would suggest that, despite the increased robustness of the trends detected using a spatio-temporal model, in a number of regions the shortness of the record still challenges the detection of a long-term trend. Alternatively, this disparity may arise from using a multi-sensor dataset, i.e. one that contains data from multiple ocean colour sensors. Due to only a partial temporal overlap and bias between individual sensors there is the potential for multi-sensor datasets to introduce discontinuities in the record. Such discontinuities have been shown to potentially impact trends estimated in multi-sensor datasets, due to uncorrected biases, potentially leading to misleading conclusions (Mélin, 2016). The ESA OC-CCI dataset used here has undergone an extensive bias correction process, so will be affected by this issue to a more limited degree. Assessing the effect of taking into account discontinuities in multi-sensor records, in this model framework, is the focus of Chapter 5.

3.6 Conclusions

This study presents, to the author’s knowledge, the first Bayesian spatio-temporal analysis of trends in ocean chlorophyll. The Bayesian spatio-temporal analysis 1) provides a more accurate fit to observations, 2) provides a more complete assessment of uncertainty, and 3) impacts trend estimates when compared to a model that is not spatially resolved. For example, the global trend in chl from the spatio-temporal model (-0.023 ± 0.12 % yr^{-1}) is an order of magnitude smaller than the trend detected using a model without spatial correlation (-0.38 ± 0.045 % yr^{-1}), and has an approximately three times larger uncertainty. This result suggests trend analysis using statistical models that are not spatially resolved might lead to biased and overconfident trend estimates. The significant differences between the two approaches (i.e. with and without spatial correlation) suggests it is important to fully consider space-time effects when assessing the impacts of climate change, particularly for data sets with large uncertainty or with a short record length. Another innovative aspect of this study is the use of a Bayesian approach that provides the advantage of quantifying the full probability distribution of trends in each region.

While the detected global decline in chl over the period September 1997 to December 2013 is small, there is regional disparity with both positive and negative trends present across the globe ranging from approximately -2 % yr^{-1} to 1 % yr^{-1}. If sustained, these changes could result in a cascade effect throughout the entire trophic system via trophic amplification by changing the available food supply. Changes in phytoplankton abundance also impact the carbon cycle with potential feedbacks throughout the biogeochemical system. Increasing chl concentration is detected in high latitude regions, which are dominated by large phytoplankton species. This result could suggest an increasing carbon export to the deep ocean in these regions, a potential climate feedback, although changes in specific species are not assessed.

By including environmental covariates to explain seasonal and interannual variability the secular trend within the available data can be more clearly distinguished. However, with only 16 years of data it may still not be possible to distinguish a long-term response to climate change from natural variability in all regions, especially where the signal-to-noise ratio is small. Future work should aim to include additional datasets (e.g. in situ data) for additional information and to increase the period covered in the analysis. Combining evidence from different and independent data sets offers the potential to increase confidence in the trends detected and to determine whether they can be distinguished from interannual variability, which can be achieved within the space-time modelling framework. Space-time modelling offers a solution for quantifying global change in general.

3.7 Tables

Table 3.1 Summary of trends estimates for all regions, their 95 % credible interval (CI) representing the uncertainty; and model goodness-of-fit, measured by the normalised root mean squared error (NRMSE) and bias. Results are shown for the model with spatial correlation terms (STC) and without (TC). Entries in bold represent regions where the 95 % credible interval does not include 0 % yr^{-1}, i.e. a trend is most likely present. All regions in the model without spatial correlation are likely exhibiting a trend. The region names are defined in Table 2.2.

Region	Model Type	Trend Value (% yr^{-1})	Lower CI Boundary (% yr^{-1})	Upper CI Boundary (% yr^{-1})	NRMSE	Bias (% yr^{-1})
1	**STC**	**-0.79**	**-0.97**	**-0.58**	**0.24**	**-0.017**
	TC	**-0.70**	**-0.78**	**-0.63**	**0.42**	**-0.043**
2	**STC**	**-0.29**	**-0.43**	**-0.16**	**0.14**	**-0.0034**
	TC	**-0.95**	**-0.99**	**-0.92**	**0.33**	**-0.014**
3	**STC**	**-0.58**	**-0.68**	**-0.46**	**0.12**	**-0.0013**
	TC	**-0.87**	**-0.91**	**-0.84**	**0.38**	**-0.01**
4	STC	-0.029	-0.19	0.093	0.32	-0.021
	TC	**-1.21**	**-1.29**	**-1.13**	**0.63**	**-0.051**
5	**STC**	**0.54**	**0.36**	**0.70**	**0.23**	**-0.011**
	TC	**0.67**	**0.60**	**0.72**	**0.38**	**-0.026**
6	**STC**	**0.72**	**0.55**	**0.95**	**0.11**	**-0.00093**
	TC	**-0.84**	**-0.88**	**-0.81**	**0.30**	**-0.0059**
7	**STC**	**-0.11**	**-0.16**	**-0.06**	**0.10**	**-0.0025**
	TC	**-0.35**	**-0.38**	**-0.33**	**0.20**	**-0.0075**
8	STC	0.034	-0.068	0.13	0.16	-0.003
	TC	**-0.50**	**-0.54**	**-0.46**	**0.40**	**-0.017**
9	**STC**	**-0.57**	**-0.73**	**-0.37**	**0.15**	**-0.0018**
	TC	**-0.51**	**-0.57**	**-0.46**	**0.44**	**-0.012**
10	STC	-0.21	-0.42	0.05	0.24	-0.011
	TC	**-0.58**	**-0.65**	**-0.53**	**0.33**	**-0.02**
11	**STC**	**0.16**	**0.01**	**0.29**	**0.21**	**-0.01**
	TC	**-0.24**	**-0.33**	**-0.16**	**0.27**	**-0.016**
12	**STC**	**-0.93**	**-1.41**	**-0.62**	**0.30**	**-0.033**
	TC	**-0.44**	**-0.55**	**-0.35**	**0.45**	**-0.045**
13	**STC**	**0.64**	**0.47**	**0.87**	**0.18**	**-0.013**

Region	Model Type	Trend Value (% yr $^{-1}$)	Lower CI Boundary (% yr $^{-1}$)	Upper CI Boundary (% yr $^{-1}$)	NRMSE	Bias (% yr $^{-1}$)
	TC	**-0.59**	**-0.64**	**-0.54**	**0.33**	**-0.041**
14	**STC**	**0.97**	**0.68**	**1.24**	**0.18**	**-0.008**
	TC	**-0.94**	**-1.00**	**-0.89**	**0.34**	**-0.019**
15	**STC**	**-1.05**	**-1.22**	**-0.90**	**0.13**	**-0.0017**
	TC	**-0.55**	**-0.59**	**-0.51**	**0.25**	**-0.0062**
16	**STC**	**0.36**	**0.27**	**0.44**	**0.20**	**-0.0093**
	TC	**-0.81**	**-0.89**	**-0.73**	**0.31**	**-0.00019**
17	**STC**	**-2.02**	**-2.13**	**-1.92**	**0.12**	**-0.00087**
	TC	**-1.45**	**-1.48**	**-1.43**	**0.24**	**-0.0038**
18	**STC**	**0.34**	**0.14**	**0.52**	**0.20**	**-0.019**
	TC	**-0.31**	**-0.36**	**-0.25**	**0.28**	**-0.035**
19	**STC**	**0.31**	**0.15**	**0.47**	**0.23**	**-0.032**
	TC	**-0.10**	**-0.17**	**-0.03**	**0.34**	**-0.061**
20	STC	-0.13	-0.24	0.00	0.12	-0.0014
	TC	**-0.29**	**-0.33**	**-0.25**	**0.53**	**-0.016**
21	STC	0.015	-0.052	0.086	0.18	-0.0066
	TC	**-0.12**	**-0.17**	**-0.09**	**0.45**	**-0.035**
22	**STC**	**0.18**	**0.17**	**0.19**	**0.24**	**-0.013**
	TC	**0.17**	**0.15**	**0.19**	**0.34**	**-0.022**
23	STC	-0.10	-0.26	0.032	0.19	-0.0097
	TC	**-0.55**	**-0.63**	**-0.48**	**0.27**	**-0.016**

Table 3.2 Effect of the monthly factor on the normalised root mean square error (NRMSE). In most regions, a modest increase in model fit is seen, although in three regions the effect is negligible and in three other regions this leads to a slightly worse model fit.

	Monthly Factor Not Present	Monthly Factor Present
Region	NRMSE	
1	0.2396	0.2402
2	0.1369	0.1366
3	0.1218	0.1218
4	0.3187	0.3185
5	0.2253	0.2251
6	0.1084	0.1076
7	0.1051	0.1045
8	0.1600	0.1571
9	0.1488	0.1488
10	0.2534	0.2428
11	0.2219	0.2133
12	0.2986	0.2984
13	0.1816	0.1751
14	0.1880	0.1822
15	0.1265	0.1265
16	0.2075	0.1999
17	0.1178	0.1171
18	0.2011	0.1991
19	0.2383	0.2346
20	0.1197	0.1202
21	0.1839	0.1844
22	0.2578	0.2441
23	0.1945	0.1875

Table 3.3 Trend estimates and their 95 % credible interval (CI) obtained with the spatio-temporal model using the boundaries as defined in Henson et al. (2010). Entries in bold represent regions where the 95 % credible interval does not include zero, i.e. the presence of a trend is likely.

Region	Region Name	Trend Value (% yr $^{-1}$)	Lower CI Boundary (% yr $^{-1}$)	Upper CI Boundary (% yr $^{-1}$)
1	**High latitude North Pacific**	**-2.3**	**-2.4**	**-2.1**
2	**Oligotrophic North Pacific**	**0.43**	**0.34**	**0.52**
3	Equatorial Pacific	-0.070	-0.19	0.070
4	**Oligotrophic South Pacific**	**0.54**	**0.38**	**0.74**
5	**Southern Ocean Pacific**	**-0.99**	**-1.1**	**-0.84**
6	**High latitude North Atlantic**	**0.72**	**0.50**	**0.93**
7	**Oligotrophic North Atlantic**	**-1.1**	**-1.3**	**-0.84**
8	**Equatorial Atlantic**	**-1.1**	**-1.4**	**-0.79**
9	**Oligotrophic South Atlantic**	**-0.47**	**-0.66**	**-0.28**
10	**Southern Ocean Atlantic**	**0.42**	**0.10**	**0.74**
11	**Arabian Sea**	**-1.4**	**-1.7**	**-1.0**
12	**Bay of Bengal**	**-0.90**	**-1.2**	**-0.62**
13	**Oligotrophic Indian**	**-0.61**	**-0.73**	**-0.47**
14	**Southern Ocean Indian**	**-0.86**	**-1.1**	**-0.65**

3.8 Figures

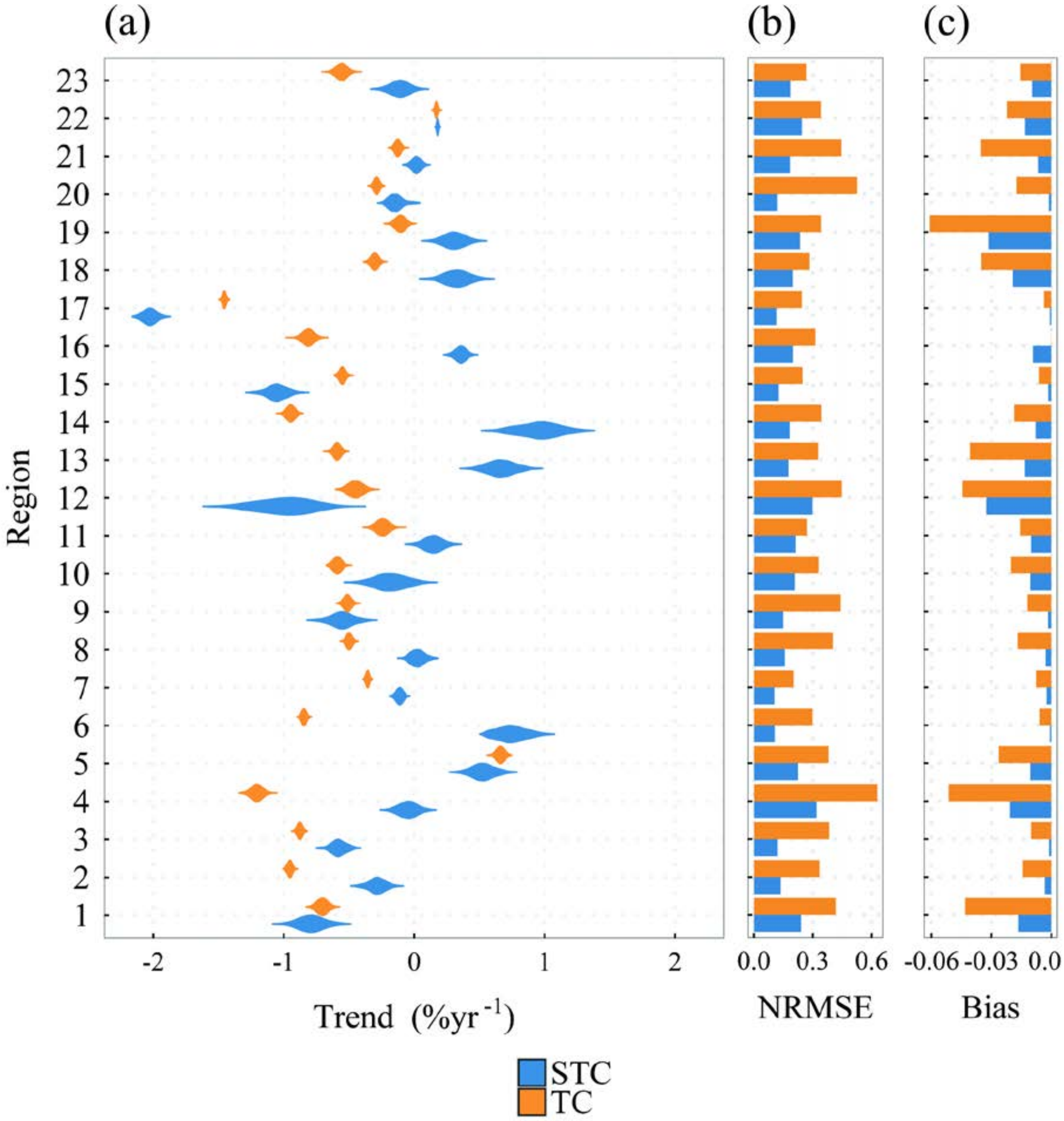

Figure 3.1 (a) Posterior probability densities for the chl trends obtained in each region, (b) accuracy of the fit via the normalised root mean squared error (NRMSE) for each region, and (c) the general direction of any misfit (bias). Two models are used in each region: STC refers to the model with spatio-temporal correlation and TC refers to the model with temporal correlation only (i.e. without spatial correlation). The regions are defined in Table 2.2.

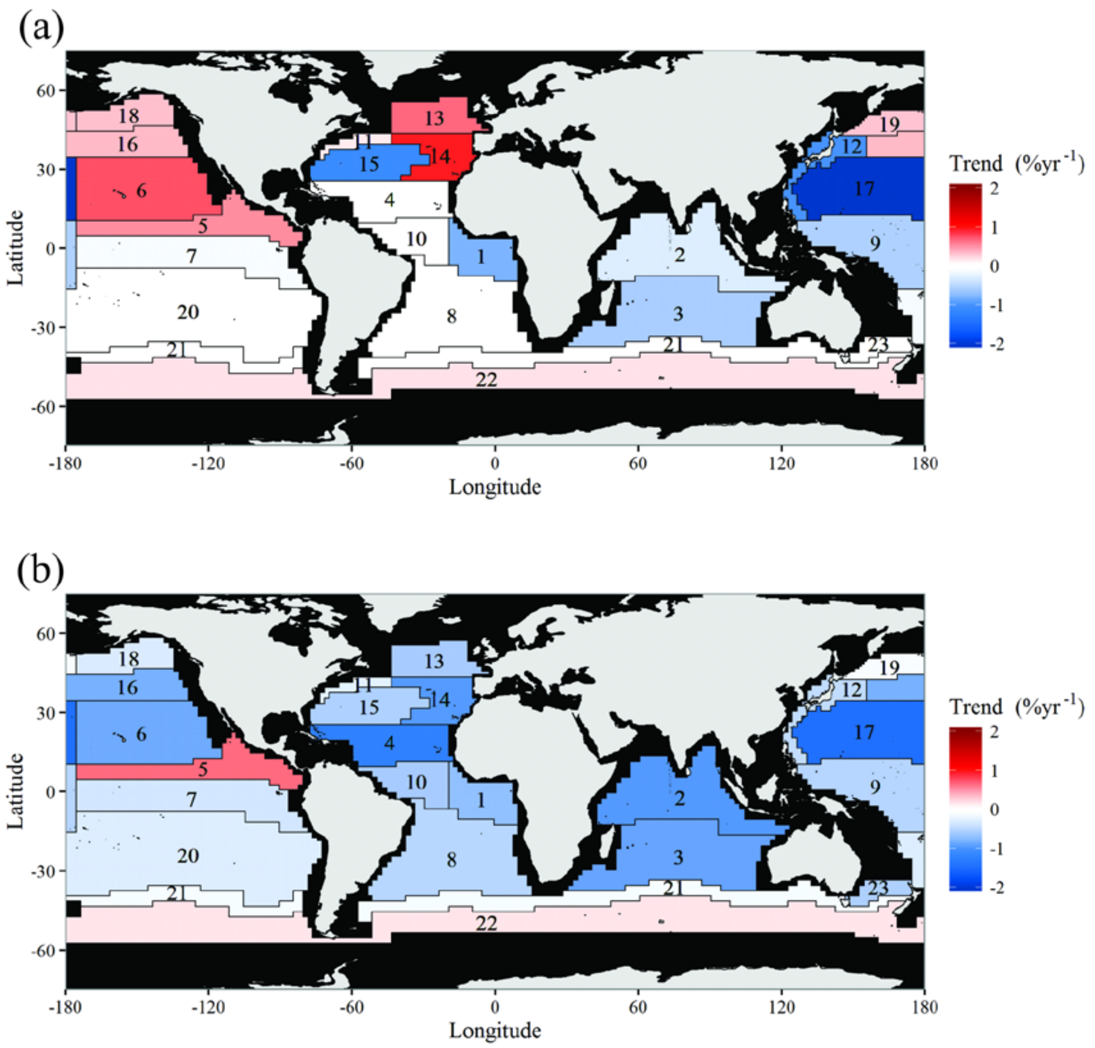

Figure 3.2 Magnitude of the chl trend detected in each region (Sep 1997- Dec 2013) for (a) the spatio-temporal model and (b) using the model without spatial correlation. Black regions are not considered in the analysis due to limited data availability. Regions that are white indicate that the absence of a trend is most likely, based on a 95 % credible interval. The region names are defined in Table 2.2.

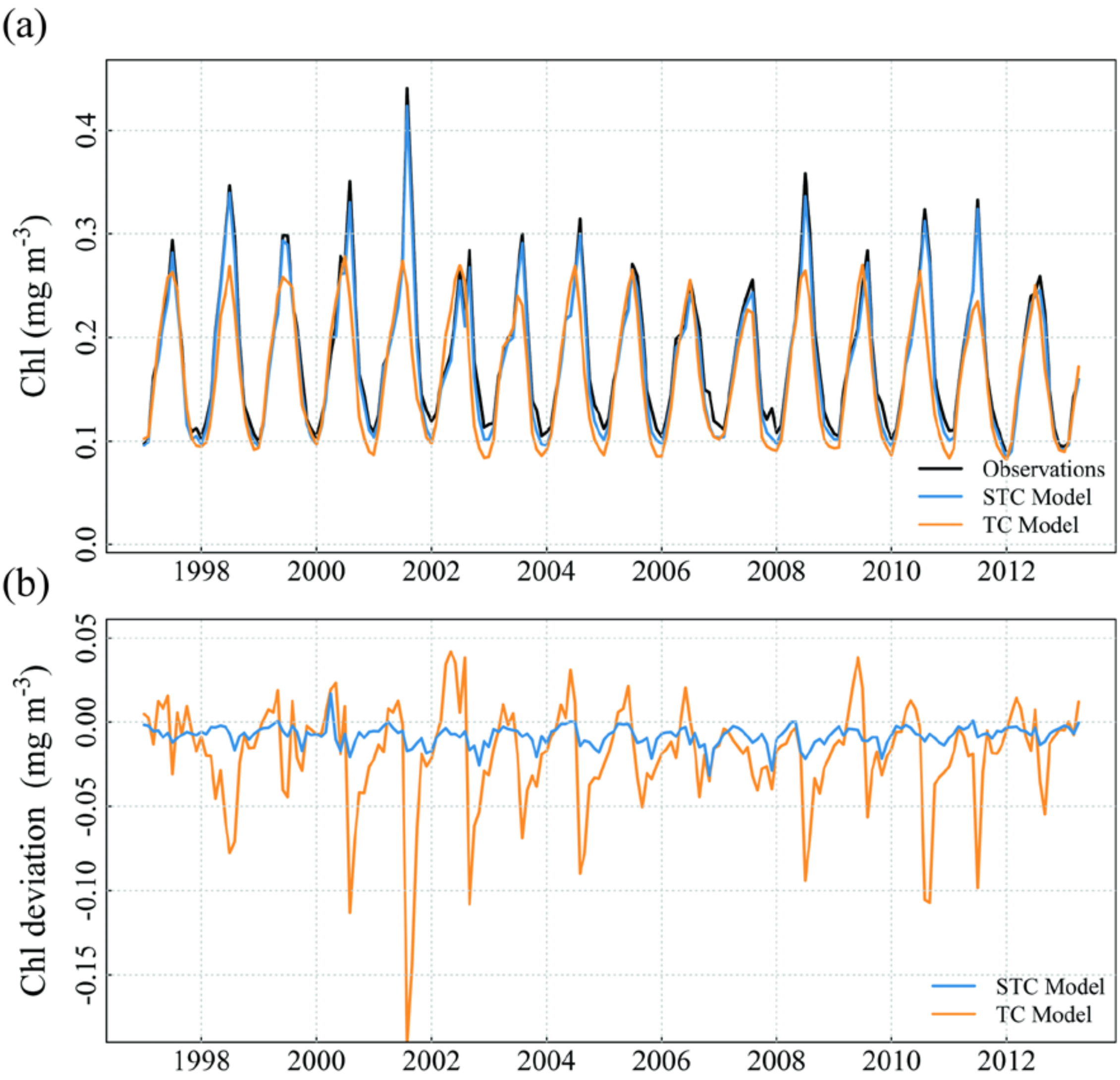

Figure 3.3 Comparison of observed and modelled chl for the North Atlantic Subtropical Gyral Province (East) (Region 14). (a) Regionally-averaged observed and modelled chl time-series, and (b) model deviations from observations. Two models are used: STC refers to the model with spatio-temporal correlation and TC refers to the model with temporal correlation only (i.e. without spatial correlation). Note that by considering spatial correlation, the model better captures the full extent of both interannual and seasonal variability.

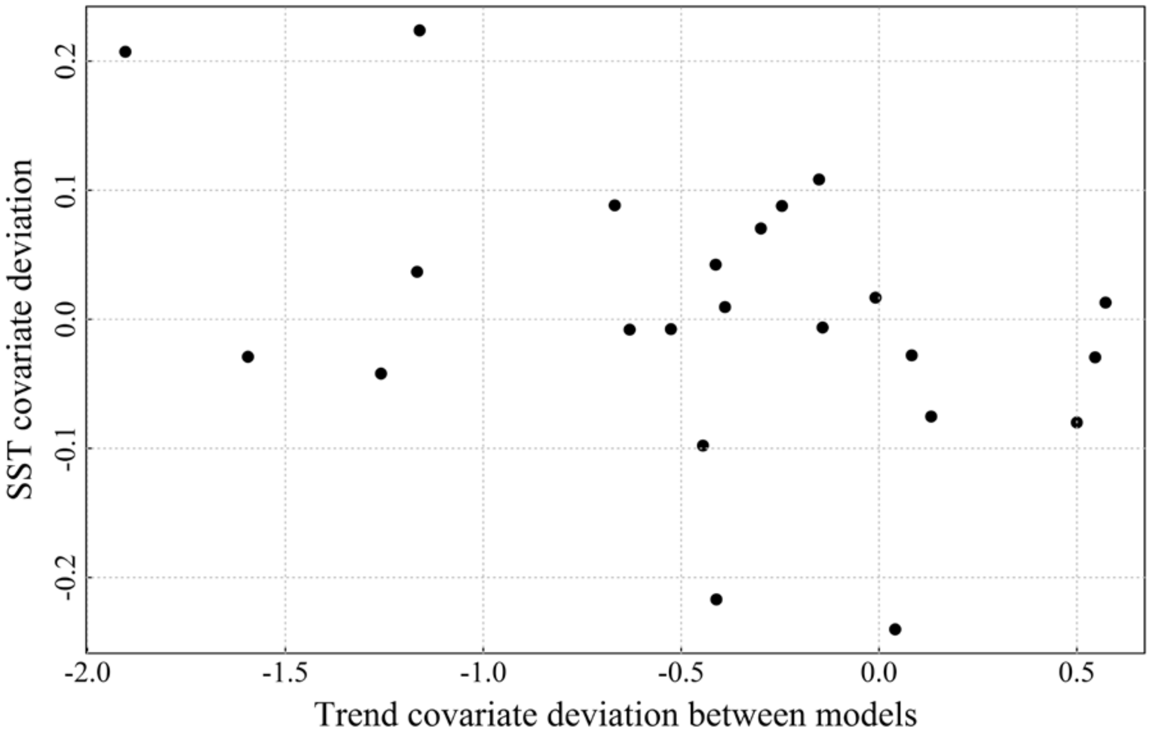

Figure 3.4 Deviations in trend and SST covariates between the two models. The x-axis shows the trend covariate for the spatial correlation model subtracted from the trend covariate for the model without spatial correlation. The y-axis shows the same but for the SST covariate. No correlation is seen between the two, indicating that the change in trend value between the two models is not due to a change in the SST covariates.

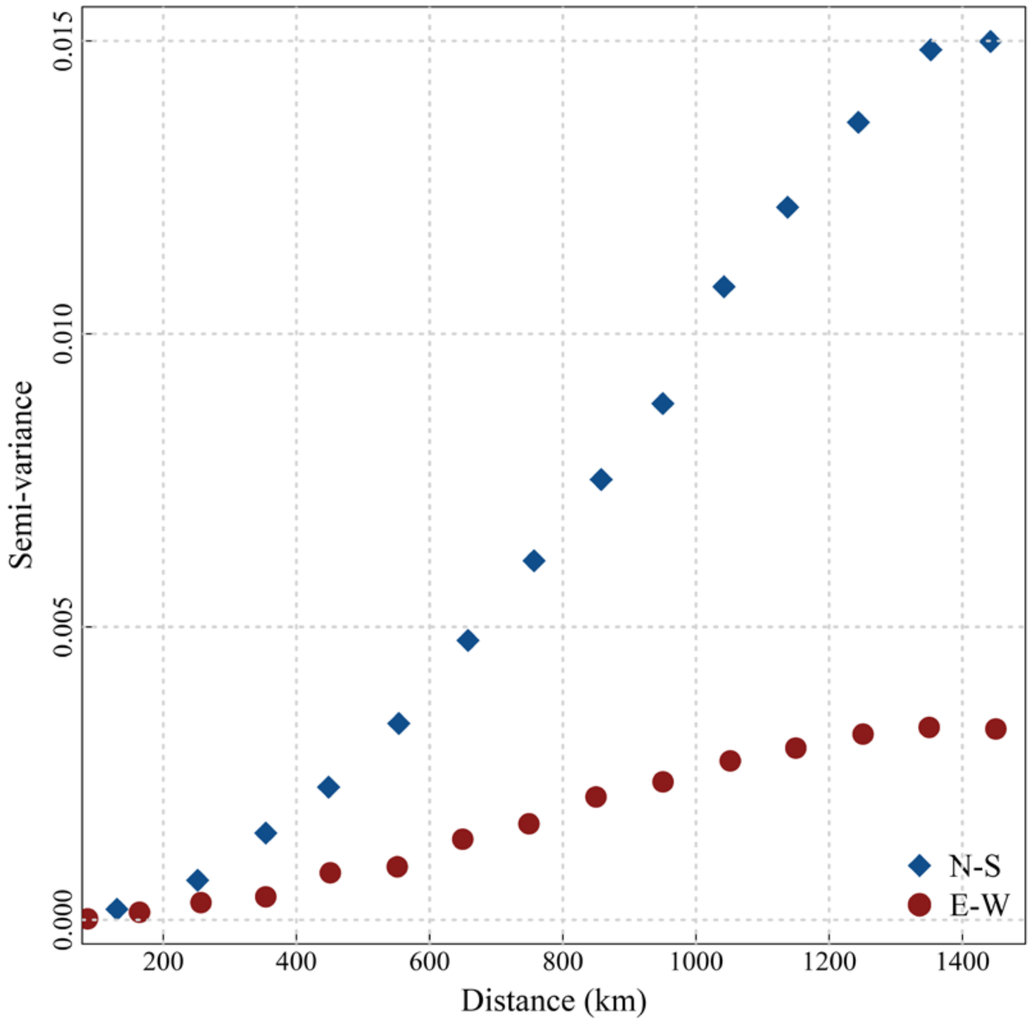

Figure 3.5 Directional semi-variogram for the North Pacific Polar Front Province (Region 16), which is representative of the majority of regions. This highlights the difference in spatial-correlation patterns in the N-S and E-W directions, indicating that a spatio-temporal model that allowed for anisotropic spatial correlation may improve model fit.

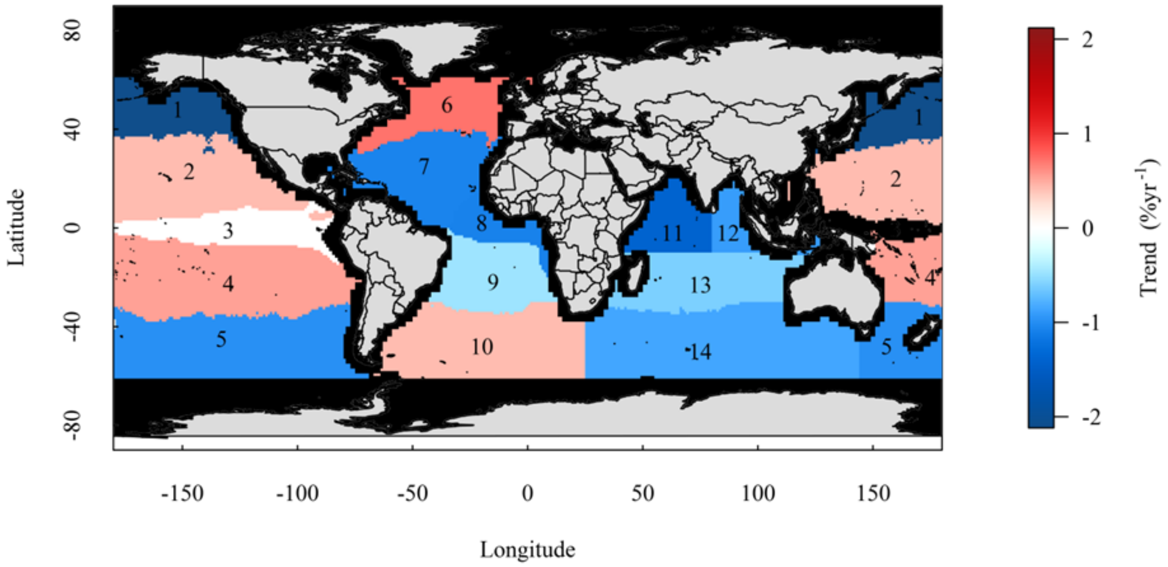

Figure 3.6 Magnitude of the chl trend detected in each region (Sep 1997 - Dec 2013) for the boundaries as defined in Henson et al. (2010). Areas of the ocean not defined under these boundary definitions are in black. Regions in white indicate that the absence of a trend is most likely, based on a 95 % credible interval. See Table 3.3 for full list of values and region names.

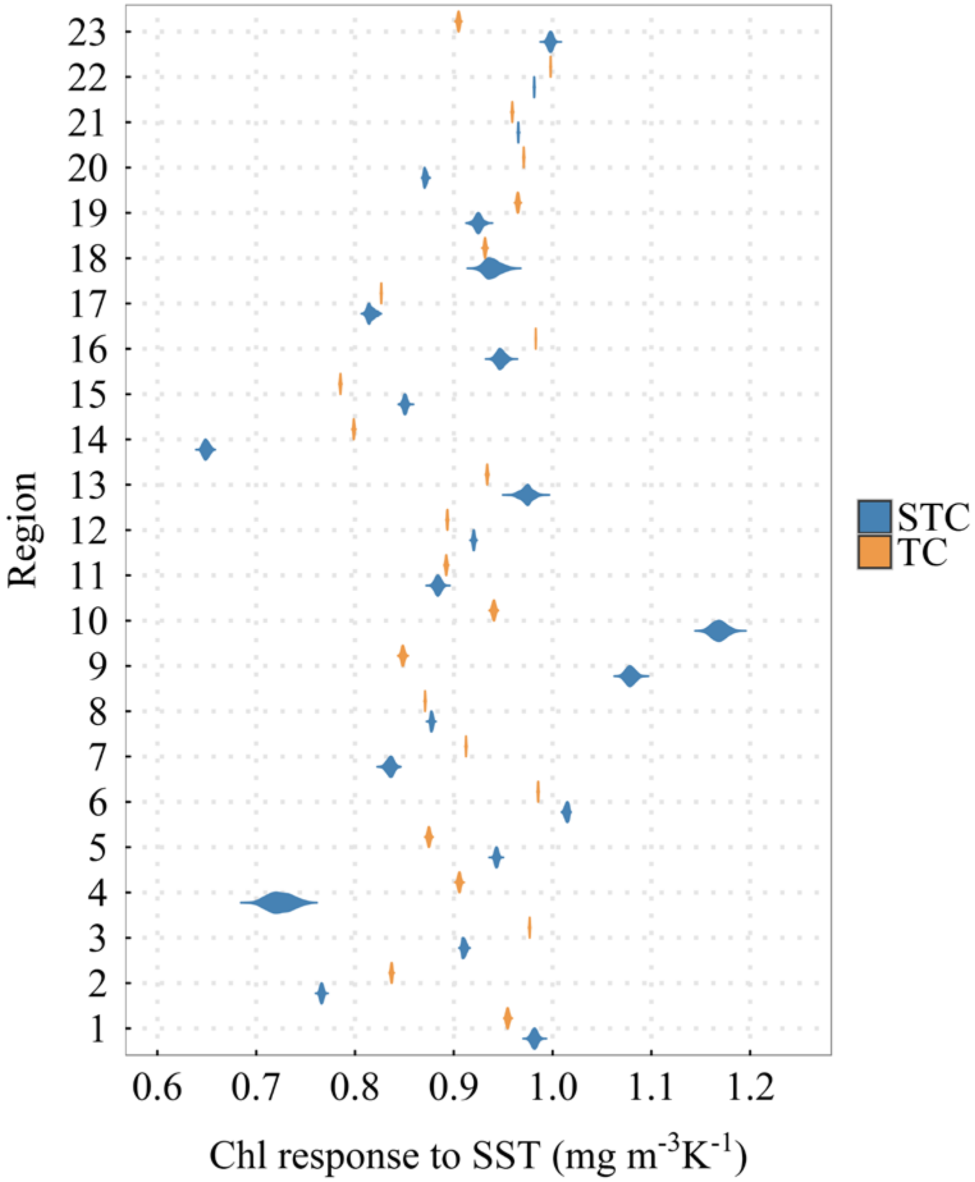

Figure 3.7 Posterior probability densities for the response of chl to SST (i.e. the SST covariate) in each region. Two models are used in each region: STC refers to the model with spatio-temporal correlation and TC refers to the model with temporal correlation only (i.e. without spatial correlation terms). The regions names are defined in Table 2.2.

Chapter 4: Global Ocean Colour Trends and Associated Uncertainties Constrained Using Biogeochemical Models

This chapter is, at the time of writing, in preparation for publication in *Geophysical Research Letters* as:

Hammond, M. L., Beaulieu, C., Henson, S. A., & Sahu, S. K. Global ocean colour trends and associated uncertainties constrained using biogeochemical models.

MLH was responsible for the analysis and writing. CB & SKS were responsible for guidance with the statistical technique and theory. CB & SAH were responsible for guidance with the theory and interpretation of biogeochemistry.

4.1 Abstract

Satellite ocean colour records provide detailed coverage of ocean chlorophyll. However, the short length of these records makes detecting long-term trends challenging. Coupled physical-biogeochemical models can provide multi-decadal ocean simulations which may help separate long-term trends from decadal variability. Trends in CMIP5 models over the period 1979 – 2033 are incorporated as priors in to a Bayesian spatio-temporal analysis of ocean chlorophyll trends. A global average chlorophyll trend of 0.29 % yr^{-1} is found, with trends typically positive in high and mid latitudes. Introducing priors tends to reduce trend estimate magnitude (by 0.040 % yr^{-1} average) and uncertainty (by -0.028 % yr^{-1} average). However, the trend magnitude reduction is not statistically different from zero in any region. Estimated trends are also shown to be statistically different from the model prior information in 15 of 23 regions. Longer records and better model representations of biology and physics may help reconcile these differences in future.

4.2 Introduction

Primary production (PP) by phytoplankton comprises approximately half of the global total biospheric production and is vital to most marine ecosystems (Behrenfeld et al., 2001; Field et al., 1998). It is thus important to determine whether phytoplankton abundance is changing and, if so, how rapidly.

Chlorophyll-a concentration (chl), a proxy for phytoplankton abundance, is used in studies of trends as it can be measured regularly from satellites at a global scale (Gregg et al., 2003); it is thus listed as an essential climate variable (Bojinski et al., 2014). As phytoplankton form the base of the marine food web and are mechanistically linked with fishery yield (Friedland et al., 2012) any changes could have a strong effect on future marine fish stocks (Cheung et al., 2010).

Biogeochemical models can be used to project future change as well as to investigate trends over historical periods. Using prescribed atmospheric forcing, the hindcast simulation by Laufkötter et al. (2013) showed a PP decrease of 6.5 % over the last 40 years (1960 - 2006). Modelling projections, to the end of the 21st Century, with multiple different parameterizations of marine ecosystems have shown either a global PP decrease of 2 to 20 % (Bopp et al., 2013; Steinacher et al., 2010), or a combination of both PP increases and decreases, varying regionally (Laufkötter et al., 2015). Using an empirical model linking phytoplankton changes directly to climate indicators, Sarmiento et al. (2004) projected a 0.7 - 8.1 % increase in global PP from 1860 to 2050.

Observational data allow us to obtain the best possible understanding of ongoing changes in phytoplankton abundance. Ocean colour satellite records can provide the best information source for understanding the long-term response of phytoplankton abundance to global climate forcing, due to their large spatial coverage and temporal resolution (e.g. McClain, 2009; Siegel et al., 2013). However, the short record length and large natural variability of chl can make trend estimation challenging (e.g. Beaulieu et al., 2013; Henson et al., 2010; Mélin, 2016; Saulquin et al., 2013). In an analysis of published phytoplankton trend estimates, Boyce & Worm (2015) found that trends estimated from longer time-series show less variability and are of lower magnitude than trends estimated from shorter time-series. Many studies have been conducted on widely available satellite data, although no consensus on the nature of a global phytoplankton abundance trend has been reached. A positive trend was reported by Antoine et al. (2005), using data from both Coastal Zone Color Scanner (CZCS) (1979 - 1986) and Sea-viewing Wide Field-of-view Sensor (SeaWiFS) (1998 - 2002). A positive but much smaller trend was also reported by Saulquin et al. (2013) combining data from SeaWiFS and Medium Resolution Imaging Spectrometer (MERIS) (1998 - 2011). Using solely SeaWiFS data Behrenfeld et al. (2006) and Vantrepotte & Mélin (2011) found that PP and chl show an overall decrease over the periods 1999 - 2006 and 1997 - 2007 respectively. A similar trend was found by Gregg & Rousseaux (2014) using data from SeaWiFS and Moderate Resolution Imaging Spectroradiometer (MODIS) over the period 1998 - 2012, although an updated study (1998 - 2015) found no significant trend (Gregg et al., 2017). Decreases in chl have also been reported in most oligotrophic gyres by Signorini et al. (2015) using data from the SeaWiFS and MODIS sensors (1998 - 2013). Studies using robust statistical analysis have shown that no global trend can be distinguished from noise in the period 1998 - 2007 (Beaulieu et al., 2013). It has been suggested that a global average of 31.5 years of data is required to distinguish a climate change driven chl trend from background variability (Henson et al., 2010; 2016), substantially longer than the ~20 year record available at the time of writing.

In order to better assess trends in global ocean colour data, a Bayesian spatio-temporal model is used. These models have been shown to produce a more accurate fit to chl observation than statistical models that do not account for spatial relationships within the data and, in addition, they provide a full assessment of uncertainty (Hammond et al., 2017). In order to compensate for the shortness of the ocean colour record, output from the IPCC Coupled Model Intercomparison Project (CMIP5) models is used to provide Bayesian priors. A combination of Historical and RCP8.5 scenarios from the available CMIP5 model runs are used in order to inform the statistical model.

4.3 Material & Methods

4.3.1 Data

The data for chl are sourced from the ESA OC-CCI v3.1 product (Lavender et al., 2015; available at: http://www.esa-oceancolour-cci.org/). This dataset combines the SeaWiFS, MERIS, MODIS, and Visible Infrared Imaging Radiometer Suite (VIIRS) sensors using band-shifting and bias-correction techniques to create a monthly time-series from September 1997 to December 2016 inclusive. The data is downscaled to a 1° grid by averaging within 1° boxes.

Model data comes from CMIP5 models (sourced from https://esgf-node.llnl.gov/projects/cmip5/), see Table 2.1 for a full list of models used. Models and ensembles with available monthly chl output, run under the RCP8.5 and historical scenarios, were used. RCP8.5 and historical outputs are joined, omitting data outside the period of interest, to create a continuous dataset covering 1979 – 2033 (global average time-series can be found in Appendix B.1). This range was selected to cover the observational period and to provide sufficient length either side to isolate interannual variability. The year 2033 was chosen as the upper time limit due to the large increase in inter-model uncertainty after this point (see Figure 1.3), and the lower limit of 1979 was chosen to provide similar lengths before and after the observational period. The model grid outputs were interpolated to match the 1° grid spacing of the satellite data. Model output was analysed as detailed in Section 4.3.2. A log-transformation of the chl data is used, for both observational and model output, after Campbell (1995).

Sea Surface Temperature (SST) is also included as a covariate, see details in Section 4.3.2. For the observational data, SST data are from the NOAA optimum interpolation v2 product (Reynolds et al., 2002; available at: http://www.esrl.noaa.gov/psd/data/gridded/data.noaa.oisst.v2.html). In addition, SST output from the same CMIP5 models is used, treated in the same way as above, to assist in the estimation of trends in the models. Monthly means are used in all datasets.

Trends in 23 open ocean regions are analysed, with boundaries defined as in Longhurst (1995; 1998), see Table 2.2. The province approach was chosen as these regions are defined by characteristic physical forcing and biogeochemical factors. Coastal and polar waters were omitted due to issues with data availability and quality. For full details behind the selection of regions see Section 2.1.

4.3.2 Model Formulation

In each of the 23 Longhurst regions selected for study a hierarchical Bayesian spatio-temporal model is fitted. For full details of the model setup used see Section 2.2. Equation 1 represents the first level or data level, where the relationship between the observed chl $Z_{n,t}$, at location n and at month t, and its true value $O_{n,t}$ and random measurement error $\varepsilon_{n,t}$ is stated:

$$Z_{n,t} = O_{n,t} + \varepsilon_{n,t} \qquad (1)$$

The true value is represented by the following regression model:

$$O_{n,t} = \boldsymbol{x}'_{n,t}\boldsymbol{\beta} + \boldsymbol{a}'_n \boldsymbol{w}_{m,t} \qquad (2)$$

Where $\boldsymbol{x}_{n,t}$ represents the covariates and intercept, $\boldsymbol{\beta}$ represents the regression coefficients, and the term $\boldsymbol{a}_n'\boldsymbol{w}_{m,t}$ represents spatial and temporal correlation. The spatial correlation is represented by an exponential decay away from site n, and the temporal correlation by an AR(1) process. The selected covariates are: the time of the observation, a monthly factor (constant for all years), and SST. These covariates are selected for the following reasons: time allows the estimation of the temporal trend, the monthly factor is a representation of seasonal cyclicity, and SST allows longer-term environmental variability to be taken into account. These covariates are used in all regions, except in the Pacific Subarctic Gyres Province (East) (Region 18) where the monthly factor is omitted due to anomalous phenology (see Section 2.2).

Underlying these equations is a distribution from which the model draws samples. These prior distributions can be used to represent existing understanding, or left vague to represent no clear previous understanding (i.e. a vague prior). The prior distribution used here is represented by a normal distribution with a specified mean and variance. A mean trend of 0 % yr^{-1} and a large variance (100) is used for the vague prior. Additionally, CMIP5 model output is used to provide prior information. The period 1979 - 2033, combining RCP8.5 and historical scenarios, is used to completely cover the observational period and allow a sufficiently long record to best isolate trends from interannual variability. A statistical model with negligible spatial correlation, similar to the model used as a comparison in Chapter 3, is fitted for each CMIP5 model, ensemble, and Longhurst region. Spatial correlation terms were omitted due to the high computational cost from the longer time-series and number of models, which is expected to result in a loss of useful information, although the longer time-series should compensate for this. Individual ensembles are averaged per model, to avoid adding additional weight to individual models, before a multi-model mean and variance is calculated to provide information for a prior. A complete list of prior estimates is included in Table 4.1.

The Bayesian statistical model estimates a posterior distribution for each parameter. This study is focused on the trend parameter. The posterior mode of the trend parameter represents the best estimate of the trend. The uncertainty of the trend parameter is represented by the 95 % credible interval which is defined as the 95 % highest density interval (HDI) (Kruschke, 2015). To assess the effect of introducing the CMIP5 prior information, results for the statistical model with the CMIP5 priors are compared with results from a statistical model with vague priors. To evaluate whether trends are likely to be different in the two scenarios their 95 % credible intervals are compared to determine if there is no overlap.

The model fit was estimated in R using the spTimer package. For full details on the package and model setup see Bakar & Sahu (2015) and Section 2.2.

4.4 Results

4.4.1 Prior Information from CMIP5 Models

The prior information obtained from the CMIP5 models is shown in Figure 4.1 and Table 4.1. Modal prior trends are all of greater magnitude than the vague priors used in Chapter 3 (which are also used as a comparison in this chapter). The vague priors all have a mean value of 0.0 % yr $^{-1}$ whilst the average magnitude of the CMIP5 prior trends is 0.14 % yr $^{-1}$. Although the CMIP5 priors are larger than the vague priors, they are still smaller than the average magnitude of trends estimated from the observations using the vague priors (0.65 % yr $^{-1}$). Conversely, the variances of the priors obtained from the CMIP5 models (0.21) are substantially smaller than the vague priors (100). The effect on trend estimates by using the CMIP5 prior information is considered in the next section.

4.4.2 Trend Estimates with Priors

The statistical model with CMIP5 model priors estimates a global weighted average trend of 0.29 % yr $^{-1}$, a net positive trend (Figures 4.2 & 4.3a). The weighting is based on the average chl and area in each region. There is regional variability around the global trend, including several regions with a negative trend. The regions with negative trends are the Indian South Subtropical Gyre Province (Region 3) (-0.47 % yr $^{-1}$), the North Pacific Equatorial Countercurrent Province (Region 5) (-0.87 % yr $^{-1}$), the North Pacific Tropical Gyre Province (Region 6) (-1.1 % yr $^{-1}$), the Pacific Equatorial Divergence Province (Region 7) (-1.2 % yr $^{-1}$), the North Pacific Subtropical Gyre Province (West) (Region 17) (-0.33 % yr $^{-1}$), and the Eastern Tropical Atlantic Province (Region 1) (-0.28 % yr $^{-1}$). See Table 4.2 for a complete list of estimated trends, both with and without CMIP5 priors.

The Atlantic mostly contains regions with positive trends, e.g. the Gulf Stream Province (Region 11) (0.61 % yr $^{-1}$), the North Atlantic Drift Province (Region 13)

(0.92 % yr^{-1}), the North Atlantic Subtropical Gyral Province (East) (Region 14) (0.88 % yr^{-1}), the North Atlantic Tropical Gyral Province (Region 4) (0.53 % yr^{-1}), the Western Tropical Atlantic Province (Region 10) (0.72 % yr^{-1}), and the South Atlantic Gyral Province (Region 8) (0.42 % yr^{-1}). The South Pacific Subtropical Gyre Province (Region 20) (0.82 % yr^{-1}) and the Southern Ocean, specifically the South Subtropical Convergence Province (Region 21) (0.83 % yr^{-1}) and the Subantarctic Province (Region 22) (1.3 % yr^{-1}), also show positive trends. High latitudes are typically positive except in the Northern Pacific Ocean, where the outlook is mixed, i.e. the Pacific Subarctic Gyres Province (East) (Region 18) has a positive trend (0.48 % yr^{-1}) and the trend in the Pacific Subarctic Gyres Province (West) (Region 19) is not statistically different from zero (0.013 % yr^{-1}).

4.4.3 Uncertainty in Trend Estimates

The global average uncertainty estimated by the statistical model with CMIP5 priors is 0.34 % yr^{-1}. The regional pattern of uncertainty is more complex and does not seem to be related to trend magnitude (Figures 4.2 and 4.3b). Uncertainty tends to be highest in the eastern North Atlantic, i.e. in the North Atlantic Drift Province (Region 13) (0.57 % yr^{-1}) and the North Atlantic Subtropical Gyral Province (East) (Region 14) (0.58 % yr^{-1}). There is also high uncertainty in the western and north-most North pacific: the Kuroshio Current Province (Region 12) (0.56 % yr^{-1}), the Pacific Subarctic Gyres Province (West) (Region 19) (0.57 % yr^{-1}), and the Pacific Subarctic Gyres Province (East) (Region 18) (0.50 % yr^{-1}). Conversely, uncertainty is lowest in the Southern Ocean (i.e. the South Subtropical Convergence Province (Region 21) (0.16 % yr^{-1}) and the Subantarctic Province (Region 22) (0.041 % yr^{-1})) as well as in parts of the equatorial and northern Pacific, i.e. the Pacific Equatorial Divergence Province (Region 7) (0.12 % yr^{-1}), the North Pacific Polar Front Province (Region 16) (0.17 % yr^{-1}), and the North Pacific Subtropical Gyre Province (West) (Region 17) (0.19 % yr^{-1}). See Table 4.2 for a complete list of trend estimate uncertainties, both with and without CMIP5 priors.

4.5 Discussion

4.5.1 Effect of Priors

The effect of including priors is revealed by comparing the statistical models with and without CMIP5 model prior information (Figures 4.2 and 4.4). The mean trend in the model with CMIP5 priors is 0.010 % yr^{-1}, with a mean magnitude of 0.13 %

yr^{-1} (see Table 4.1 for a complete list of the prior information). The mean trend in the statistical model with vague priors is 0.18 % yr^{-1}, with a mean magnitude of 0.29 % yr^{-1}. The differences between the trend magnitudes in the two models average -0.040 % yr^{-1} (i.e. lower magnitude in the model with CMIP5 prior information). Trend differences are negative in 8 of the 23 regions, positive in 11 of the 23 regions and neutral in 4 others. The differences in trend seem to be primarily in the direction of zero, i.e. reducing in magnitude. This reduction in magnitude appears to primarily result from the very low magnitude variance of the priors (0.21). The small variance of the CMIP5 prior information, relative to the vague prior, creates an inward pressure on the probability densities, effectively pushing the trends towards zero. This is despite the fact that the average prior trend magnitude is higher when using the CMIP5 priors (0.14 % yr^{-1}) than the vague priors (0.0 % yr^{-1}). However, all these differences are small and the trend estimates with and without CMIP5 prior information are not deemed statistically different.

The introduction of CMIP5 priors leads to a mean reduction in uncertainty of 0.027 % yr^{-1}; this is a reduction in 13 of the 23 regions (i.e. 56 % of regions) (Figures 4.2 and 4.4). In the model with vague priors the variance is 100, whereas the CMIP5 priors have an average variance of 0.21. Even the largest variance of the CMIP5 priors is 1.2, substantially smaller than the variance in the vague prior. A reduction in uncertainty of the trend estimates is expected as the priors allow us to constrain trend values, although this does not happen in all regions. Prior information was calculated from CMIP5 models using a statistical model without spatial correlation, for computational efficiency. If spatial correlation was included in the statistical model estimating trends in the CMIP5 models it would be expected to increase the variance of the prior information derived from CMIP5 models, which may mean the use of CMIP5 prior information no longer lead to a mean reduction in trend estimate uncertainty.

When comparing the statistical models, with and without CMIP5 model prior information, no regions were found to have statistically different trends. The ability of CMIP5 models to recreate chl observations is examined to assess the usefulness of the CMIP5 prior information. To do this a Taylor diagram for the models is plotted in Figure 4.5 (Taylor, 2001). Taylor diagrams are widely used in climate sciences to summarise model performance, relative to observations, using the metrics: Pearson Correlation Coefficient (PCC), RMSE, and standard deviation.

Figure 4.5 shows the poor PCC when comparing model output with observations (maximum value of 0.4 in the CNRM model, only 5 of the models show a PCC greater than 0.2). Additionally, all models have a RMSE greater than 2 mg m^{-3}. Finally, all models have a much lower standard deviation than observations, with the exception of the MPI ESM LR and MPI ESM MR models, whose standard deviations are only slightly lower than observations. The lower standard deviations in the model output may result from underestimation of the chl peaks seen in observations, reducing overall variability. In summary CMIP5 models show, compared to observations: a poor correlation, a large deviation, and a smaller degree of variability. Thus, models show poor skill at reproducing the ocean colour chl observations. This poor skill at reproducing chl observations may also indicate a limited ability to reproduce long-term trends in chl, biasing the prior information used. Therefore, it seems that substantial improvements must be made to the biogeochemical components of biogeochemical-physical models in order to allow them to more successfully recreate observations, which would allow them to provide improved prior information.

A sensitivity test was performed in order to analyse the effect of incorporating priors (Tables 4.3 & 4.4). This is done by analysing certain regions in the statistical model for a range of prior mean and variance values before examining the resulting trend estimates and their uncertainties. For example, in the Tasman Sea Province region (Region 23), a prior variance of greater than 0.1 has very limited effect on the trend estimates. There is a degree of variability in these estimates caused by using fewer iterations in the test (10,000 vs 40,000 in the main analysis). Priors with smaller variances have more effect on the trend estimates, reaching a maximum when prior variances are 0.001 where trend estimates and prior means are approximately the same. Although the CMIP5 priors provide a much smaller variance (average of 0.21) than the vague priors (100), their variance is still too large in most cases to have a significant effect on the trend estimates. In future, greater consistency between the CMIP5 model trend estimates is required for them to have greater influence on chl trend estimates as Bayesian priors.

4.5.2 Global Trends and Other Studies

This study estimates trends that are on average more positive than a number of previous studies. Previous studies that report similar global positive trends include Saulquin et al. (2013), using SeaWiFS and MERIS data over the period

1998 - 2011, and Hammond et al. (2017) using version 2.0 of the ESA OC-CCI dataset, covering Sep 1997 - Dec 2013. The study using the longest ocean colour dataset, other than the present study, is Gregg et al. (2017) which uses SeaWIFS and MODIS data over the period 1998 - 2015. Gregg et al. (2017) reported no globally significant trend, albeit within a considerably different statistical framework to the present study.

On a regional scale it is interesting to note that the Indian Ocean is estimated to have negative trends in a number of studies, although not always over the whole region (e.g. Gregg & Rousseaux, 2014; Hammond et al., 2017; Saulquin et al. 2013; Siegel et al., 2013; Signorini et al., 2015; Vantrepotte & Mélin, 2011). However, in the studies by Henson et al. (2010; 2016) which estimated the record length required to unambiguously distinguish a trend signal from environmental variability, the Indian Ocean is found to be one of the latest to emerge (i.e. it requires 40 years of record). There is also consistency in the sign of estimated trends in northern hemisphere western subtropical gyres (e.g. Gregg & Rousseaux, 2014; Hammond et al., 2017; Siegel et al., 2013; Signorini et al., 2015; Vantrepotte & Mélin, 2011). In Henson et al. (2010), the northern hemisphere oligotrophic regions are estimated to require 37 – 39 years of record length in order for a trend to be distinguished from environmental variability. The consistency in the sign of estimated trends between records of various lengths suggests trends may be beginning to emerge from natural variability in these regions.

In other regions of the globe there is typically disagreement in the estimated trends compared with other studies. This can be explained by both the different statistical approach and longer record length used in the present study. The only other study using a similar methodology is Hammond et al. (2017). However, this uses ESA OC-CCI v2.0 dataset, which is 4 years shorter than the ESA OC-CCI v3.1 dataset, does not include the VIIRS sensor, and has uncorrected decay in MODIS data (Mélin et al., 2017). The ESA OC-CCI v3.1 dataset includes the large El Niño event in 2015/2016, and also starts with a similarly large event (in 1997/1998); such oscillations can have a key effect on trend detection.

4.6 Conclusion

Trends in global ocean colour data, over the period 1997 - 2016, are assessed using a Bayesian spatio-temporal model. Bayesian prior information is provided by the analysis of chl trends in CMIP5 model output covering the period 1979 - 2033. A global average weighted trend of 0.29 % yr^{-1} is found. This is part of a global pattern that tends to show positive trends at high and mid latitudes. The introduction of priors reduces trend magnitude by an average of 0.040 % yr^{-1} and trend estimate uncertainty by an average of 0.027 % yr^{-1}. However, the reduction in trend magnitude is not statistically different from zero in any region.

In the majority of regions studied, the estimated trends in observations are different from the estimated trends in CMIP5 model output. This suggests, alongside the increases in uncertainty seen in some regions when using CMIP5 information as priors, that there is a disagreement between modelled and observed chl trends. This disagreement implies that either observational records are not yet long enough to detect long-term trends or models are not accurately simulating trends. The poor ability of models to reproduce chl observations may indicate it is the latter.

In either case a Bayesian spatio-temporal model provides a promising framework for using both model and observational information to improve estimates of climate change driven trends and uncertainties. Improvements to this technique could be made by using models that are better able to reproduce chl observations, reducing inter-model trend estimate uncertainty, and by incorporating in situ data as Bayesian priors. Alternatively, merging satellite data with longer-term in situ records may be an approach to improve the estimation of chl trends within this framework.

4.7 Tables

Table 4.1 Full list of modal trends and their 95 % credible interval (CI) boundaries, for the CMIP5 models. See Table 2.2 for region names.

Region	Trend Value (% yr $^{-1}$)	Lower CI Boundary (% yr $^{-1}$)	Upper CI Boundary (% yr $^{-1}$)
1	0.32	-0.13	0.75
2	0.44	0.11	0.77
3	0.094	-0.018	0.21
4	0.19	-0.27	0.66
5	0.31	-0.37	1.0
6	0.15	0.019	0.29
7	0.092	-0.66	0.89
8	-0.089	-0.24	0.064
9	0.41	0.18	0.65
10	0.43	-0.056	0.92
11	-0.16	-0.27	-0.056
12	0.084	0.023	0.15
13	-0.14	-0.56	0.3
14	-0.42	-2.8	2.0
15	-0.065	-1.2	1.0
16	0.13	-0.070	0.33
17	0.21	-0.79	1.2
18	-0.049	-0.13	0.024
19	0.051	0.015	0.084
20	0.040	-0.013	0.094
21	0.093	0.069	0.12
22	-0.017	-0.11	0.077
23	0.15	0.11	0.19

Table 4.2 Full list of modal trends and their 95 % credible interval (CI), for the statistical model with vague priors, and the statistical model with CMIP5 priors. See Table 2.2 for region names

	Model with Vague Priors			Model with CMIP5 Priors		
Region	Trend Value (% yr $^{-1}$)	Lower CI Boundary (% yr $^{-1}$)	Upper CI Boundary (% yr $^{-1}$)	Trend Value (% yr $^{-1}$)	Lower CI Boundary (% yr $^{-1}$)	Upper CI Boundary (% yr $^{-1}$)
1	-0.32	-0.51	-0.068	-0.28	-0.49	-0.055
2	-0.086	-0.29	0.040	-0.061	-0.23	0.078
3	-0.52	-0.68	-0.39	-0.47	-0.63	-0.35
4	0.52	0.38	0.68	0.53	0.36	0.66
5	-0.87	-1.1	-0.70	-0.87	-1.1	-0.66
6	-1.2	-1.4	-1.1	-1.1	-1.3	-0.96
7	-1.3	-1.3	-1.2	-1.2	-1.3	-1.2
8	0.46	0.33	0.58	0.42	0.29	0.55
9	-0.066	-0.27	0.15	0.060	-0.25	0.23
10	0.72	0.57	0.87	0.72	0.55	0.86
11	0.74	0.56	0.93	0.61	0.44	0.79
12	-0.16	-0.67	0.41	-0.00071	-0.28	0.28
13	1.0	0.73	1.3	0.92	0.68	1.3
14	0.99	0.7	1.3	0.88	0.62	1.2
15	-0.22	-0.38	-0.031	-0.16	-0.36	0.0017
16	1.0	0.94	1.1	1.0	0.93	1.1
17	-0.29	-0.43	-0.22	-0.33	-0.42	-0.23
18	0.67	0.36	0.92	0.48	0.20	0.70
19	-0.37	-0.54	-0.17	0.013	-0.26	0.31
20	1.1	0.98	1.3	0.82	0.70	0.98
21	0.93	0.83	1.0	0.83	0.74	0.90
22	1.3	1.3	1.4	1.3	1.3	1.4
23	0.051	-0.15	0.21	0.071	-0.08	0.22

Table 4.3 Example sensitivity analysis showing the effect, on the best trend estimate, of a range of mean and variance values in the trend prior distribution. This example is for the Tasman Sea Province region (Region 23), although similar results are found in other regions. The trend estimate approaches the prior mean with a degree inversely proportional to the prior variance. The table reports trend values in % yr^{-1}, calculated in units of $\log(\text{mg m}^{-3})$ per month.

	Prior Variance						
	0.0001	0.001	0.01	0.1	1	10	100
Prior Mean (% yr^{-1})	Trend Estimate (% yr^{-1})						
-5	-4.9	-4.5	-2.4	-0.41	-0.017	0.014	0.039
-1	-0.99	-0.90	-0.46	-0.051	0.032	0.039	0.031
-0.5	-0.49	-0.45	-0.22	-0.004	0.034	0.034	0.051
-0.1	-0.097	-0.089	-0.033	0.024	0.047	0.038	0.025
-0.05	-0.049	-0.039	-0.014	0.025	0.028	0.036	0.017
-0.01	-0.0089	-0.0089	0.010	0.028	0.027	0.047	0.023
0	-0.00095	0.0033	0.0075	0.022	0.047	0.036	0.021
0.01	0.010	0.016	0.021	0.035	0.026	0.051	0.034
0.05	0.049	0.053	0.039	0.033	0.045	0.038	0.039
0.1	0.098	0.094	0.074	0.056	0.051	0.040	0.040
0.5	0.49	0.45	0.25	0.075	0.028	0.031	0.038
1	0.99	0.91	0.50	0.12	0.063	0.045	0.034
5	4.9	4.5	2.4	0.46	0.065	0.051	0.037

Table 4.4 Example sensitivity analysis showing the effect, on the trend uncertainty, of a range of mean and variance values in the trend prior distribution. This example is from the Tasman Sea Province region (Region 23), although similar results are found in other regions. The prior mean does not affect the trend uncertainty. The uncertainty appears to decrease proportionally with the prior variance. However prior variances of greater than 0.1 seem to have a relatively limited effect on the trend credible interval width. The table reports credible interval widths in % yr^{-1}, calculated in units of log(mg m^{-3}) per month.

	Variance						
	0.0001	0.001	0.01	0.1	1	10	100
Prior Mean (% yr^{-1})	Trend Uncertainty (% yr^{-1})						
-5	0.039	0.12	0.28	0.36	0.37	0.37	0.37
-1	0.039	0.11	0.27	0.36	0.37	0.36	0.36
-0.5	0.039	0.12	0.27	0.35	0.37	0.36	0.37
-0.1	0.039	0.12	0.27	0.35	0.37	0.37	0.38
-0.05	0.039	0.12	0.27	0.36	0.39	0.37	0.38
-0.01	0.039	0.12	0.27	0.36	0.37	0.37	0.37
0	0.038	0.12	0.27	0.35	0.37	0.37	0.37
0.01	0.039	0.12	0.27	0.36	0.37	0.37	0.37
0.05	0.039	0.12	0.27	0.36	0.36	0.37	0.38
0.1	0.039	0.12	0.27	0.36	0.38	0.38	0.37
0.5	0.039	0.12	0.27	0.35	0.37	0.36	0.37
1	0.039	0.12	0.27	0.37	0.38	0.37	0.37
5	0.039	0.12	0.27	0.35	0.36	0.36	0.38

4.8 Figures

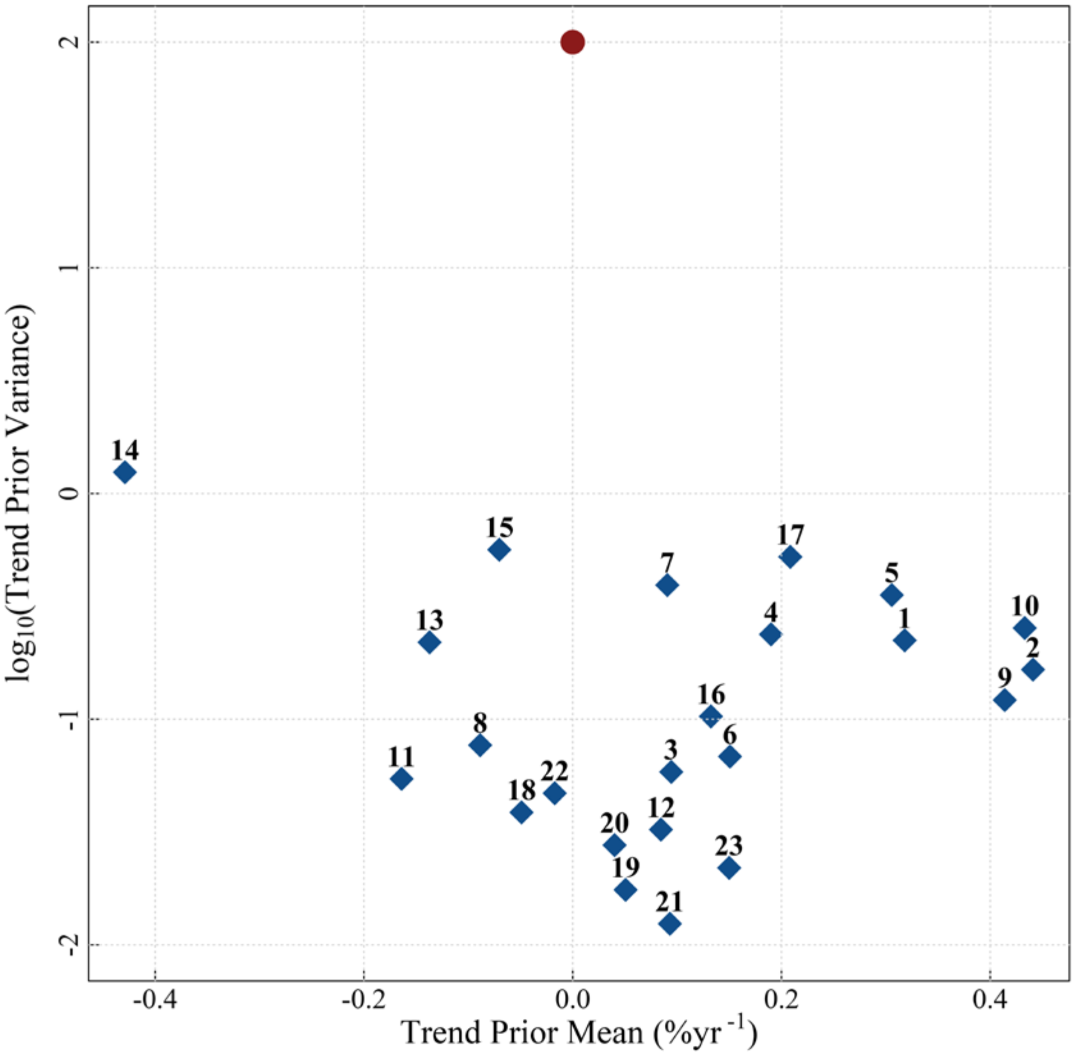

Figure 4.1 Values of mean and variance used in the prior information. The red circle indicates the vague priors used, the blue diamonds indicate the priors, in each region, determined using information from the CMIP5 models. Note that variance is plotted on a logarithmic scale due to there being several orders of magnitude difference between the vague priors and the priors using information from the CMIP5 models. See Table 2.2 for a list of region names.

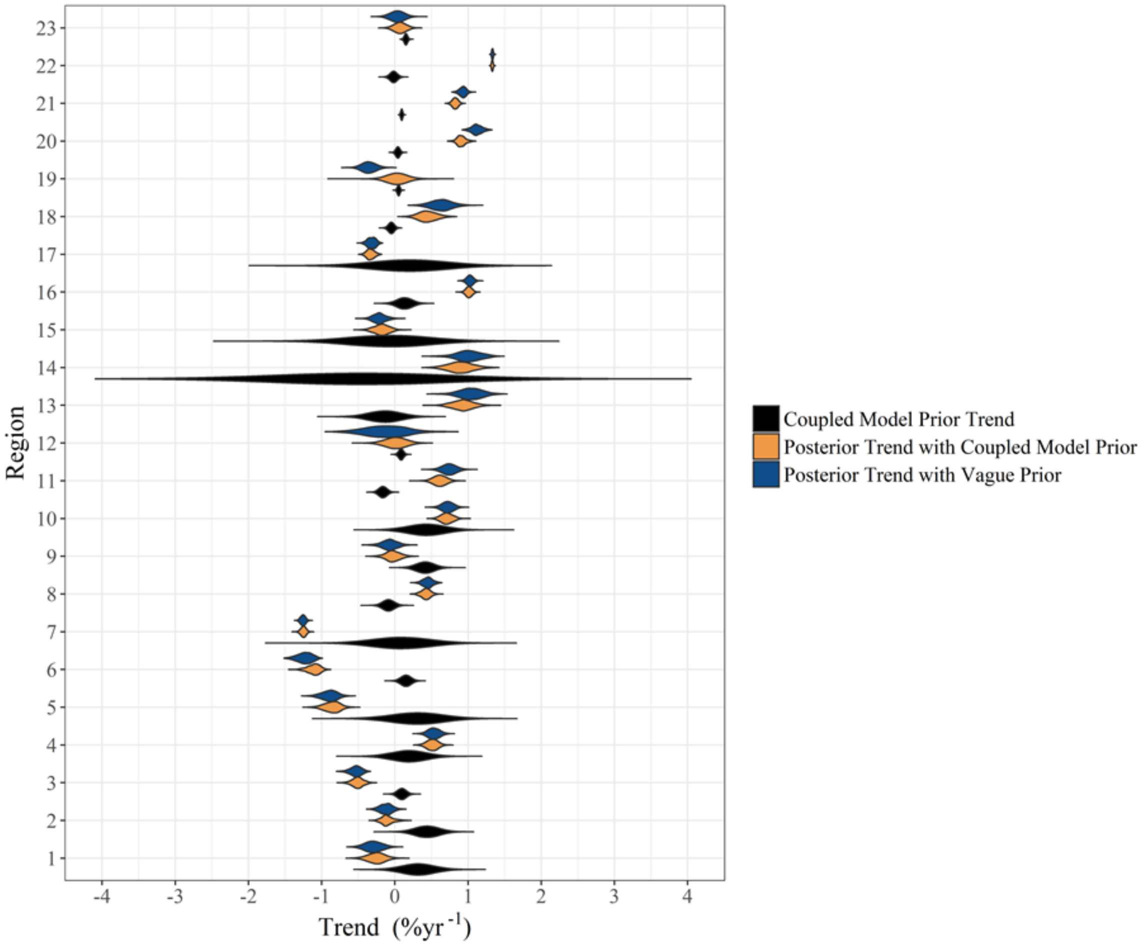

Figure 4.2 Posterior probability density of the trend in the CMIP5 models, used as prior information, and the trend estimate for the statistical models with and without CMIP5 priors. The trend estimates are not statistically different when including CMIP5 prior information. A map of the provinces is provided in Figure 4.3 and a list of region names is provided in Table 2.2. The statistical model with CMIP5 model priors estimates a global weighted average trend of 0.29 % yr^{-1}.

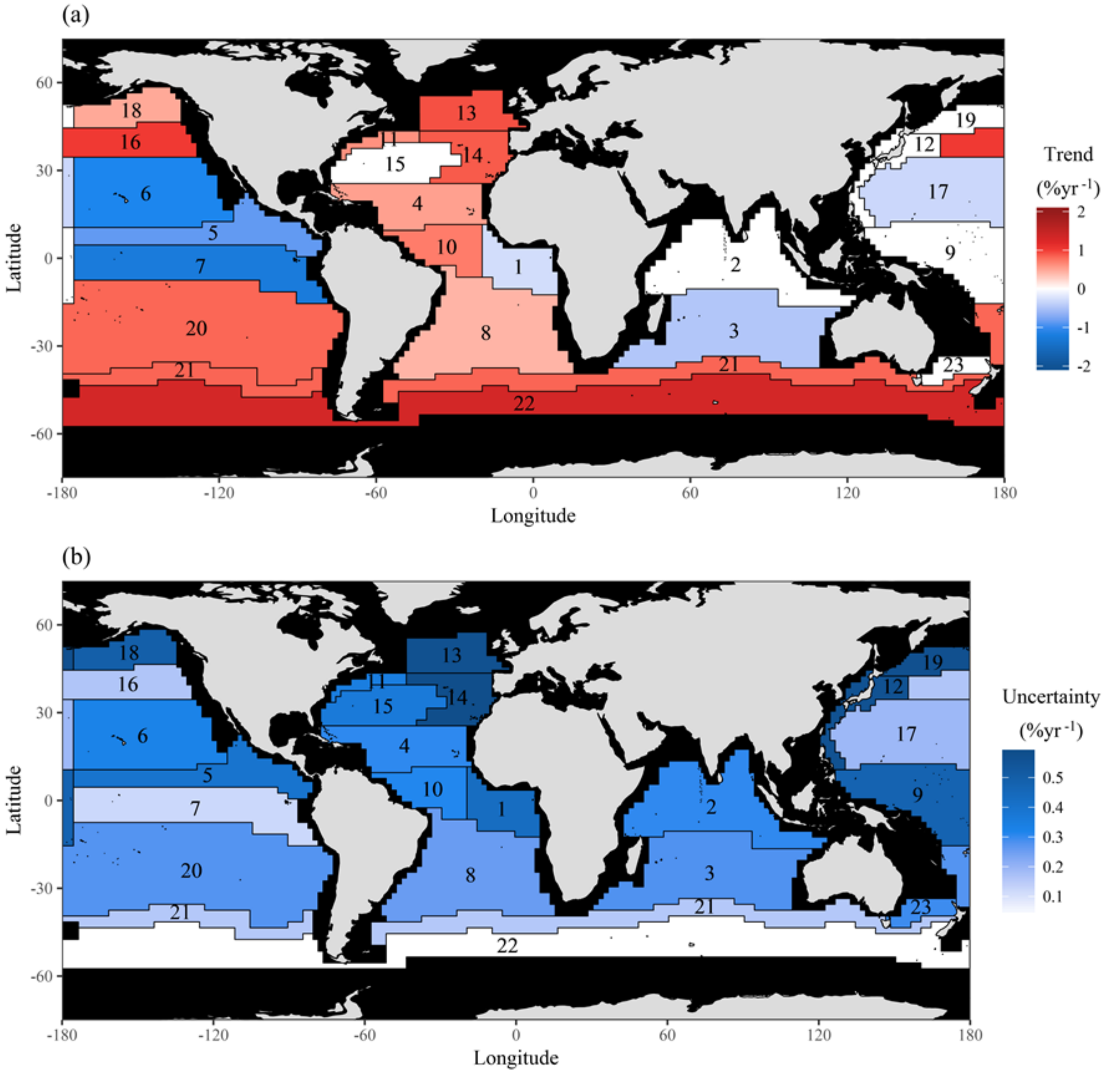

Figure 4.3 The (a) best trend estimate and (b) uncertainty of the trend estimate for the statistical model with CMIP5 priors in each region. Trends are typically more positive at mid to high latitude and average 0.28 % yr^{-1}, with a range of -1.2 % yr^{-1} to 1.3 % yr^{-1}. The uncertainty follows a different pattern, appearing to be partially dependent on ocean region; it is high in the North Atlantic and low in the Southern Ocean. A list of region names can be found in Table 2.2.

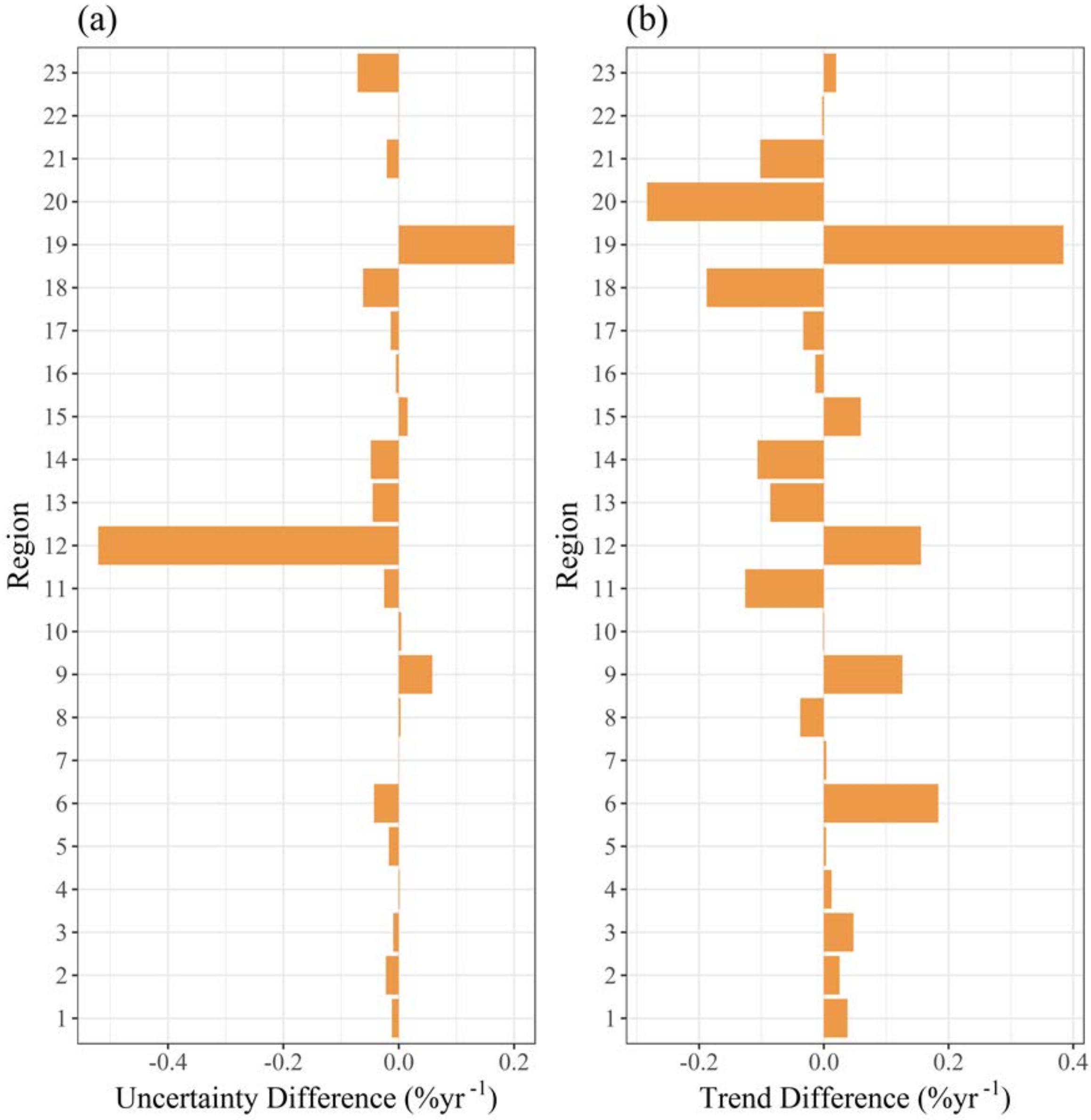

Figure 4.4 The difference in (a) estimated trend uncertainty and (b) their estimated trend, comparing the statistical models with and without CMIP5 priors in each region. A negative difference indicates that the estimated value is smaller in the statistical model with the CMIP5 priors. The introduction of priors tends to decrease trend magnitude by an average of 0.040 % yr^{-1} and to reduce trend estimate uncertainty by an average of 0.027 % yr^{-1}. A map of the provinces is provided in Figure 4.3 and a list of region names is provided in Table 2.2.

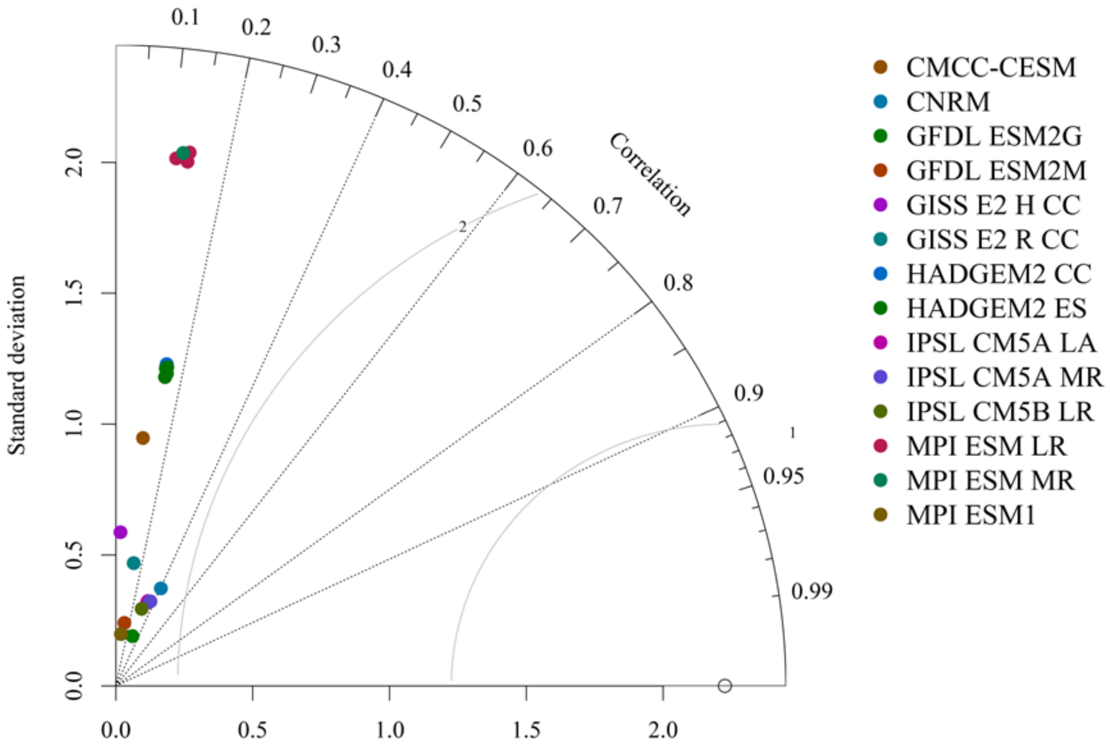

Figure 4.5 Taylor diagram showing the standard deviation (along the radius of the semi-circle) of observational chl data and of the chl output from each CMIP5 model. The observations are marked by the small unfilled circle on the x-axis. The diagram also shows the correlation (along the arc of the semi-circle), and RMSE (radiating from the observation point), between observations and each of the CMIP5 models. Colours represent each of the models listed in Table 2.1. Where a model has multiple ensembles, they are all presented in the same colour. There are two things of particular note: (1) the relatively low agreement between model output and chl observations and (2) the low variability of most models, when compared to observational data.

Chapter 5: Assessing the Effect of Potential Discontinuities in the Ocean Colour Satellite Record on Chlorophyll Trends and Their Uncertainties

This chapter has been previously published in Geophysical Research Letters as:

Hammond, M. L., Beaulieu, C., Henson, S. A., and Sahu S. K. (2018) Assessing the Presence of Discontinuities in the Ocean Color Satellite Record and Their Effects on Chlorophyll Trends and Their Uncertainties, Geophysical Research Letters, 45. DOI: 10.1029/2017GL076928.

MLH was responsible for the analysis and writing. CB & SKS were responsible for guidance with the statistical technique and theory. CB & SAH were responsible for guidance with the theory and interpretation of biogeochemistry.

5.1 Abstract

Ocean colour sensors are crucial for understanding dynamics in global phytoplankton populations. However, the limited lifespans of these sensors make multi-sensor datasets necessary for estimating long-term trends. Discontinuities may be introduced when producing multi-sensor datasets, potentially biasing estimated trends and affecting their uncertainties. A Bayesian spatio-temporal model is used to analyse the effect of discontinuities on estimated chlorophyll trends. The discontinuities considered are the introduction of MERIS, MODIS, and VIIRS, and the termination of SeaWiFS. The presence of discontinuities affects trend estimates (statistically different trends in ~60 % of regions), and can even bias trend estimates (opposite sign in ~13 % of regions). Considering a single discontinuity increases trend uncertainty by an average of 0.20 % yr^{-1} *(0.59 % yr*$^{-1}$ *for two discontinuities). This difference in trend magnitude and uncertainty highlights the importance of minimising discontinuities in multi-sensor records and taking into account discontinuities when analysing trends.*

5.2 Introduction

Ocean colour satellite records can be used to assess how global phytoplankton biomass may be affected by climate change. These records are especially suited to this task because of their high spatial and temporal resolution (e.g. McClain, 2009). However, there are major challenges inherent to trend detection in chlorophyll-a concentration (chl) derived from ocean colour sensors. These include the low signal-to-noise ratio, the large degree of natural variability, and the shortness of the record (e.g. Beaulieu et al., 2013; Henson et al., 2010; Mélin, 2016; Saulquin et al., 2013). A comparison of observational, i.e. in situ and satellite, chl observations found that shorter datasets have conflicting, and larger magnitude, trend estimates when compared to longer records (Boyce & Worm, 2015). The large magnitude of natural variability can obscure a smaller magnitude long-term trend, complicating the estimation of these trends.

To compensate for the shortness of any single ocean colour record, multi-sensor datasets can be used. These combine the available ocean colour sensors using various approaches (e.g. Lavender et al., 2015; Maritorena & Siegel, 2005). The four main ocean colour sensors providing the longest overlapping period of coverage to date are: Medium Resolution Imaging Spectrometer (MERIS) (April 2002 to April 2012), Moderate Resolution Imaging Spectroradiometer (MODIS) (July 2002 to present), Sea-Viewing Wide Field-of-View Sensor (SeaWiFS) (September 1997 to December 2010), and Visible Infrared Imaging Radiometer Suite (VIIRS) (Jan 2012 to present). The approach used to combine satellite records must fully compensate for the differences between the individual datasets which can vary temporally and spatially (Djavidnia et al., 2010). If the differences between datasets are not accounted for, trends estimated from the combined record may be biased and/or have increased uncertainty (Gregg & Casey, 2010). Even with the use of multi-sensor records, the maximum available length of chl record is still only approximately 20 years, from the launch of SeaWiFS to present, shorter than the suggested ~30 years required to distinguish a climate change driven chl trend from natural variability (Henson et al., 2010; 2016).

To assess the effects of potential discontinuities in multi-sensor records on trend estimation, the discontinuities are modelled alongside the long-term trend as suggested in Weatherhead et al. (1998). More specifically, a Bayesian spatio-temporal model is used, which has been shown to provide an accurate fit to observations and a complete assessment of uncertainty when estimating chl trends (Hammond et al., 2017). Three major discontinuities in the satellite record are considered: the launch of both the MERIS and MODIS sensors in the spring/summer of 2002, the termination of the SeaWiFS sensor at the end of 2010, and the launch of the VIIRS satellite, providing data from the start of 2012.

5.3 Materials & Methods

5.3.1 Data

The chl data come from version 3.1 of the ESA OC-CCI project (Lavender et al., 2015; available at: http://www.esa-oceancolour-cci.org/). This product combines data from the SeaWiFS, MERIS, MODIS, and VIIRS sensors to create a continuous, bias-corrected time-series running from September 1997 to December 2016 inclusive. The ESA project uses band-shifting and bias-correction techniques to combine the data from individual sensors. This dataset is downscaled to a 1° grid by averaging within 1° boxes. As a comparison, the analysis is also performed on data from the GlobColour dataset (available at: http://globcolour.info/) in which SeaWiFS, MERIS, MODIS, and VIIRS sensors are merged using the Garver, Siegel, Maritorena Model process (Maritorena & Siegel, 2005; Maritorena et al., 2010), i.e. matching to a bio-optical model. Only Case 1 (open ocean) data are used as coastal regions are not considered (see below). A log-transformation is used on both sets of chl data, after Campbell (1995). To help explain natural variability in the chl data, SST is used as a covariate. SST data are sourced from the NOAA optimum interpolation v2 data product (Reynolds et al., 2002; available at: http://www.esrl.noaa.gov/psd/data/gridded/data.noaa.oisst.v2.html). Monthly means are used in all datasets.

Trends are analysed in 23 regions, based on those defined by Longhurst (1995; 1998) but with coastal and polar waters excluded due to issues with the availability and quality of data, see Table 2.2. Full details of the reasoning behind region selection are included in Section 2.1.

5.3.2 Model Formulation

A hierarchical Bayesian spatio-temporal model is fitted in each of the 23 Longhurst regions retained for analysis. The key equations are presented below; full details can be found in Section 2.2. First, the relationship between observed chl $Z_{n,t}$ and its true underlying value $O_{n,t}$ at location n and at month t is represented as:

$$Z_{n,t} = O_{n,t} + \varepsilon_{n,t} \tag{1}$$

where $\varepsilon_{n,t}$ is an independently normally distributed white noise process with zero mean and an unknown pure error variance, which primarily represents random measurement error. A regression model is used to represent the true chl value:

$$O_{n,t} = \boldsymbol{x}'_{n,t}\boldsymbol{\beta} + \boldsymbol{a}'_{n}\boldsymbol{w}_{m,t} \tag{2}$$

This regression model is composed of the covariates (including intercept) $\boldsymbol{x}_{n,t}$, the regression coefficients $\boldsymbol{\beta} = (\beta_0, \beta_{Trend}, \beta_{SST}, \beta_{Disc}, \beta_{M1}, \dots, \beta_{M12})$, and the term $\boldsymbol{a}'_{n}\boldsymbol{w}_{m,t}$ representing spatial and temporal correlation. The spatial correlation is represented by an exponential decay away from site n, and the temporal correlation by an AR(1) process. The covariates include the date of the observation, the month (which is represented as factor levels where each month of the year has an additional term, constant for all years), and SST. Time is used to estimate the temporal trend, the monthly factor is used to represent the seasonal cycle, and SST is used to isolate longer term environmental variability. The regression coefficients correspond to the covariates as follows: β_0 to the intercept, β_{Trend} to the trend, β_{SST} to SST, β_{Disc} to the discontinuity, and $\beta_{M1}, \dots, \beta_{M12}$ to the monthly factor levels. Note that the monthly factor is not included in the Pacific Subarctic Gyres Province (East) (Region 18), see Section 2.2 for the reasoning behind this decision.

Discontinuities are assumed to be represented by a mean-shift, i.e. an additional constant term is added after the time of discontinuity, a gradual drift in sensors (i.e. a discontinuity in trend) is not considered. The covariate indicating the presence of a mean-shift discontinuity is $\boldsymbol{x}^{Disc}$ and is represented as a factor which is different either side of the time of discontinuity (Weatherhead et al., 1998):

$$\boldsymbol{x}_t^{Disc} = \begin{cases} 0, & t < t_{Disc} \\ 1, & t \geq t_{Disc} \end{cases} \tag{3}$$

Where t_{Disc} is the known time of discontinuity. β_{Disc} is the regression coefficient for this mean-shift, representing the magnitude of the discontinuity. Vague priors, i.e. $N(0{,}100)$, are used for the discontinuity regression coefficients. Only the times of potential discontinuities are known and other factors such as the direction or magnitude of discontinuities are unknown, as there are few published estimates of inter-sensor discontinuities in the chl record. Trends are assumed to be of a constant value over the entire period under consideration, however the introduction of discontinuity terms is still expected to affect the estimation of trend magnitudes. An unaccounted mean-shift after a certain time point will introduce a temporal difference which the model will fit as a trend, in the case that no mean-shift term is included.

Five scenarios based on major satellite inclusions and failures are considered (Table 5.1). The first is a scenario with no discontinuities (N-scenario). The second scenario is one discontinuity at the launch of the MERIS and MODIS sensors in spring (April and July of 2002, respectively) (M-scenario). The time equidistant between their operational dates is used as the discontinuity time, due to the relatively short time between the launch of these satellites. The third scenario is a discontinuity at the failure of the SeaWiFS satellite in December 2010 (S-scenario). The fourth scenario is when both these discontinuities are considered in the same model (MS-scenario). The final scenario is when all discontinuities are considered, those above plus the launch of the VIIRS sensor in Jan 2012 (MSV-scenario). An additional scenario combining both the MERIS/MODIS discontinuity and the VIIRS discontinuity (MV-scenario) is considered in Appendix C.5.

The modelling approach fits a full posterior distribution for each parameter. This study focuses on the trend and discontinuity parameters with their posterior mode representing the best estimate. The uncertainty of the trend estimate is represented by the 95 % credible interval of the posterior, defined as the 95 % highest density interval (HDI) (Kruschke, 2015). The differences in the best estimate of the trend, and its uncertainty, are compared between the N-scenario and each discontinuity scenario in every region. When comparing the trends in each region, the discontinuity scenarios are considered likely to be statistically different if their 95 % credible intervals do not overlap.

The spTimer package in R is used to estimate the model fit (Bakar & Sahu, 2015). See Bakar & Sahu (2015) and Section 2.2 for additional details on the model setup.

5.4 Results

5.4.1 Discontinuity Magnitude and the Effect on Trend Estimates

In the majority of the regions in this study, taking into account discontinuities affects the trend estimate. The degree and direction of the effect is dependent on both the discontinuity scenario and region. The majority of regions have a discontinuity magnitude that is different from zero (i.e. their 95% credible intervals do not include 0 % yr $^{-1}$): 19 regions for the M-scenario and S-scenario, 17 regions for the MS-scenario, and 16 for the MSV-scenario. The majority of these regions also show a trend that is different from the N-scenario, i.e. their 95% credible intervals do not overlap. More specifically, in 17 regions in the S-scenario, 13 regions in the M-scenario, 13 regions in the MS-scenario, and 14 regions in the MSV-scenario the trend magnitudes are different when compared to the N-scenario.

The difference in trend estimates between the single discontinuity scenarios and the N-scenario is found to be inversely proportional to the discontinuity magnitude. A discontinuity magnitude of 0.1 log(mg m $^{-3}$) leads to a trend that is -0.65 % yr $^{-1}$ different (Figures 5.1b and 5.1c). The discontinuity for the M-scenario is positive in most regions, leading to a negative trend difference (average of -0.54 % yr $^{-1}$) (Figure 5.2). The opposite is found for the S-scenario (average of 0.59 % yr $^{-1}$). For the MS-scenario, the sign of the difference is evenly distributed between positive and negative (average difference -0.028 % yr $^{-1}$). In about half (12) of regions the trend difference for the MS-scenario lies between the trend differences for the two single discontinuity scenarios, suggesting they are partially cancelling out (Figure 5.1b). The MSV-scenario shows similar results to the MS-scenario with an average difference of 0.0047 % yr $^{-1}$ (Figures 5.1b & 5.3a) and can be compared to the N-scenario in Figure 5.4a.

The difference in trend magnitude for the MSV-scenario averages 1.1 % yr $^{-1}$, varying between -2.9 % yr $^{-1}$ and 2.6 % yr $^{-1}$. The MS-scenario is similar, averaging 0.85 % yr $^{-1}$ and varying between -2.2 % yr $^{-1}$ and 2.7 % yr $^{-1}$. The single discontinuity scenarios show a slightly lower trend magnitude difference: for the M-scenario the average difference in magnitude is 0.65 % yr $^{-1}$ (varying between -1.96 % yr $^{-1}$ and 1.0 % yr $^{-1}$) and for the S-scenario the average difference in magnitude is 0.81 % yr $^{-1}$ (varying between -0.95 % yr $^{-1}$ and 3.1 % yr $^{-1}$). Note that in a number of regions, the trend changes sign i.e. switches from increasing to decreasing or vice versa. These regions are, for the MSV-scenario, the North Atlantic Tropical Gyre Province (Region 4), the South Atlantic Gyral Province (Region 8), the Kuroshio Current Province (Region 12), the North Atlantic Subtropical Gyral Province (West) (Region 15), and the Subantarctic Province (Region 22). There is no clear global pattern in either the trend difference or the discontinuity magnitude.

To fully understand how discontinuities affect the estimated trends, an alternative multi-sensor dataset is considered: GlobColour. The differences for each of the discontinuity scenarios compared to the N-scenario are shown in Figure 5.5. The uncertainty and trend differences are found to be very similar on average to the ESA OC-CCI dataset. The average trend differences for the GlobColour dataset are: -0.35 % yr^{-1} (M-scenario), 0.72 % yr^{-1} (S-scenario), -0.057 % yr^{-1} (MS-scenario), and -0.32 % yr^{-1} (MSV-scenario). They are -0.54 % yr^{-1} (M-scenario), 0.59 % yr^{-1} (S-scenario), -0.028 % yr^{-1} (MS-scenario), and 0.047 % yr^{-1} (MSV-scenario) for the average trend difference in the ESA OC-CCI dataset. Both datasets show a similar pattern for trend differences with the M-scenario being negative, and the S-scenario being positive. Discontinuity magnitudes also show the same pattern as the trend difference but reversed. However, the GlobColour dataset has slightly higher magnitude trend differences in the scenarios with multiple discontinuities, possibly arising from the different merging approach used. The regional pattern is somewhat different to the OC-CCI dataset although there remains no clear pattern. In summary the use of a different multi-sensor dataset, which uses a different merging approach, does not affect the results.

5.4.2 Effect of Discontinuities on Trend Estimate Uncertainties

Taking into account discontinuities increases uncertainty in all scenarios and regions. A single discontinuity increases trend uncertainty by an average of 0.21 % yr^{-1}; for the S-scenario it is 0.24 % yr^{-1}, and the M-scenario it is 0.17 % yr^{-1}. The magnitude of uncertainty increase is region dependent and varies in the range 0.016 - 0.64 % yr^{-1} (Figure 5.1a). For the MS-scenario the average difference in uncertainty is 0.64 % yr^{-1}, varying for individual regions in the range 0.071 – 1.5 % yr^{-1} (Figure 5.1a). The MSV-scenario the uncertainty difference is similar to the MS-scenario, with an average of 0.64 % yr^{-1}, varying in the range of 0.077 – 1.6 % yr^{-1} (Figures 5.1a & 5.3b) and it can be compared to the N-scenario in Figure 5.4b).

The regions with the highest proportional increase in uncertainty, for the MSV-scenario relative to the N-scenario, are the Pacific Equatorial Divergence Province (Region 7) (0.25 % yr^{-1}, 200 %), the Indian Monsoon Gyres Province (Region 2) (uncertainty increase of 0.66 % yr^{-1}, 200 % compared to N-scenario), the North Atlantic Tropical Gyral Province (Region 4) (0.60 % yr^{-1}, 200 %), the Western Tropical Atlantic Province (Region 10) (0.63 % yr^{-1}, 210 %), and the North Atlantic Subtropical Gyral Province (West) (Region 15) (0.77 % yr^{-1}, 220 %). Regions with the smallest proportional uncertainty increase are typically found in the mid-latitude Pacific Ocean: the North Pacific Tropical Gyre Province (Region 6) (0.51 % yr^{-1}, 140 %), the West Pacific Warm Pool Province (Region 9) (0.57 % yr^{-1}, 140 %), the Kuroshio Current Province (Region 12) (1.6 % yr^{-1}, 150 %), the North Pacific Polar Front Province (Region 16) (0.24 % yr^{-1}, 140 %), and the South Pacific Subtropical Gyre Province (Region 20) (0.40 % yr^{-1}, 140 %).

The average uncertainty differences for the GlobColour dataset are: 0.24 % yr^{-1} (M-scenario), 0.32 % yr^{-1} (S-scenario), 0.75 % yr^{-1} (MS-scenario), and 0.81 % yr^{-1} (MSV-scenario) (Figure 5.5 shows a regional breakdown of this). For the ESA OC-CCI dataset the average uncertainty differences are: 0.17 % yr^{-1} (M-scenario), 0.24 % yr^{-1} (S-scenario), 0.62 % yr^{-1} (MS-scenario), and 0.81 % yr^{-1} (MSV-scenario). Both datasets show a very similar pattern for average uncertainty difference. However, uncertainty differences are typically larger in the GlobColour dataset, by an average across all scenarios and regions of 0.12 % yr^{-1}. In summary the use of a different multi-sensor dataset, using a different merging approach, does not affect the findings of this study.

5.5 Discussion

5.5.1 How do Discontinuities Affect Trend Magnitude Estimates?

The trend difference between the MSV-scenario and the N-scenario averages 1.1 % yr^{-1}, varying in the range ± 2.8 % yr^{-1}, resulting in different trends in 14 of the 23 regions. In a study that analysed the effect of bias between sensors by introducing artificial biases in the range 1 - 50 % when merging the SeaWiFS and MODIS sensors, Mélin (2016) showed that a 5 - 6 % bias between two sensors can lead to significantly different trends. This illustrates the strong effect that discontinuities in the record can have, in agreement with the present study. However, Mélin (2016) also found that trends estimated for oligotrophic subtropical gyres are particularly sensitive to discontinuities in the record, which they attributed to the low natural variability of gyres and thus more easily detected trends. In the present study, oligotrophic gyres do not seem to show such a pattern, although the Pacific oligotrophic subtropical gyre regions do show a greater than average difference in trend. The average trend magnitude difference is 1.1 % yr^{-1}; the North Pacific Tropical Gyre Province (Region 6) has a difference of 2.2 % yr^{-1}, North Pacific Subtropical Gyre Province (West) (Region 17) has a difference of -2.9 % yr^{-1}, and the South Pacific Subtropical Gyre Province (Region 20) has a difference of -1.3 % yr^{-1}. The difference to Mélin (2016) may be due to the substantial differences in methodologies. Here a spatio-temporal method is used on a dataset merged from multiple sensors to take into account discontinuities, whereas Mélin (2016) analysed records with discontinuities induced prior to merging.

Work by Brewin et al. (2014) suggests that trends in monthly log-transformed chl values, calculated using least squares linear regression, show a similar regional pattern in the MERIS, MODIS, and SeaWiFS sensors. However, the results of the present study imply that trends may not show a similar pattern in multi-sensor records when discontinuities are taken into account with a spatial correlation technique. Taking into account discontinuities leads to substantially different trends, implying that in these cases there may be disagreement between the individual sensors making up the multi-sensor record, and this is made clearer by considering spatial correlation.

The discontinuity model in the present study represents a mean-shift. Another significant problem with multi-sensor datasets, and sensors in general, is the gradual drift in sensors' detected values, i.e. a discontinuity which is associated with a change in trend. Drift is not directly assessed here. A gradual drift makes merging individual sensors more challenging and, if not corrected, may also directly affect estimated trends. Mélin (2016) determined that any drift greater than 2 % per decade can alter the conclusions of a trend analysis, which suggests this effect may be as important as discontinuities in the mean. Drift is not assessed here, as over the short-term period of drift (several years) its magnitude is likely to be confused with any interannual variability that is not accounted for by the SST term. To correctly account for inter-sensor drift, a comparison of the individual sensor records and available in situ records would be required, which is beyond the scope of this study. Inter-sensor drift would be expected to lead to further increases in uncertainty and changes to the trend estimates.

A final potential problem with multi-sensor datasets is discontinuities in variance which could occur due to differences between sensors. Such differences may include: different sensor noise levels, different sensor sensitivity to chl values, or different sensor sensitivity to chl seasonality. Variance-shift discontinuities were not considered here as substantial modification to the model framework would be required for this analysis to be performed. Such changes would be expected to affect estimation of the trend by introducing more uncertainty in fitting the trend term. This work could be expanded in future to consider shifts in variance.

The results here depend on the ability to distinguish trends and discontinuities accurately. A series of simulation studies with “known” trends and discontinuities are conducted to assess model skill in accurately estimating trends and discontinuities. 100 synthetic datasets are generated, which should prove to be a sufficient number to account for the effects of random variability. The synthetic datasets are based on the North Atlantic, with equivalent record length, mean chl, and sinusoidal seasonality. The synthetic datasets assume a Gaussian spatio-temporal random field based on variograms calculated from the real North Atlantic data. This process is the same that is assumed by the statistical model used in all chapters. A realistic range of trends and discontinuities (at the time of the SeaWiFS discontinuity) is then applied to the datasets. The space-time model is used to estimate the trend and discontinuity magnitudes in these synthetic datasets, the results of which can be found in Tables 5.2 & 5.3. In these simulation studies the trend term is accurately estimated to within less than 1 %, and the discontinuity term is accurately estimated to within approximately 5 %, for a specified discontinuity of 0.01 mg m^{-3} or greater. The statistical model shows skill in accurately estimating specified trends and discontinuities in a realistic synthetic dataset, thus the risk of obtaining erroneous estimates in the real datasets with this approach should be low.

5.5.2 How do Discontinuities Affect Uncertainty in Trend Estimates?

The results show that taking into account potential discontinuities in the record increases the uncertainty of long-term trends, such that two discontinuities can double the uncertainty in trend estimates. Detection of trends in the current multi-sensor record may be particularly sensitive to a) the timing of discontinuities relative to decadal variability and b) the location of discontinuities in the record. The 1997/1998 El Niño event (Wolter & Timlin, 1998) lies before the MERIS/MODIS discontinuity, and the 2015/2016 El Niño event (Levine & McPhaden, 2016) follows the SeaWiFS and VIIRS discontinuities (Figure 5.6). The larger uncertainty, and trend magnitude, differences seen in the S-scenario appear to be caused by the SeaWiFS discontinuity being further from either end of the record than the MERIS/MODIS discontinuity, leading to a higher impact on the trend estimates. The MSV-scenario may have comparable results to the MS-scenario as the VIIRS and SeaWiFS discontinuities are only separated by 1 year. The increase in trend uncertainty when taking into account discontinuities is likely to make trend analysis using longer multi-sensor records more challenging, as there will be a larger number of sensors and thus potentially a larger number of discontinuities. However, the timing of these discontinuities is important; if two discontinuities are temporally close the effect may be similar to only one discontinuity.

The increase in trend estimate uncertainty when taking into account discontinuities occurs because the statistical model is estimating the magnitude of specific discontinuities. This leads to a greater degree of freedom as the model has extra terms to fit. These discontinuities still exist even if not specified in the model. Studies neglecting to consider these terms will have a perceived, but inaccurate, smaller uncertainty. This larger uncertainty challenges the detection of long-term trends by increasing the length of record required.

5.5.3 Implications for Multi-sensor Ocean Colour Records

Very similar results are found when using both the ESA OC-CCI dataset and GlobColour dataset. This is despite the two datasets being merged using different approaches. The ESA OC-CCI dataset has been corrected for bias (Lavender et al., 2015). The GlobColour data are specifically not bias corrected so as not to unduly introduce a false trend, but are instead validated by comparison to a biogeochemical model (Ford & Barciela 2017; Maritorena et al., 2010). This suggests that the results, in the present study, are largely independent of the particular dataset used. Instead the method assesses the effect a discontinuity would have at certain specified times. Any true biases within the dataset may have already been partially, or completely, corrected during the merging process. This means that the true trend and uncertainty likely lie in a range between the results from the N-scenario (the lower limit) and the MSV-scenario (the upper limit).

5.6 Conclusion

The effect of taking into account discontinuities in multi-sensor satellite records on the magnitude and uncertainty of chl trends is assessed using a Bayesian spatio-temporal method. This method provides a quantification of the trend uncertainty, as well as an accurate assessment of trends within the data. Discontinuities are introduced into the statistical model as a discrete factor, at the times dictated by three major discontinuities in the ocean colour record. These are the introduction of the MERIS and MODIS sensors in 2002, the loss of the SeaWiFS sensor at the end of 2010, and the introduction of the VIIRS sensor in 2012.

The effect on uncertainty is dependent on the number of discontinuities present. If just one of the above discontinuities is modelled, there is a ~0.20 % yr^{-1} increase in uncertainty. If two discontinuities are modelled, i.e. MERIS/MODIS & SeaWiFS or MERIS/MODIS & VIIRS, the uncertainty rises by at least 0.064 % yr^{-1} and by up to 1.5 % yr^{-1}, dependent on the region. Modelling all three discontinuities produces similar results to modelling the two discontinuities as listed above. The increases in trend uncertainty are accompanied by a difference in trend estimates. When modelling all three discontinuities, the differences in trend magnitude have a maximum of 2.9 % yr^{-1}, are statistically likely to be different in 14 of the 23 regions considered, and can even show a different sign of trend.

The increase in uncertainty and bias in trend estimates when taking into account discontinuities challenges the detection of long-term trends in multi-sensor records. The discontinuity-induced differences in trend estimates shown here should be considered as an upper limit, i.e. the maximum difference that discontinuities at this time point may produce. This work does not directly assess the efforts made to combine these datasets, meaning the effect revealed in the dataset may already be minimised. The trend bias and increase in uncertainty induced by taking into account discontinuities in the record stresses the importance of using the best techniques to remove biases between sensors when combining them. Such techniques may include advanced statistical methods, potentially including the use of spatio-temporal models, as well as launching missions with sufficient overlap in order to most effectively cross-calibrate and merge records.

5.7 Tables

Table 5.1 Information on the different discontinuity scenarios considered. The time of discontinuities stated represent the final month before the discontinuity, as the discontinuity is represented as being between months. Trends are considered to be statistically different to the N-scenario if their 95 % credible intervals do not overlap. Values in brackets represent the percentage of regions (out of 23) which show a statistically different trend. See also Figure 5.6 where the lifespans of individual sensors are plotted as a time-series.

Abbreviation	Discontinuities	Time of Discontinuities	Number of Regions with Statistically Different Trends
N	n/a	n/a	n/a
M	MERIS/MODIS	May 2002	13 (57 %)
S	SeaWIFS	December 2010	17 (74 %)
MS	MERIS/MODIS and SeaWiFS	May 2002 and December 2010	13 (57 %)
MV	MERIS/MODIS and VIIRS	December 2010, and December 2011	13 (57 %)
MSV	MERIS/MODIS, SeaWiFS, and VIIRS	May 2002, December 2010, and December 2011	14 (61 %)

Table 5.2 Mean model trend estimates when using the 100 synthetic datasets based on real North Atlantic data with specified trends and discontinuity (at the time of the SeaWiFS discontinuity). The statistical model is able to estimate the specified trends well.

	Discontinuity in Data (mg m^{-3})				
	0	0.001	0.01	0.1	1
Trend in Data (% yr^{-1})	Trend Estimate (% yr^{-1})				
-4.0	-4.0	-4.0	-4.0	-4.0	-4.0
-2.0	-2.0	-2.0	-2.0	-2.0	-2.0
-1.0	-1.0	-1.0	-1.0	-1.0	-0.99
0.0	2.9×10^{-4}	-4.4×10^{-4}	-1.7×10^{-3}	-6.6×10^{-4}	-4.2×10^{-3}
1.0	1.0	1.0	1.0	1.0	1.0
2.0	2.0	2.0	2.0	2.0	2.0
4.0	4.0	4.0	4.0	4.0	4.0

Table 5.3 Mean model discontinuity estimates when using the 100 synthetic datasets based on real North Atlantic data with specified trends and discontinuity (at the time of the SeaWiFS discontinuity). The statistical model is able to estimate the specified discontinuities well.

	Discontinuity in Data (mg m^{-3})				
	0	1.0×10^{-3}	1.0×10^{-2}	0.10	1.0
Trend in Data (% yr^{-1})	Discontinuity Estimate (mg m^{-3})				
-4	3.1×10^{-4}	1.5×10^{-3}	1.1×10^{-2}	0.10	1.0
-2	3.0×10^{-4}	7.0×10^{-4}	9.6×10^{-3}	0.10	1.0
-1	-8.5×10^{-5}	8.8×10^{-4}	1.0×10^{-2}	0.10	1.0
0	-8.4×10^{-5}	1.1×10^{-3}	1.0×10^{-2}	0.10	1.0
1	-4.3×10^{-4}	6.9×10^{-4}	9.8×10^{-3}	0.10	1.0
2	3.5×10^{-4}	9.1×10^{-4}	9.6×10^{-3}	0.10	1.0
4	4.0×10^{-4}	1.1×10^{-3}	1.1×10^{-2}	0.099	1.0

5.8 Figures

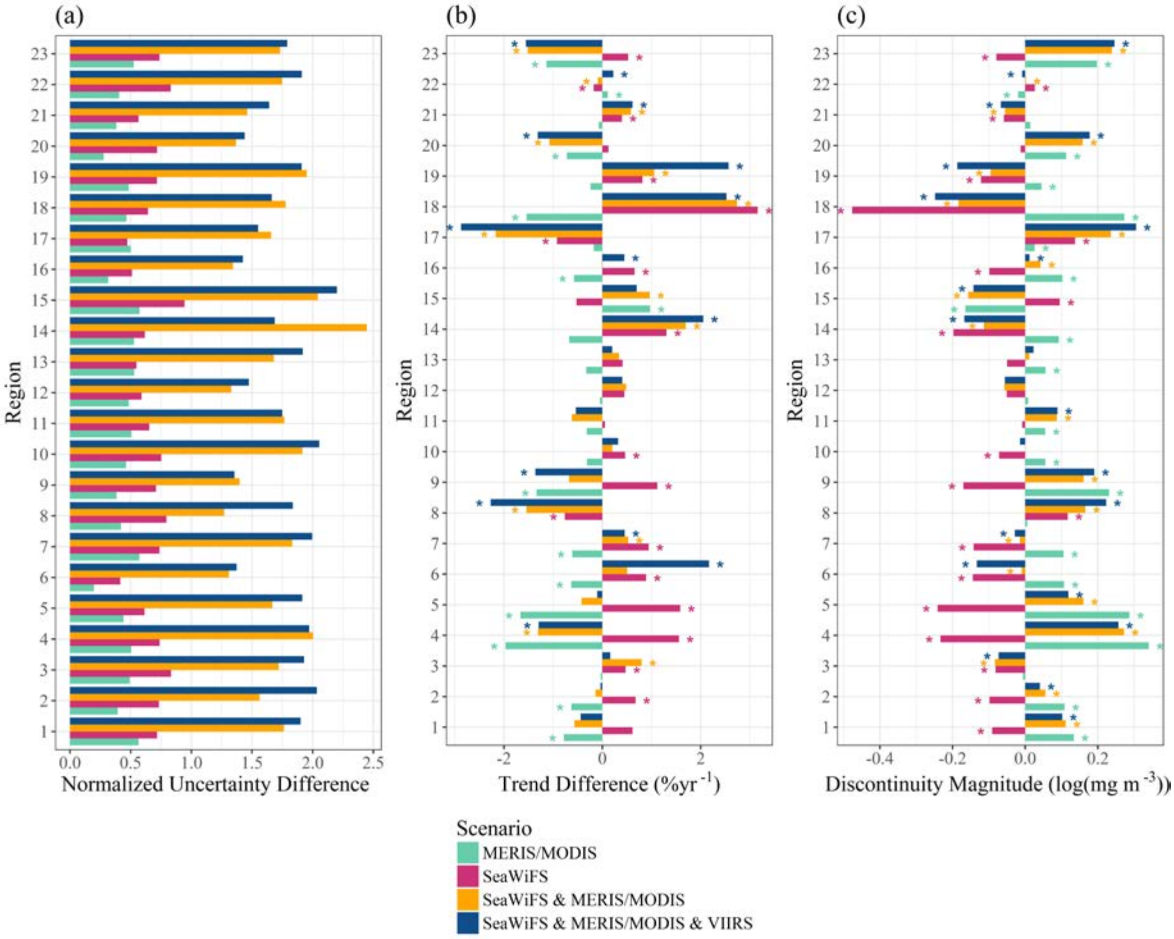

Figure 5.1 The difference in (a) uncertainty (normalised to each region's uncertainty), (b) trend between the models with a discontinuity term and the no discontinuity scenario, and (c) the discontinuity magnitude for each region (averaged for the multiple discontinuity scenarios). These results are from the ESA OC-CCI dataset. See Table 5.1 for the scenario abbreviations used in the main text. The uncertainty is defined as the width of the 95 % credible intervals. For (b), regions where trends are statistically different from zero, i.e. their 95 % credible intervals do not contain zero, are indicated with *. For (c), * indicates that at least one discontinuity is different from zero. Inclusion of the SeaWiFS discontinuity tends to lead to a more positive trend, whilst the MODIS/MERIS discontinuity leads to a more negative trend in most cases, associated with a negative and a positive discontinuity magnitude respectively. See Figure 5.3 for a map of the regions. Region names are listed in Table 2.2.

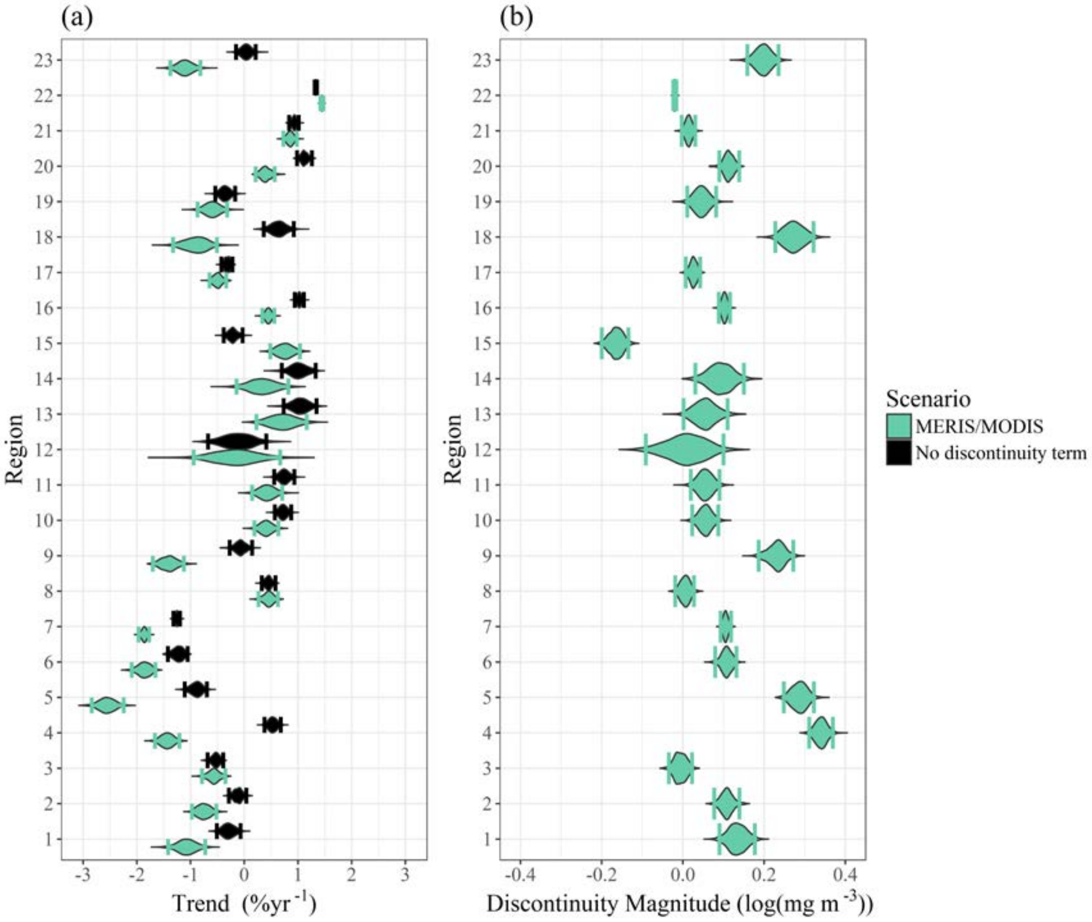

Figure 5.2 Posterior probability density of (a) the trend in the MERIS/MODIS discontinuity scenario and the no discontinuity scenario, and (b) the discontinuity magnitude in the MERIS/MODIS discontinuity scenario, for each region. These results are from the ESA OC-CCI dataset. Trends, estimated for the two scenarios, are considered to be statistically different if their 95 % credible intervals do not overlap. Corresponding figures for the other scenarios can be found in the Appendices C.3 - C.6. Regions names are listed in Table 2.2.

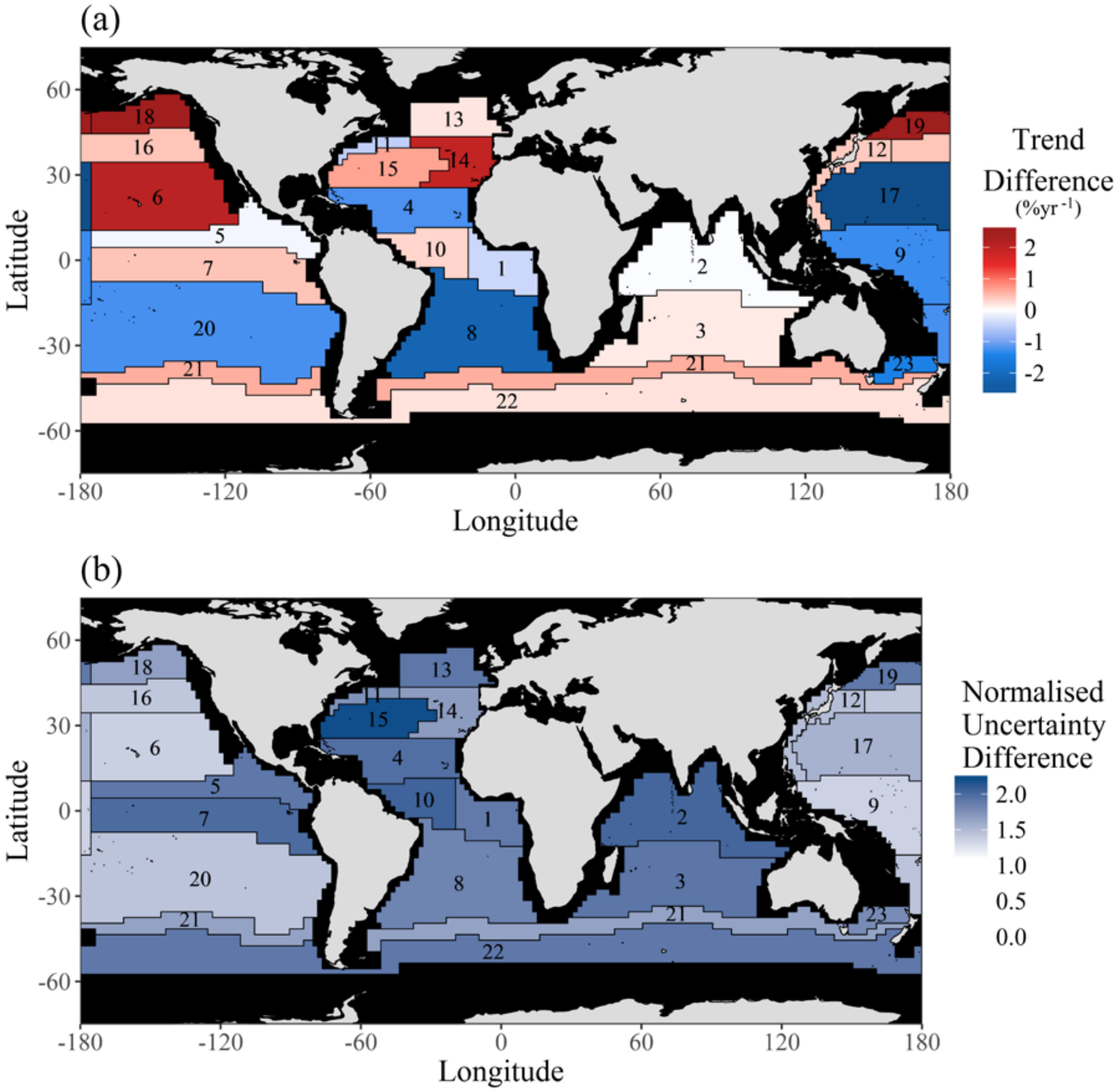

Figure 5.3 The difference for individual regions in their (a) estimated trend and (b) estimated uncertainty (normalised to each region’s uncertainty), comparing the scenario with all discontinuities and the scenario with no discontinuities. These results are from the ESA OC-CCI dataset. Region names are listed in Table 2.2. See Figure 5.4 for the trend magnitude as estimated in the scenario with no discontinuity.

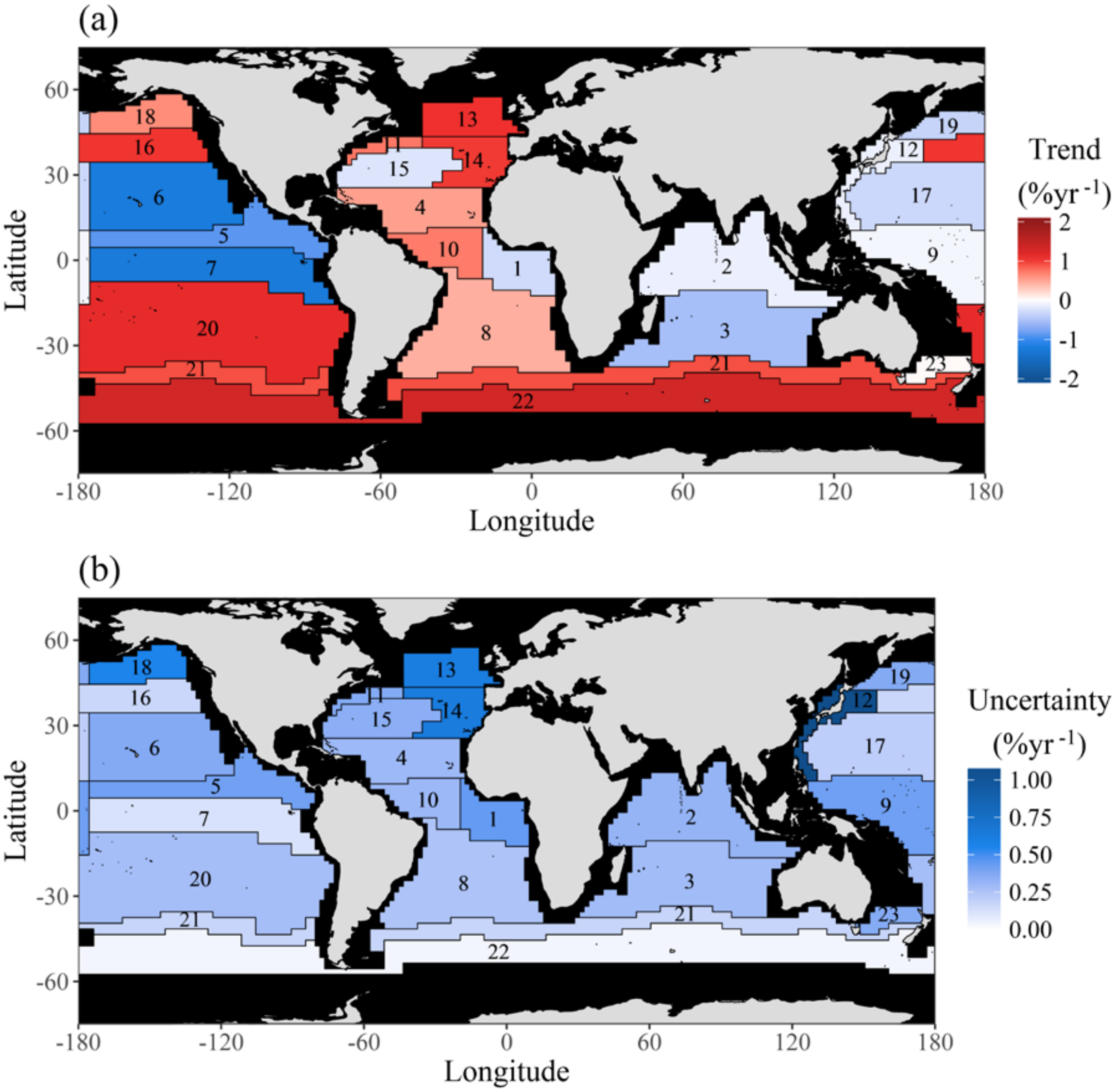

Figure 5.4 The (a) trend magnitude and (b) uncertainty of the trend estimate for individual regions under the scenario with no discontinuity. These results are from the ESA OC-CCI dataset. This is the scenario which all other scenarios are compared to.

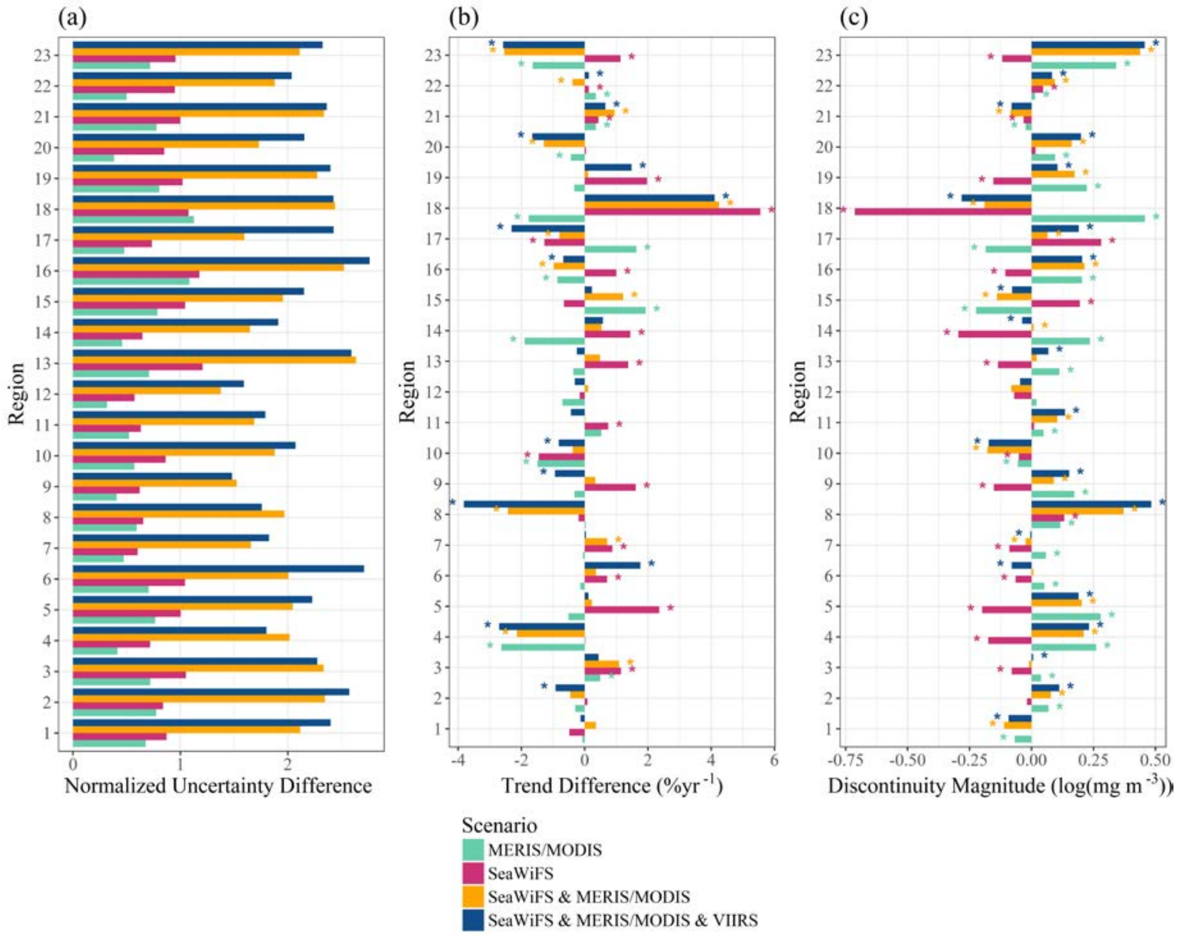

Figure 5.5 The difference in (a) uncertainty (normalised to each region's uncertainty) and (b) trend between the models with a discontinuity term and the no discontinuity scenario, as well as (c) the discontinuity magnitude for each region (averaged for the multiple discontinuity scenarios). All information from this figure results from the model using GlobColour data. The uncertainty difference is the difference between the widths of the 95 % credible intervals. For (b), regions where trends are statistically different from zero, i.e. their 95 % credible intervals do not contain zero, are indicated with *. For (c), * indicates that at least one discontinuity is different from zero. There is a ~0.28 % yr^{-1} difference when a single discontinuity is considered and an average of 0.72 % yr^{-1} when considering two discontinuities. The difference in trend is between the modes of the posterior trends. Region names can be found in Table 2.2.

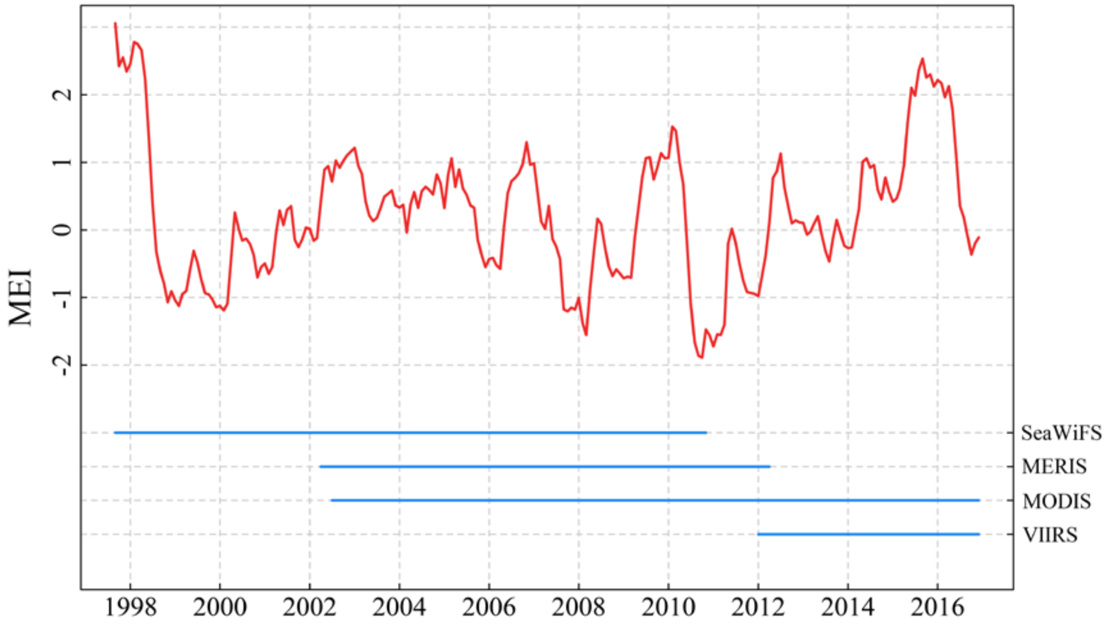

Figure 5.6 The multivariate ENSO index (MEI) indicating the relative strengths of El Niño and La Niña events. Also shown are the lifespans of the sensors used in the ESA OC-CCI and GlobColour datasets: SeaWiFS, MERIS, MODIS, and VIIRS. The strong El Niño event in 1997/1998 precedes the MERIS/MODIS discontinuity and the similarly strong event in 2015/2016 follows the VIIRS and SeaWiFS discontinuities.

Chapter 6: Synthesis

6.1 Conclusions from This Work

Chl is of global importance and any changes could potentially have a large impact on ocean ecosystems and the environment, both of which could impact humanity. The aim of this work was to improve the estimation of global chl trends, an area of research that despite its importance is without clear consensus in the literature. The main conclusions from this work are as follows.

In Chapter 3, a hierarchical Bayesian spatio-temporal model is used to estimate chl trends in global ocean colour data for the period September 1997 - December 2013. To assess the impact on chl trends from including spatial correlation terms, a model without spatial correlation is also fitted. Including spatial correlation terms results in a notable improvement in accuracy of model fit. Additionally, including spatial correlation terms results in an order of magnitude smaller global trend, and larger uncertainty: - 0.023 ± 0.12 % yr^{-1} as opposed to - 0.38 ± 0.045 % yr^{-1} when the spatial correlation terms are not included. The clear improvement in model fit accuracy, and assessment of uncertainty, emphasises the potential of using spatio-temporal modelling when studying global change in chl, although additional work is required to determine if these estimated trends are indeed long-term, to allow comparison with studies using long-term in situ data. The difference in uncertainty between the two models is a result of the different volumes of information considered. In the model without spatial correlation terms, individual grid cells are considered as independent, i.e. their spatial relationship is ignored, this leads to an artificially small uncertainty in these trend estimates. The large degree of noise associated with ocean colour data, alongside the large natural variability, relative to low magnitude trends, may make spatio-temporal models particularly useful for estimating trends in chl data, future studies should build upon this work by using additional data sources to further improve our understanding.

Coupled physical-biogeochemical models provide representations of the ocean that can cover many decades. In Chapter 4, this information is used with the aim of enhancing the separation of long-term trends from decadal variability and reducing trend estimate uncertainty. Trends are estimated in CMIP5 models over the period 1979 - 2033 to incorporate as priors into the Bayesian spatio-temporal model. The introduction of priors reduces the uncertainty of trend estimates

(0.027 % yr^{-1} average) and the magnitude of trends (0.060 % yr^{-1} average). The trend estimates using CMIP5 priors tend to be lower magnitude than the trends estimated without priors, which are mainly positive, leading to an average reduction in trend magnitude. However, the trends are not deemed to be statistically different with and without the CMIP5 priors, in any region. In the majority (16 of 23) of regions, the trend estimates using solely the observational chl data are different from the CMIP5 priors, indicating disagreement between trends detected in satellite observations and model output. The impact of the priors is limited due to this disagreement. Additionally, a sensitivity analysis indicates that reduced variability in CMIP5 prior trends would provide more impactful priors. Longer-term observations and better biological and physical model representations may help reconcile these differences in future. These would also help determine if long-term trends in ocean colour data have yet to become distinguishable from natural variability and whether coupled physical-biogeochemical models are currently capable of accurately representing chl trends in the ocean.

Multi-sensor records are typically used in the analysis of trends in ocean colour data, due to the short lifespans of individual sensors. Creating a multi-sensor record from the individual sensors requires data treatment to resolve any inter-sensor differences. The data treatment process may fail to correct the biases, or potentially introduce additional biases between sensors, which may affect estimated trends and their uncertainties. In Chapter 5, the Bayesian spatio-temporal model is used to analyse the effect of taking into account discontinuities on estimated chl trends. The discontinuities considered are the introduction of the MERIS, MODIS, and VIIRS sensors, and the termination of the SeaWiFS sensor. The majority (between 16 and 19 depending on scenario) of regions are found to have a at least one discontinuity with a magnitude that is statistically different from zero. In the scenario considering all discontinuities there are statistically different trends in ~60 % of regions, with an average change in magnitude of 1.1 % yr^{-1} and a reversal of trend sign in ~13 % of regions. Considering a single discontinuity also leads to an increase in uncertainty, averaging 0.20 % yr^{-1} for a single discontinuity and 0.59 % yr^{-1} for two discontinuities. One key consideration of these results is that any biases within the dataset may have already been partially, or completely, corrected during the merging process. This means that the true trend and uncertainty likely lie in a range between the results of taking all discontinuities in to account and taking no discontinuities into account (especially if discontinuities are well corrected for in the merging process). This difference in trend magnitude and uncertainty highlights the importance of minimizing discontinuities in multi-sensor records and stresses the importance of considering discontinuities when analysing trends.

If these discontinuities are considered to be effectively corrected for within the ESA OC-CCI v3.1 dataset, then the general outlook for global chl seems to be mixed with positive trends at high latitudes and more negative trends elsewhere. There should be some caution in this assumption, as although the ESA OC-CCI dataset shows very similar trends to those of its component single mission products until 2012, the data beyond this may be affected by MODIS ageing. Although over the period 2012 - 2015 the ESA OC-CCI v3.1 data show similar trends to the VIIRS sensor (Mélin et al., 2017). This general picture, of more positive trends at high latitude, is unchanged between the ESA OC-CCI v2.0 and v3.1 datasets. The differences between the ESA OC-CCI v2.0 and v3.1 dataset are three additional years of ocean colour data, from the MODIS sensor, the introduction of the VIIRS sensor to provide additional data from 2012, and updated algorithms to provide corrections for decay in MODIS data (Grant et al., 2017). Trends are however generally more positive, in the v3.1 dataset, and in 4 regions the trends change sign from negative to positive. Specifically, the global weighted average trend is -0.023 % yr^{-1} in the v2.0 dataset and 0.29 % yr^{-1} in the v3.1 dataset (with CMIP5 priors, although their inclusion has limited impact). The regional pattern is also largely the same with positive trends in high to mid latitudes and negative or neutral (i.e. the trend is not statistically different from zero) trends elsewhere. However, some regions do change sign. The following regions have positive trends in both datasets but show an increase in the magnitude of trends (listed in brackets): the North Atlantic Subtropical Gyral Province (East) (Region 14) (0.97 % yr^{-1} in v2.0 and 0.99 % yr^{-1} in v3.1), the North Atlantic Drift Province (Region 13) (0.64 % yr^{-1} in v2.0 and 1.0 % yr^{-1} in v3.1), the Gulf Stream Province (Region 11) (0.16 % yr^{-1} in v2.0 and 0.74 % yr^{-1} in v3.1), the Pacific Subarctic Gyres Province (East) (Region 18) (0.34 % yr^{-1} in v2.0 and 0.67 % yr^{-1} in v3.1), the North Pacific Polar Front Province (Region 16) (0.36 % yr^{-1} in v2.0 and 1.0 % yr^{-1} in v3.1), and the Subantarctic Province (Region 22) (0.18 % yr^{-1} in v2.0 and 1.3 % yr^{-1} in v3.1). All these regions are, at least partially, at latitudes greater than 30°; this implies that outside the tropical ocean the trend is typically more distinguishable from natural variability. However, subtropical gyre regions are expected to have different controls to higher latitude regions, so it is unclear why they should be included in this pattern (e.g. Doney, 2006; Signorini et al., 2015). Work needs to be done to understand the meaning of the difference in model trend estimates between when considering spatial correlation, and when not (see Section 6.4). This should help explain the latitudinal pattern.

Although generally the regional pattern is consistent between these two datasets, there are some regions that do show substantial changes, indicating that these regions may require longer datasets before trends can be detected. The regions showing the highest difference between datasets are in the Northern Pacific, indicating this may be a result of larger natural variability in some regions. The North Pacific Equatorial Countercurrent Province (Region 5) and the North Pacific Tropical Gyre Province (Region 6) both change the sign of their trend and are located primarily in the eastern equatorial to subtropical North Pacific. The North Pacific Subtropical Gyre Province (West) (Region 17) has the opposite change in trend and is located in the western subtropical Pacific. The equatorial to subtropical Pacific location is expected to be strongly influenced by ENSO (e.g. Racault et al., 2017). The ENSO index is quite different between the two ESA OC-CCI datasets, both start with a strong El Niño event in 1997/1998 (Wolter & Timlin, 1998), but the v3.1 dataset also includes a second similarly strong event in 2015/2016 (e.g. Levine & McPhaden, 2016). El Niño events have been shown to be associated with a decrease in eastern equatorial/subtropical Pacific chl of up to 15 %, with the opposite relationship occurring in western equatorial/subtropical Pacific (Behrenfeld et al., 2006; Racault et al 2017). The ESA OC-CCI v2.0 dataset estimates positive trends in the North Pacific Equatorial Countercurrent Province (Region 5) and the North Pacific Tropical Gyre Province (Region 6), which could be explained by the strong negative anomaly caused by the 1997/1998 El Niño event. The ESA OC-CCI v3.1 dataset has the opposite trend which may imply that after accounting for both strong El Niño events the trend is negative in these regions. Additional covariates to explain environmental variability may help distinguish a secular trend from such strong variability.

The effect of potential discontinuities must not be discounted, substantial increases in uncertainty and different trend estimates are expected if these discontinuities have not been completely corrected for. Efforts to take discontinuities into account, like presented here, should be performed if there is any doubt about the inter-sensor consistency in multi-sensor records. Continued work improving multi-sensor records is of crucial importance to enable accurate long-term trend estimation, and to reduce the necessity of taking discontinuities into account in future.

6.2 Wider Implications

The general outlook for chl is a positive trend at mid to high latitudes and a negative trend elsewhere; this is expected to have impacts on wider ecosystems and biogeochemical cycling. Specifically changes in phytoplankton, as the base trophic level, are expected to lead to concurrent changes in zooplankton and fish stocks with increases at high latitude and decreases at low latitude. Even the relatively small changes in phytoplankton seen here, in the range of 2 % yr^{-1} may have larger impacts on higher trophic levels through the effect of trophic amplification (e.g. Cheung et al., 2010). Changes in phytoplankton will likely combine with other climate change impacts on fish physiology. Such physiological impacts may include changes in growth rates and oxygen availability resulting from temperature increases (e.g. Cheung et al 2013).

Similar latitudinal patterns to that reported in the present study have already been reported in the range shifts of fish, responding to changes in phytoplankton abundance, phytoplankton distribution, physiology, and fishing pressure (e.g. Cheung et al., 2013; Pinsky & Fogarty, 2012). Changes in phytoplankton will have a strong human impact, as they are the controlling factor in the most productive, overfished regions (Mcowen et al., 2015). The reported latitudinal pattern is of particular importance as low-latitude fisheries already have a lower yield than higher latitude ones (Friedland et al., 2012). In terms of a resulting human impact, it must be noted that only open ocean regions are assessed, these account for 20 % of total fisheries biomass (Sherman et al., 2009). However, warming oceans are expected to lead to onshore species moving further offshore (Dulvy et al., 2008), and thus the key areas of fishing may follow, increasing the proportion of fisheries biomass in open ocean regions. To improve the assessment of phytoplankton abundance changes on humanity, expansion of this technique to coastal regions should be considered, although efforts must be made to resolve data quality issues in ocean colour there.

The latitudinal pattern in chl trends will also have effects on the environment, with the potential to feedback on climate, via changes in biogeochemical systems. Changes may occur in oceanic fluxes of CO_2, N_2O, and dimethyl sulphide (DMS) as a response to these trends in phytoplankton (Law et al., 2008; Levasseur et al., 2013; López-Urrutia et al., 2006). DMS in the lower atmosphere acts as cloud condensation nuclei which can increase the albedo of low latitude clouds (Charlson et al., 1987; Levasseur et al., 2013). Although production of DMS is species dependent (Keller et al., 1989), decreases in chl are suggested to lead to decreases in DMS fluxes (Bopp et al., 2003). One of the best studied potential impacts of phytoplankton productivity changes is on the carbon system, due to the importance of global atmospheric CO_2. Modelled productivity increases, particularly in the high latitude north hemisphere, have been associated with increases in carbon export (Laufkötter et al., 2013). A net global increase in chl would be expected to result in an increased export of biogenic carbon to the deep ocean, a negative feedback on climate. The magnitude of this may be impacted by the more potent greenhouse gas N_2O; increased atmospheric fluxes of N_2O are expected to be most dramatic under decreasing O_2 conditions in tropical regions (Jin & Gruber, 2003), however the decreasing trends in chl shown in tropical regions in the present study may reduce this effect. There are many routes for a positive trend in phytoplankton to provide a negative feedback on climate, although the exact magnitudes are subject to a global balance between gases and other factors including species composition.

There are several possibilities for reducing trend estimate uncertainty in future, which is crucial to improving the decision-making process. The simplest approach to reducing uncertainty may be to use longer data records. Longer records would likely make the trend more distinguishable from other components of the signal, provided there are no concurrent increases in variability, which would act to conceal this. Ocean colour trend estimates may be further improved by using more advanced techniques to remove sources of noise from the data, these include cloud, sun glint, atmospheric interference (e.g. aerosols and dust), and other water column constituents. Methods to reduce these noise components could include the use of in situ data sources or improvements in the data treatment used to produce ocean colour records. This would allow more of the true signal to be assessed. The statistical model does already allow for estimation of normally distributed random noise, however many of these interferences are biased in one direction, for example CDOM can be confused for chl and its presence can make chl appear higher (e.g. Lewis et al., 2016). These constituents are also expected to vary over time, affecting trend estimates for example regionally in cloud (Bélanger et al., 2013) and aerosol (Floutsi et al., 2016). Refinements to methods for the selection of the spatial decay parameter in large chl datasets will also impact on uncertainty; a simple fixed distribution was used here, as automatic fitting approaches failed. The most important of these suggestions are expanded upon as proposals in Section 6.4.

6.3 Remaining Refinements to Technique

Using a Bayesian spatio-temporal model technique leads to clear improvements when analysing trends in global chl, and the spTimer package provides flexibility to allow these techniques to be fully explored. However some aspects of the package, and this technique in general, could be improved in future to aid research applications. The main issue limiting investigations of global satellite-derived data within this package is the relatively slow computation time due to the volume of data. This is despite the important implementation of knots, and the reduced spatial correlation matrix, which allows this work to be done. This is particularly problematic for the trend term here, which is slow to converge, taking up to multiple hours per region. This was handled by computing regions in parallel, an adaptation for this package to handle multiple shorter MCMC chains in parallel would allow for further improvements to computation speed. The more general scientific aspects of this package that could be improved are as follows.

Refinements of this research could be made to resolve some minor issues that have been identified in this work. The first of these is the definition of regions, which applies to Chapters 3 - 5. The chosen definition for regions was Longhurst provinces, which is based on physical and biogeochemical characteristics (Longhurst 1995; 1998). Longhurst regions were defined in the late 1990s and, although widely used, do have some drawbacks. The first of these drawbacks is that boundaries are rectilinear i.e. are often simply a line of constant, or near constant, longitude or latitude. This is problematic as there is no clear reason why an ocean would be divided rectilinearly when most ocean features are controlled by ocean physics. The second problem is that areas of biogeochemistry are expected to change over time, both long-term with climate change and on the shorter timescale of decadal variability, meaning that region boundaries should also be changing correspondingly (e.g. Devred et al., 2007; Fay & McKinley, 2014). This suggests that two approaches should be used in future to define boundaries. First, boundaries should be selected based on data from the time period being studied. Second, time-dependent or “dynamic” regions should be used, allowing changes over seasonal and interannual scales. Several approaches have been suggested to do this, primarily by considering information from chl and its environmental drivers (e.g. Devred et al., 2007; Gaetan et al., 2016; Reygondeau et al., 2013).

The use of dynamic regions may cause interactions with the spatial correlation components of the statistical analysis, particularly near region boundaries. The degree of interaction would depend on the method used to allow dynamic regions within the spatio-temporal model. The general expectation is that the grid cells nearest a boundary would have differing amounts of spatial correlation information over time, as the region area increases and decreases, which would have a corresponding impact on the confidence of model fits. Having predefined regions in this work means that some regions, at certain times, contain data that are not biogeochemically similar to the overall region. Including data which is not biogeochemically similar within a region may have an effect on trend estimates, although this should affect only a relatively small percentage of any given region. Given the latitudinal patterns seen, where regions of similar trend are usually grouped, this effect may be minimal although allowing for these changes should lead to a further improvement in fit accuracy.

The modelling of seasonality is another area suitable for refinement, as it did cause problems with model fit in the Pacific Subarctic Gyres Province (West) (Region 18) when using the ESA OC-CCI v3.1 dataset (i.e. in Chapters 4 & 5). Seasonality in the chl data is modelled using a monthly factor, which does not permit changes in phenology over time. Changes in phenology have been observed in this work and other studies (e.g. Racault et al., 2012). Previous studies have shown that allowing for annual variations in phenology leads to better model fits (e.g. Vantrepotte & Mélin, 2011). Thus, in future, the spatio-temporal method could be improved by allowing annual variations in phenology. This may be increasingly important as model studies have projected further changes in phenology as a response to climate change (Henson et al., 2013; 2018).

Anisotropic spatial correlation may be a further way to improve the method. The spatial correlation used in this study is isotropic, i.e. the spatial correlation is only related to the distance between points, not the direction between points. Oceanic currents and fronts mean that chl is typically expected to develop with a directional component. Although using isotropic spatial correlation leads to a substantially more accurate fit than not considering spatial correlation, it remains a simplification permitting easier computation. Incorporating anisotropic spatial correlation would be expected to further improve the model fit by more accurately representing the directional nature of the spatial relationship within chl data.

6.4 Future Avenues to Improving our Understanding

Bayesian spatio-temporal models have been applied here to improving trend estimation in chl for the first time. However, there are still several avenues for further improvement of our understanding of chl trends. The first major outstanding question is whether spatio-temporal models can detect climate change driven trend signals with a shorter record length than is required for models without spatial correlation. The model with spatial correlation shows an improved model fit, i.e. a better representation of the chl data, particularly over seasonal and decadal timescales. As the fit is improved over these two timescales, it may also improve the fit over longer timescales, and may thus shorten the record length required to distinguish a climate change driven trend from natural variability. Using statistical analyses without spatial correlation, model projections have been used to quantify the record length required to distinguish trends from natural variability (e.g. Henson et al., 2010; 2016); a similar analysis, using a spatio-temporal method, should be performed.

In situ data are not employed in this study, however they can provide important information. Whilst satellite data has much higher spatial coverage and temporal resolution than in situ data, in situ data samples the water column directly and, in certain regions, has a significantly longer record length than satellite data. Some studies have explored merging in situ and satellite ocean chl data to make use of the advantages of in situ data (e.g. Raitsos et al., 2014; Sravanthi et al., 2017; Uz et al., 2017). Additionally, hierarchical Bayesian spatial models have been used to merge satellite and in situ lacustrine chl data (Wilkie et al., 2015). Using in situ data could be an approach to improving the estimation of chl trends, particularly by providing a longer record. This may be especially beneficial in the North Atlantic, where in situ data has been collected by scientific cruises since the 1950s, and by commercial vessels within the semi-quantitative CPR (Continuous Plankton Recorder) project from 1948 (Boyer et al., 2013; Richardson et al., 2006). CPR data has been previously merged with satellite data by e.g. Raitsos et al. (2005; 2014), however this study did not consider spatial correlation during the analysis. As the present work shows that accounting for spatial correlation improves accuracy of model fit, as compared to not accounting for spatial correlation, merging using spatial correlation has the potential to improve the fit between CPR and satellite data. Alternatively, in situ data could be incorporated as Bayesian priors to help constrain trends, similar to how coupled physical-biogeochemical models are used in the present work. In situ data provides longer coverage and could compensate for the disadvantages of satellite data, potentially allowing for further improvements in trend estimation by helping to isolate the trend signal from decadal variability.

In situ data can also be used to improve our understanding of coastal regions, which are relatively well sampled compared to much of the open ocean, due to ease of access (e.g. Boyce et al., 2014; Valente et al., 2016). However, these regions have data quality issues in satellite derived ocean colour resulting from other constituents in the atmosphere and water column, which are both found in much higher concentrations in coastal regions (e.g. Hyde et al., 2007; Mélin et al., 2007; Schollaert et al., 2003). Merging with in situ data allows the poorer satellite data quality to be corrected for, as in situ data are not affected by atmospheric noise and are more easily corrected for noise in the water column (Coelho et al., 2017). Such a spatial correlation approach has been performed using lacustrine chl data from both satellites and regularly collected in situ records (Wilkie et al. 2015). Using spatially varying coefficients may further help remove noise, which is not expected to be constant over a region. Thus, the spatio-temporal model could potentially be applied to coastal data, which was omitted in this study due to data quality issues. The importance of these regions to human activities including fishing should make this a priority.

6.5 Finishing Words

The use of Bayesian spatio-temporal techniques offers an approach to more accurately estimating trends in chl data and understanding their uncertainties. Such techniques may be particularly important for chl data due to the high degree of spatial variability and the relatively short record length. The Bayesian framework also allows data from multiple sources to be incorporated, compensating for their individual deficits. However, Bayesian spatio-temporal techniques also have key limitations that prevent them being more widely used in the scientific community. The two main limitations are a) that the techniques currently need a specialised knowledge of statistics in order to be applied, or even considered, and b) that such techniques are substantially computationally slower than more traditional approaches. More work is needed to resolve these limitations, but it is clear that spatio-temporal modelling is now offering an enhanced approach for studying global long-term change.

Appendices

Appendix A

A.1 Trace Plots of Trend Parameter for Spatial Correlation Model

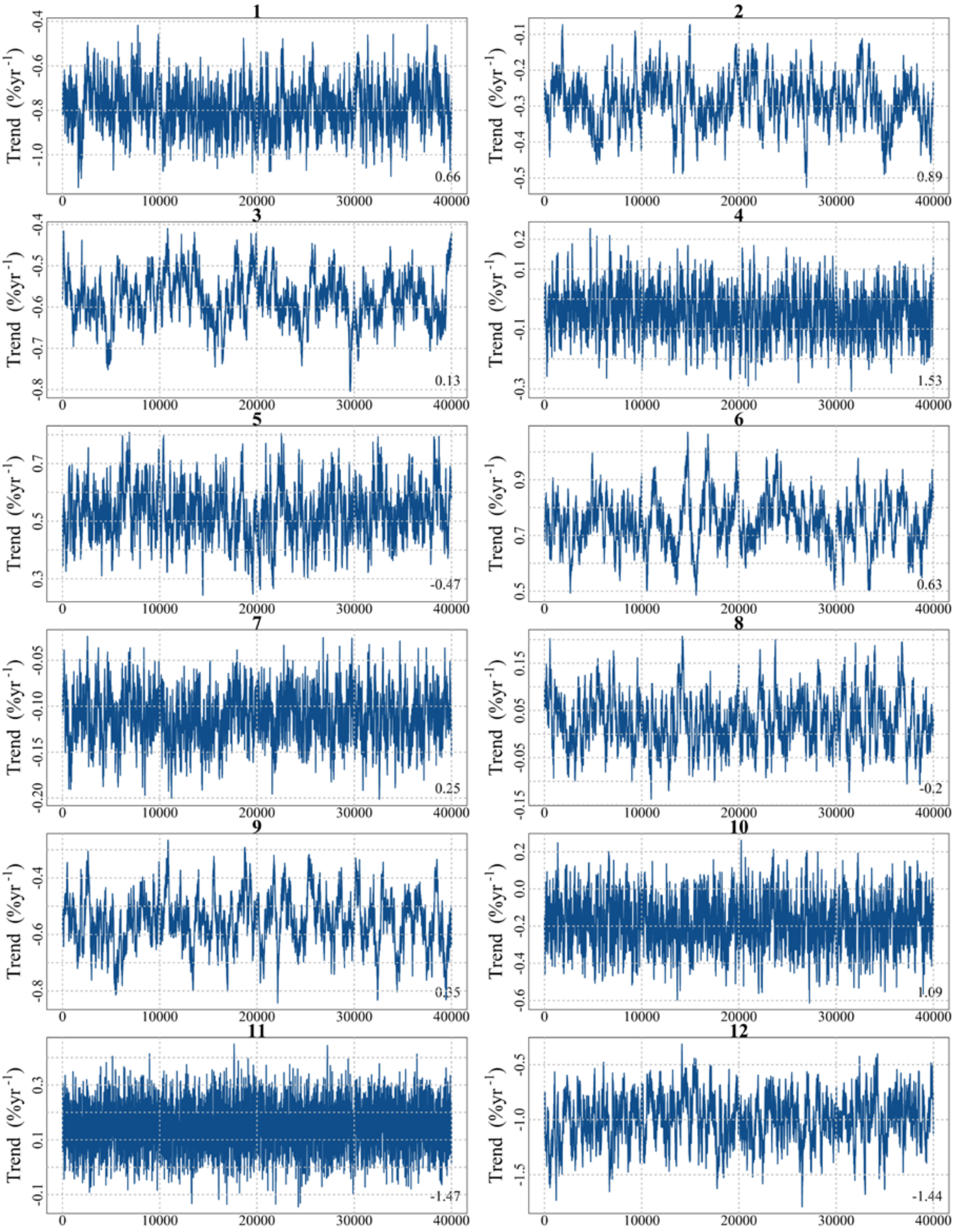

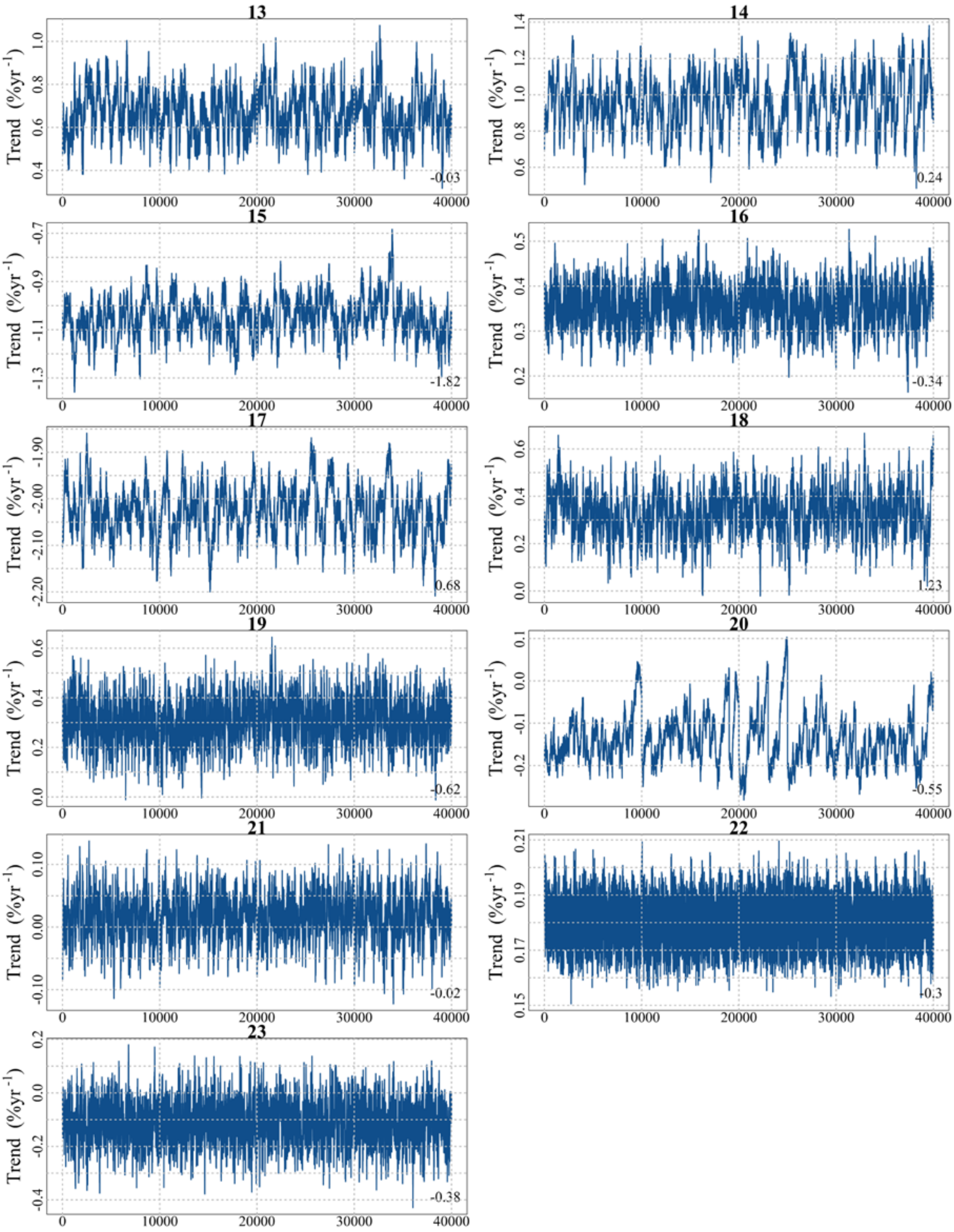

Example trace plots for the trend parameter in all regions for the model with spatial correlation terms, i.e. the slowest converging parameter in the scenario with the most complex model. Numbers in the bottom right corner of each plot indicate results of the Geweke diagnostic, a value greater than 1.96 would indicate that the first and last parts of the chain are significantly different, implying non-convergence, although none such are found here.

A.2 Chl Trend Posterior Probability Densities

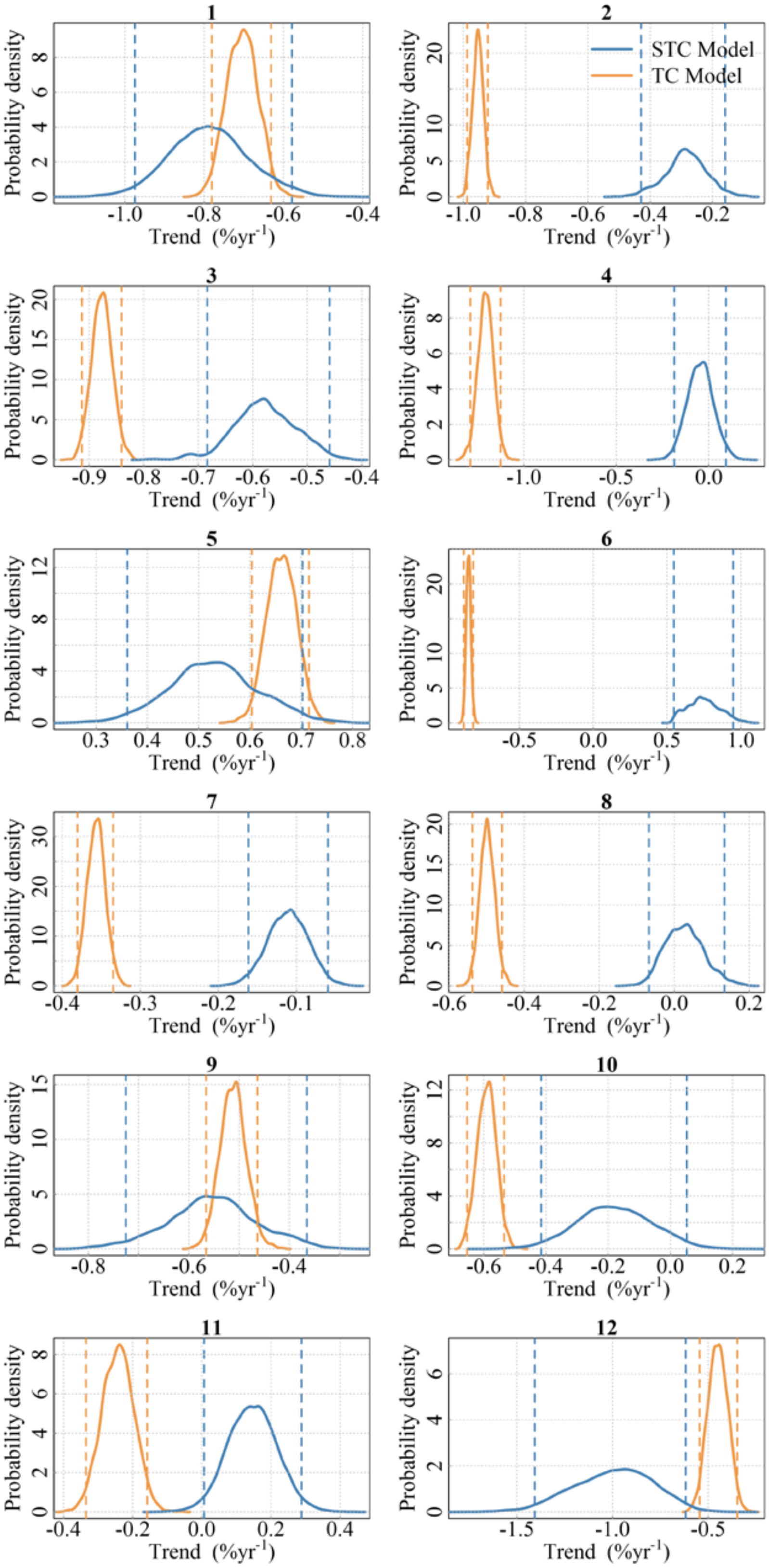

Appendix A

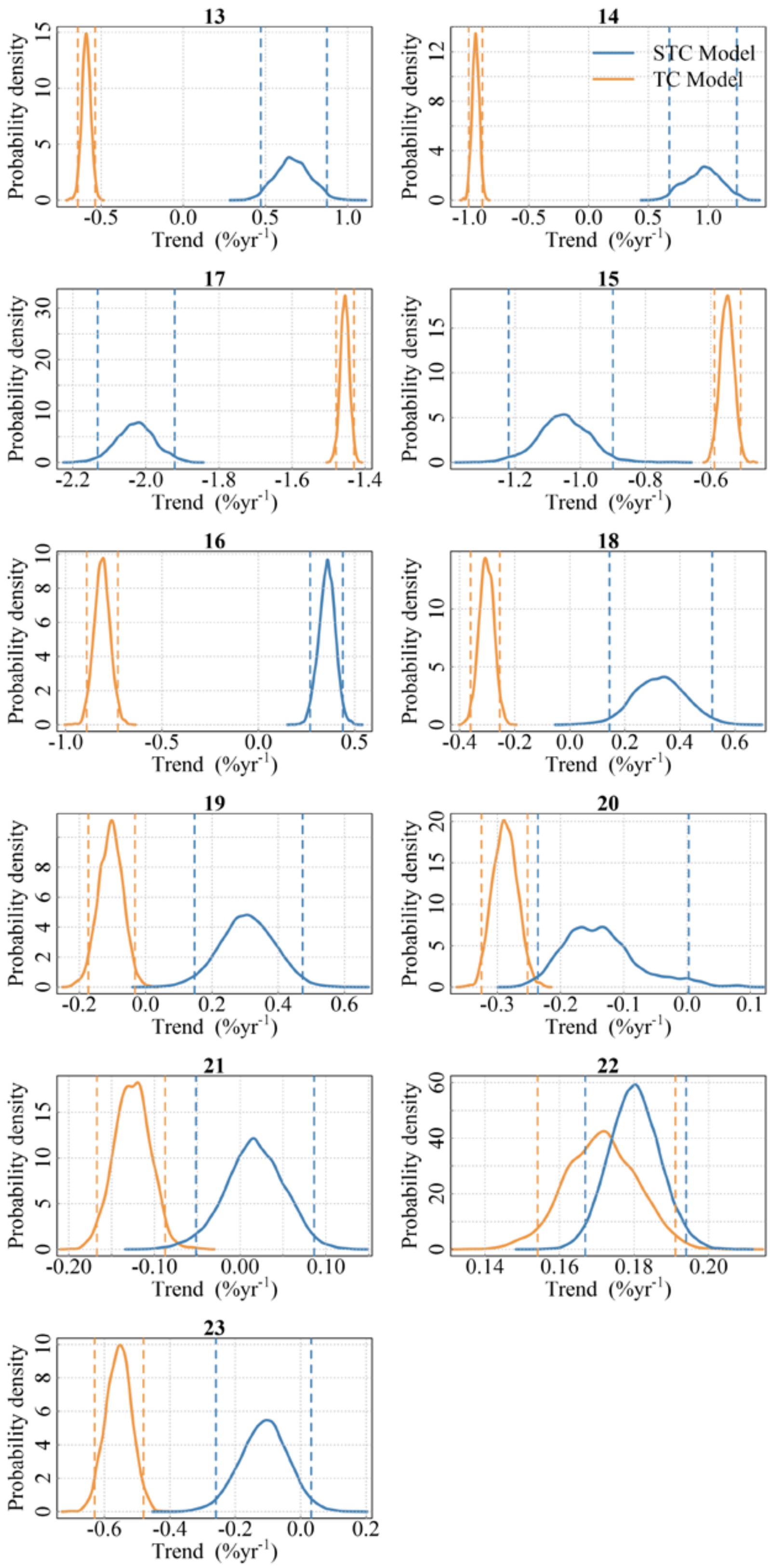

Posterior probability densities (solid lines) for the chl trend values. STC refers to the model with spatio-temporal correlation and TC refers to the model with temporal correlation only (i.e. without spatial correlation). A trend is considered unlikely if its 95 % credible interval (represented by the vertical dashed lines) contains zero. Refer to Table 2.2 for region names.

A.3 Region Average Chlorophyll Time-series

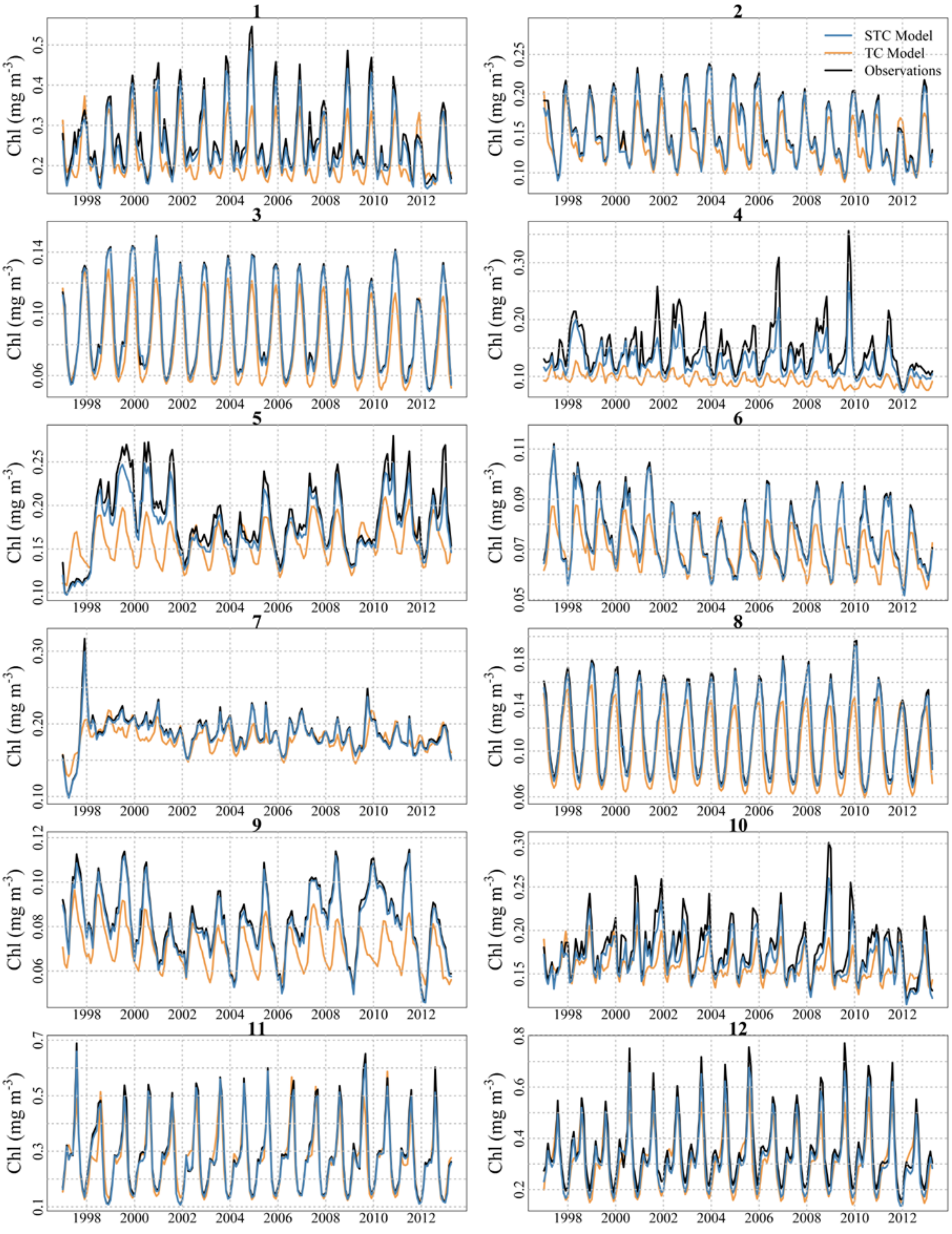

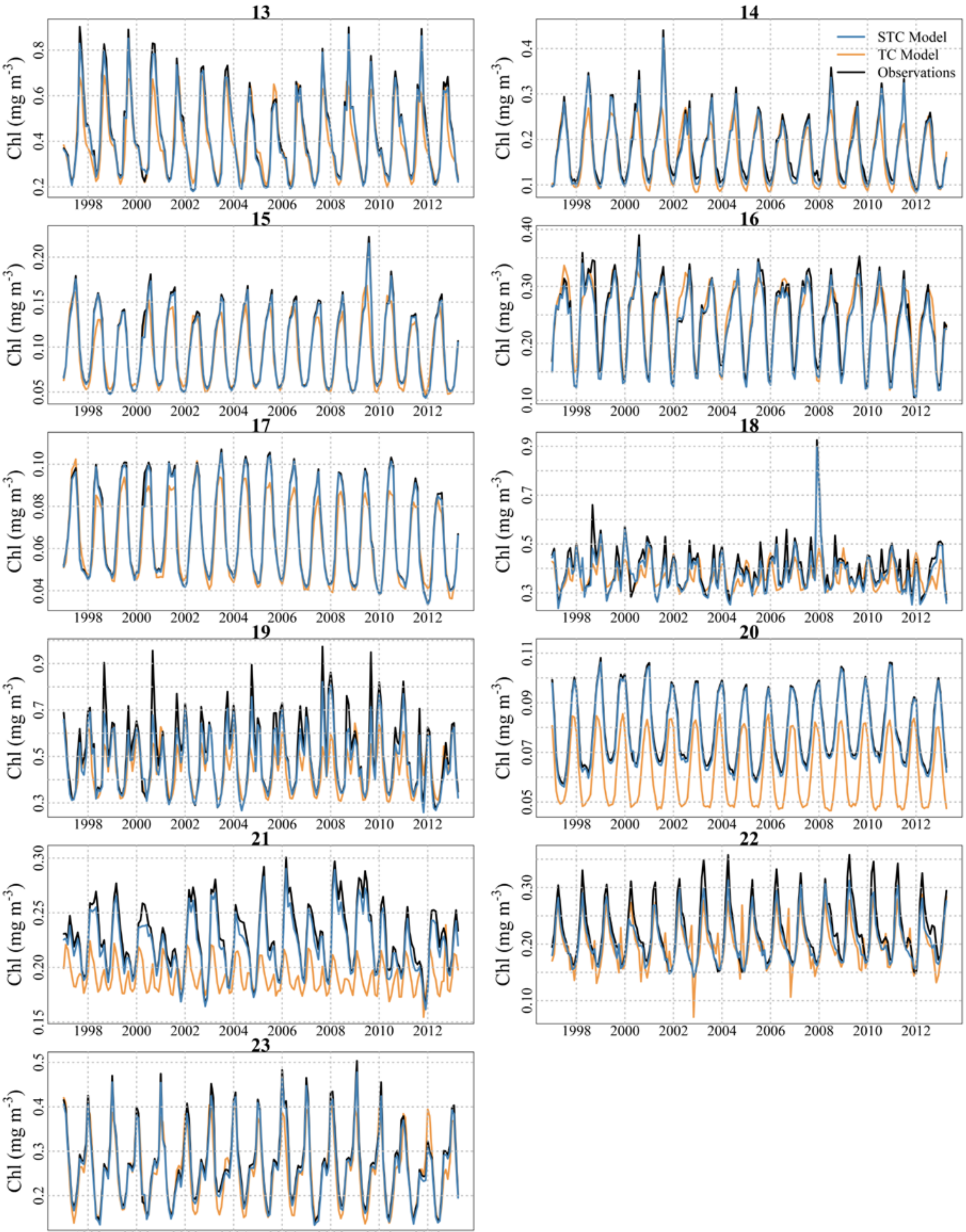

Averaged time-series for each region, showing the observed chl values and the chl values estimated by the two model types: STC refers to the model with spatio-temporal correlation and TC refers to the model with temporal correlation only (i.e. without spatial correlation). Refer to Table 2.2 for region names.

A.4 Region Average Time-Series of Chlorophyll Deviations from Observations

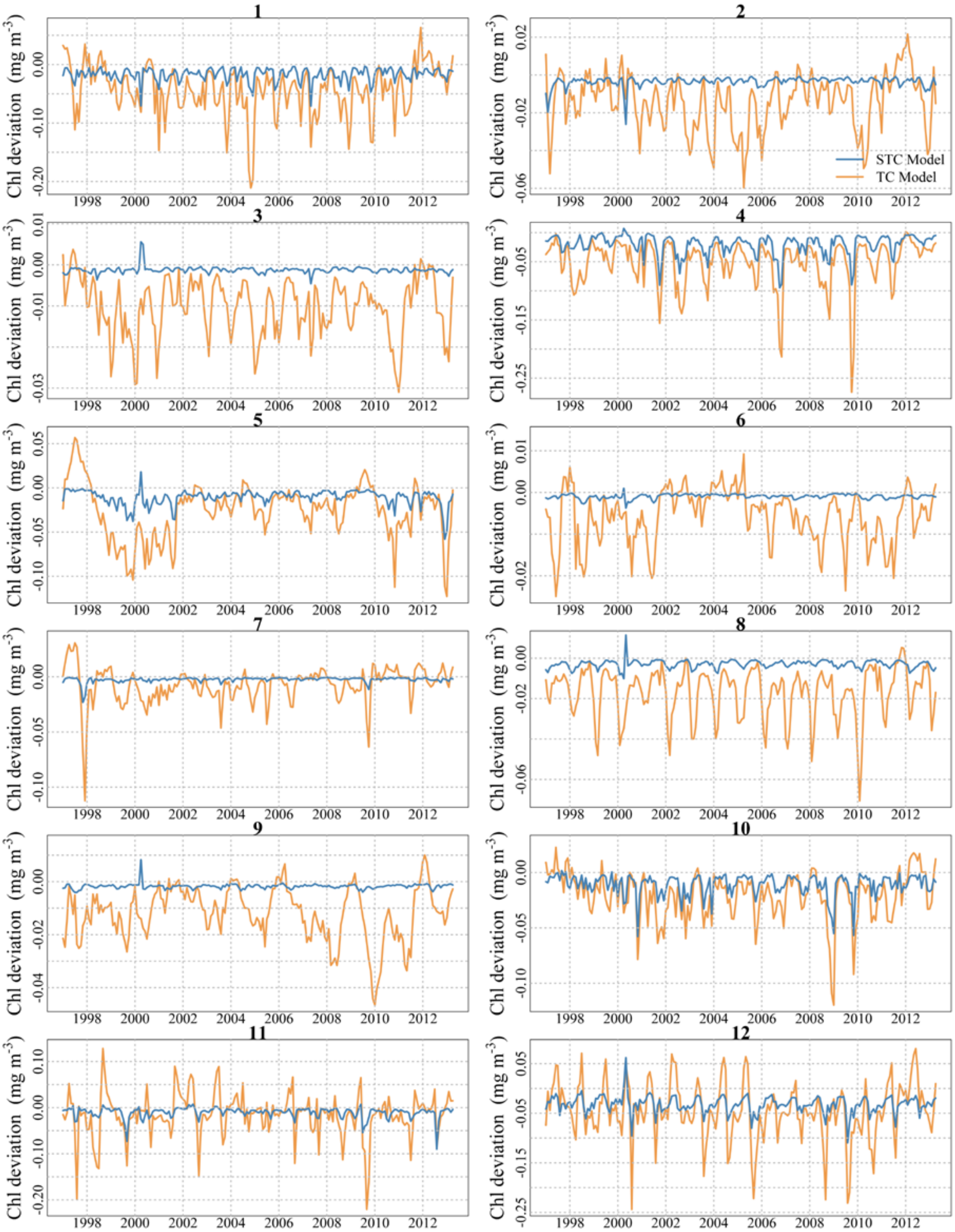

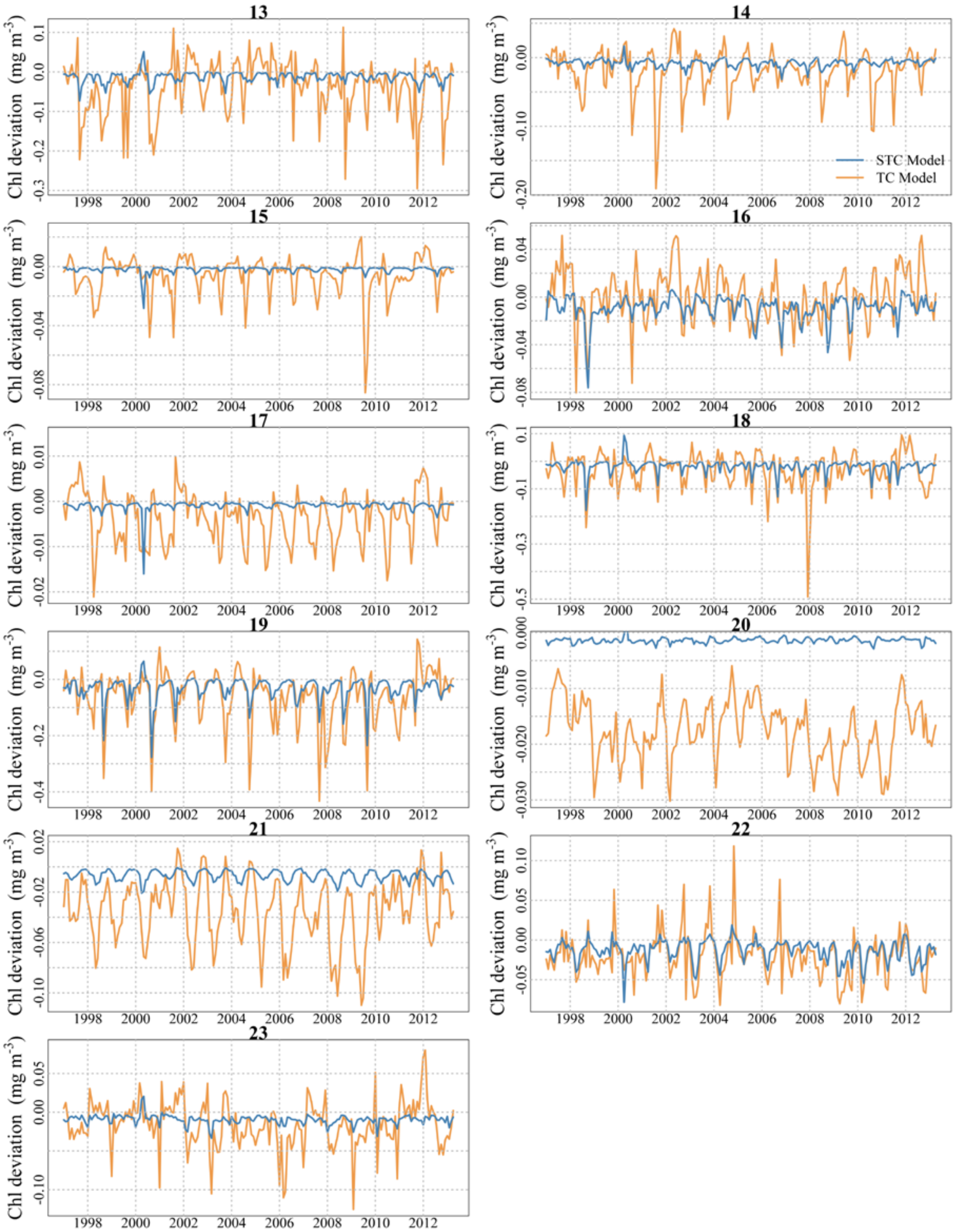

Averaged time-series for each region, showing the modelled chl deviation from observations for the two model types: STC refers to the model with spatio-temporal correlation and TC refers to the model with temporal correlation only (i.e. without spatial correlation). A value of zero means the modelled values are the same as observations, i.e. the closer a value is to zero the more accurate the model is at that time. Refer to Table 2.2 for region names

Appendix B

B.1 Global Average Time-Series for CMIP5 Model Chlorophyll

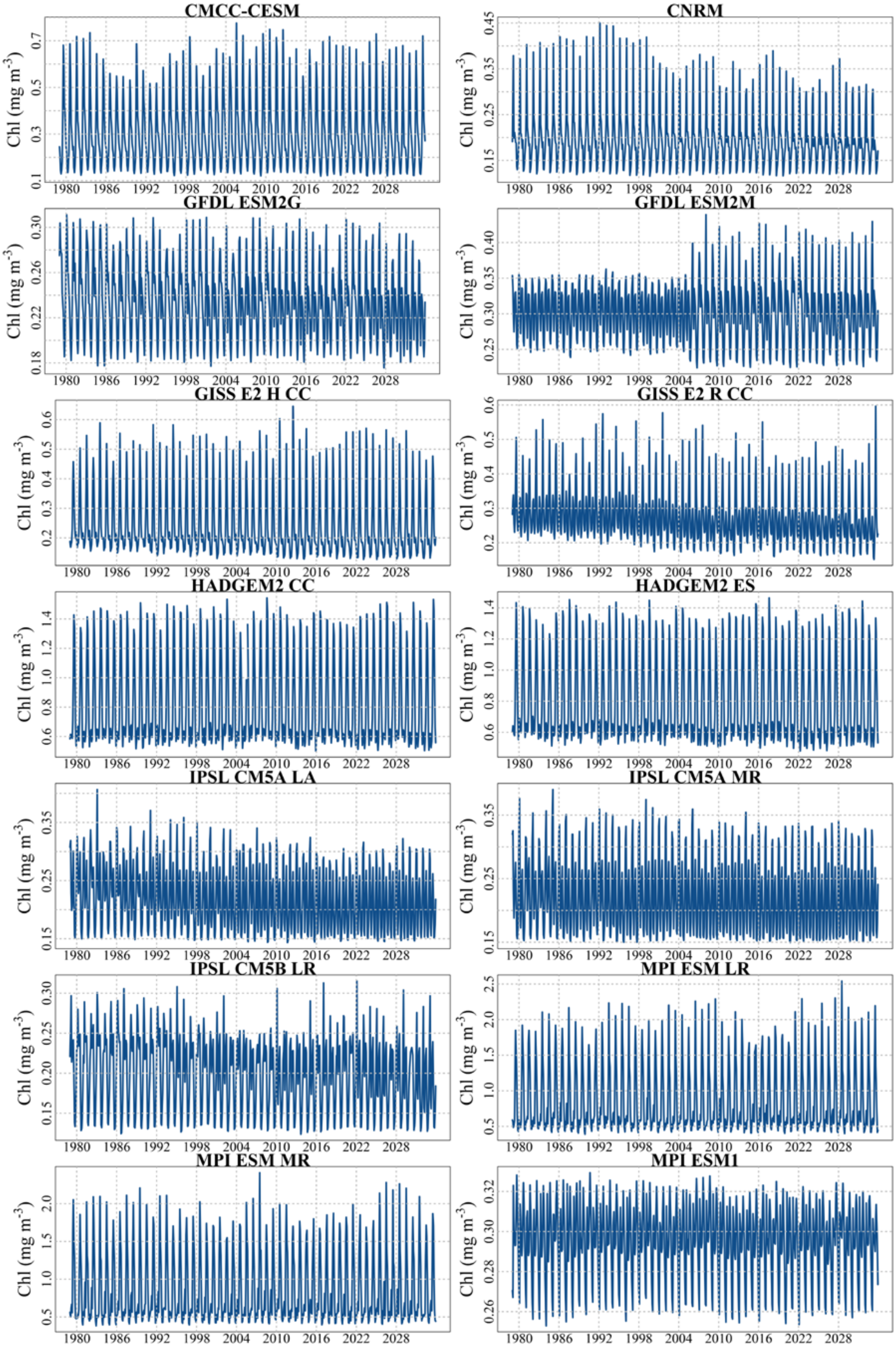

Appendix B

Global averaged time-series for each CMIP5 model. Note the different average, seasonal variability, and trend between the models. Note also that the GFDL ESM2M model shows different seasonal variability between the historical and RCP8.5 runs. Each of the individual ensembles for a given model show identical global average time-series. Refer to Table 2.2 for region names.

Appendix C

C.1 Full Trend Difference Values (ESA OC-CCI)

Uncertainty and trend differences between the five discontinuity scenarios and the scenario with no discontinuity, as well as the discontinuity magnitude (averaged for scenarios with more than one discontinuity), for all regions when using the ESA OC-CCI dataset. See Figure 5.1 for a graphical representation. Region names can be found in Table 2.2.

Region	Scenario	Trend Difference (% yr^{-1})	Uncertainty Difference (% yr^{-1})	Discontinuity Magnitude (log(mg m^{-3}))
1	M	-0.78	0.25	0.13
	S	0.61	0.32	-0.091
	MS	-0.57	0.78	0.11
	MV	-0.54	0.70	0.11
	MSV	-0.44	0.84	0.10
2	M	-0.63	0.13	0.11
	S	0.68	0.24	-0.098
	MS	-0.14	0.51	0.055
	MV	-0.12	0.47	0.053
	MSV	-0.037	0.66	0.041
3	M	-0.033	0.14	-0.0062
	S	0.47	0.24	-0.081
	MS	0.80	0.50	-0.083
	MV	-0.85	0.43	0.088
	MSV	0.16	0.56	-0.073
4	M	-2.0	0.15	0.34
	S	1.6	0.22	-0.23
	MS	-1.3	0.61	0.27

Region	Scenario	Trend Difference (% yr $^{-1}$)	Uncertainty Difference (% yr $^{-1}$)	Discontinuity Magnitude (log(mg m $^{-3}$))
	MV	-1.6	0.47	0.30
	MSV	-1.3	0.60	0.26
5	M	-1.7	0.18	0.29
	S	1.6	0.25	-0.24
	MS	-0.42	0.69	0.16
	MV	-0.57	0.60	0.17
	MSV	-0.1	0.79	0.12
6	M	-0.63	0.073	0.11
	S	0.89	0.15	-0.14
	MS	0.51	0.48	-0.0098
	MV	2.6	0.38	-0.27
	MSV	2.2	0.51	-0.13
7	M	-0.61	0.071	0.11
	S	0.94	0.091	-0.14
	MS	0.53	0.23	-0.014
	MV	-0.14	0.20	0.052
	MSV	0.45	0.25	-0.028
8	M	0.0038	0.11	0.0056
	S	-0.76	0.20	0.12
	MS	-1.5	0.32	0.17
	MV	-2.1	0.40	0.24
	MSV	-2.3	0.47	0.22
9	M	-1.3	0.16	0.23
	S	1.1	0.30	-0.17

Region	Scenario	Trend Difference (% yr $^{-1}$)	Uncertainty Difference (% yr $^{-1}$)	Discontinuity Magnitude (log(mg m $^{-3}$))
	MS	-0.68	0.59	0.16
	MV	-2.5	0.55	0.36
	MSV	-1.4	0.57	0.19
10	M	-0.31	0.14	0.055
	S	0.47	0.23	-0.072
	MS	0.20	0.59	-0.0006
	MV	0.11	0.50	0.0076
	MSV	0.32	0.63	-0.014
11	M	-0.32	0.19	0.055
	S	0.053	0.24	-0.0083
	MS	-0.62	0.66	0.087
	MV	-0.35	0.54	0.059
	MSV	-0.54	0.65	0.089
12	M	-0.046	0.53	0.0084
	S	0.45	0.64	-0.051
	MS	0.48	1.4	-0.057
	MV	0.014	1.4	0.016
	MSV	0.40	1.6	-0.056
13	M	-0.33	0.32	0.056
	S	0.41	0.34	-0.050
	MS	0.34	1.0	0.012
	MV	0.37	1.1	-0.018
	MSV	0.20	1.2	0.023
14	M	-0.67	0.33	0.092
	S	1.3	0.39	-0.20

Region	Scenario	Trend Difference (% yr^{-1})	Uncertainty Difference (% yr^{-1})	Discontinuity Magnitude (log(mg m^{-3}))
	MS	1.7	1.5	-0.11
	MV	1.4	0.95	-0.14
	MSV	2.1	1.1	-0.17
15	M	0.97	0.20	-0.16
	S	-0.53	0.33	0.095
	MS	0.96	0.72	-0.16
	MV	0.61	0.51	-0.12
	MSV	0.70	0.77	-0.14
16	M	-0.58	0.054	0.10
	S	0.66	0.087	-0.099
	MS	-0.011	0.23	0.042
	MV	0.56	0.21	-0.030
	MSV	0.45	0.24	0.012
17	M	-0.17	0.10	0.026
	S	-0.92	0.098	0.14
	MS	-2.2	0.34	0.24
	MV	-2.4	0.29	0.27
	MSV	-2.9	0.32	0.31
18	M	-1.5	0.26	0.27
	S	3.2	0.36	-0.48
	MS	2.7	0.99	-0.18
	MV	0.33	0.68	0.064
	MSV	2.5	0.93	-0.25
19	M	-0.24	0.18	0.045

Region	Scenario	Trend Difference (% yr^{-1})	Uncertainty Difference (% yr^{-1})	Discontinuity Magnitude (log(mg m^{-3}))
	S	0.81	0.27	-0.12
	MS	1.1	0.72	-0.095
	MV	3.2	0.59	-0.35
	MSV	2.6	0.71	-0.19
20	M	-0.72	0.077	0.11
	S	0.13	0.20	-0.012
	MS	-1.1	0.38	0.16
	MV	-1.4	0.38	0.17
	MSV	-1.3	0.40	0.18
21	M	-0.073	0.069	0.014
	S	0.40	0.10	-0.058
	MS	0.94	0.41	-0.085
	MV	0.13	0.35	0.0031
	MSV	0.66	0.42	-0.081
22	M	0.11	0.016	-0.20
	S	-0.17	0.034	0.026
	MS	-0.094	0.071	0.0022
	MV	0.60	0.064	-0.075
	MSV	0.22	0.077	-0.0085
23	M	-1.1	0.19	0.20
	S	0.53	0.27	-0.079
	MS	-1.5	0.64	0.24
	MV	-1.4	0.57	0.22
	MSV	-1.6	0.65	0.25

C.2 Full Trend Difference Values (GlobColour)

Uncertainty and trend differences between the five discontinuity scenarios and the scenario with no discontinuity, as well as the discontinuity magnitude (averaged for scenarios with more than one discontinuity), for all regions when using the GlobColour dataset. See Figure 5.5 for a graphical representation. Region names can be found in Table 2.2.

Region	Scenario	Trend Difference (% yr^{-1})	Uncertainty Difference (% yr^{-1})	Discontinuity Magnitude (log(mg m^{-3}))
1	M	-0.069	0.30	-0.067
	S	-0.49	0.38	0.00040
	MS	0.36	0.93	-0.11
	MV	-0.67	0.92	-0.00020
	MSV	-0.13	1.1	-0.093
2	M	-0.30	0.26	0.069
	S	0.090	0.28	-0.018
	MS	-0.46	0.77	0.078
	MV	-1.3	0.69	0.18
	MSV	-0.92	0.85	0.11
3	M	0.49	0.21	0.038
	S	1.1	0.30	-0.080
	MS	1.1	0.67	-0.010
	MV	-0.49	0.72	0.15
	MSV	0.44	0.66	0.0067
4	M	-2.6	0.14	0.26
	S	0.015	0.24	-0.17
	MS	-2.1	0.66	0.21
	MV	-3.4	0.49	0.34

Region	Scenario	Trend Difference (% yr^{-1})	Uncertainty Difference (% yr^{-1})	Discontinuity Magnitude (log(mg m^{-3}))
	MSV	-2.7	0.59	0.23
5	M	-0.51	0.32	0.28
	S	2.4	0.41	-0.20
	MS	0.23	0.84	0.20
	MV	-0.33	0.73	0.26
	MSV	0.12	0.92	0.19
6	M	-0.14	0.20	0.052
	S	0.71	0.30	-0.064
	MS	0.36	0.58	0.0074
	MV	2.4	0.61	-0.23
	MSV	1.8	0.78	-0.080
7	M	-0.057	0.077	0.058
	S	0.88	0.099	-0.090
	MS	0.71	0.27	-0.024
	MV	-0.89	0.22	0.15
	MSV	0.041	0.30	-0.005
8	M	0.031	0.18	0.12
	S	-0.19	0.20	0.13
	MS	-2.4	0.59	0.37
	MV	-3.5	0.46	0.52
	MSV	-3.8	0.52	0.48
9	M	-0.32	0.18	0.17
	S	1.6	0.28	-0.15
	MS	0.34	0.68	0.091
	MV	-2.3	0.64	0.37

Region	Scenario	Trend Difference (% yr^{-1})	Uncertainty Difference (% yr^{-1})	Discontinuity Magnitude (log(mg m^{-3}))
	MSV	-0.94	0.66	0.15
10	M	-1.5	0.18	-0.056
	S	-1.4	0.28	-0.052
	MS	-0.38	0.60	-0.18
	MV	-1.7	0.59	-0.034
	MSV	-0.82	0.66	-0.17
11	M	0.52	0.25	0.049
	S	0.74	0.30	0.011
	MS	0.014	0.79	0.1
	MV	-0.63	0.69	0.18
	MSV	-0.44	0.84	0.14
12	M	-0.7	0.39	0.020
	S	-0.16	0.70	-0.070
	MS	0.11	1.7	-0.082
	MV	-1	1.6	0.060
	MSV	-0.31	1.9	-0.047
13	M	-0.36	0.39	0.11
	S	1.4	0.67	-0.14
	MS	0.48	1.5	0.021
	MV	-1.3	1.3	0.21
	MSV	-0.25	1.4	0.068
14	M	-1.9	0.35	0.24
	S	1.4	0.49	-0.30
	MS	0.53	1.3	0.0090

Region	Scenario	Trend Difference (% yr $^{-1}$)	Uncertainty Difference (% yr $^{-1}$)	Discontinuity Magnitude (log(mg m $^{-3}$))
15	MV	-0.31	1.2	0.059
	MSV	0.58	1.5	-0.038
	M	1.9	0.33	-0.22
	S	-0.66	0.44	0.20
	MS	1.2	0.83	-0.14
16	MV	-0.13	0.77	0.011
	MSV	0.23	0.91	-0.079
	M	-0.87	0.17	0.20
	S	1	0.18	-0.11
	MS	-0.98	0.38	0.21
17	MV	-0.38	0.38	0.15
	MSV	-0.68	0.42	0.20
	M	1.6	0.11	-0.18
	S	-1.3	0.17	0.28
	MS	-0.79	0.37	0.065
18	MV	-2.5	0.38	0.29
	MSV	-2.3	0.56	0.19
	M	-1.8	0.57	0.46
	S	5.6	0.54	-0.71
	MS	4.2	1.2	-0.19
19	MV	0.96	1.1	0.14
	MSV	4.1	1.2	-0.28
	M	-0.33	0.32	0.22
	S	2	0.4	-0.15
	MS	0.11	0.89	0.17

Region	Scenario	Trend Difference (% yr $^{-1}$)	Uncertainty Difference (% yr $^{-1}$)	Discontinuity Magnitude (log(mg m $^{-3}$))
	MV	2.5	0.88	-0.095
	MSV	1.5	0.94	0.10
20	M	-0.44	0.11	0.095
	S	0.044	0.24	0.017
	MS	-1.3	0.49	0.16
	MV	-1.5	0.39	0.24
	MSV	-1.7	0.61	0.20
21	M	0.36	0.14	-0.023
	S	0.43	0.18	-0.032
	MS	0.94	0.41	-0.085
	MV	0.13	0.35	0.0031
	MSV	0.66	0.42	-0.081
22	M	0.36	0.021	0.015
	S	0.13	0.040	0.047
	MS	-0.39	0.080	0.093
	MV	0.94	0.070	-0.053
	MSV	0.13	0.086	0.083
23	M	-1.6	0.27	0.34
	S	1.1	0.36	-0.12
	MS	-2.5	0.79	0.44
	MV	-2.2	0.73	0.41
	MSV	-2.6	0.86	0.46

C.3 Posterior Probability Densities for the S-scenario

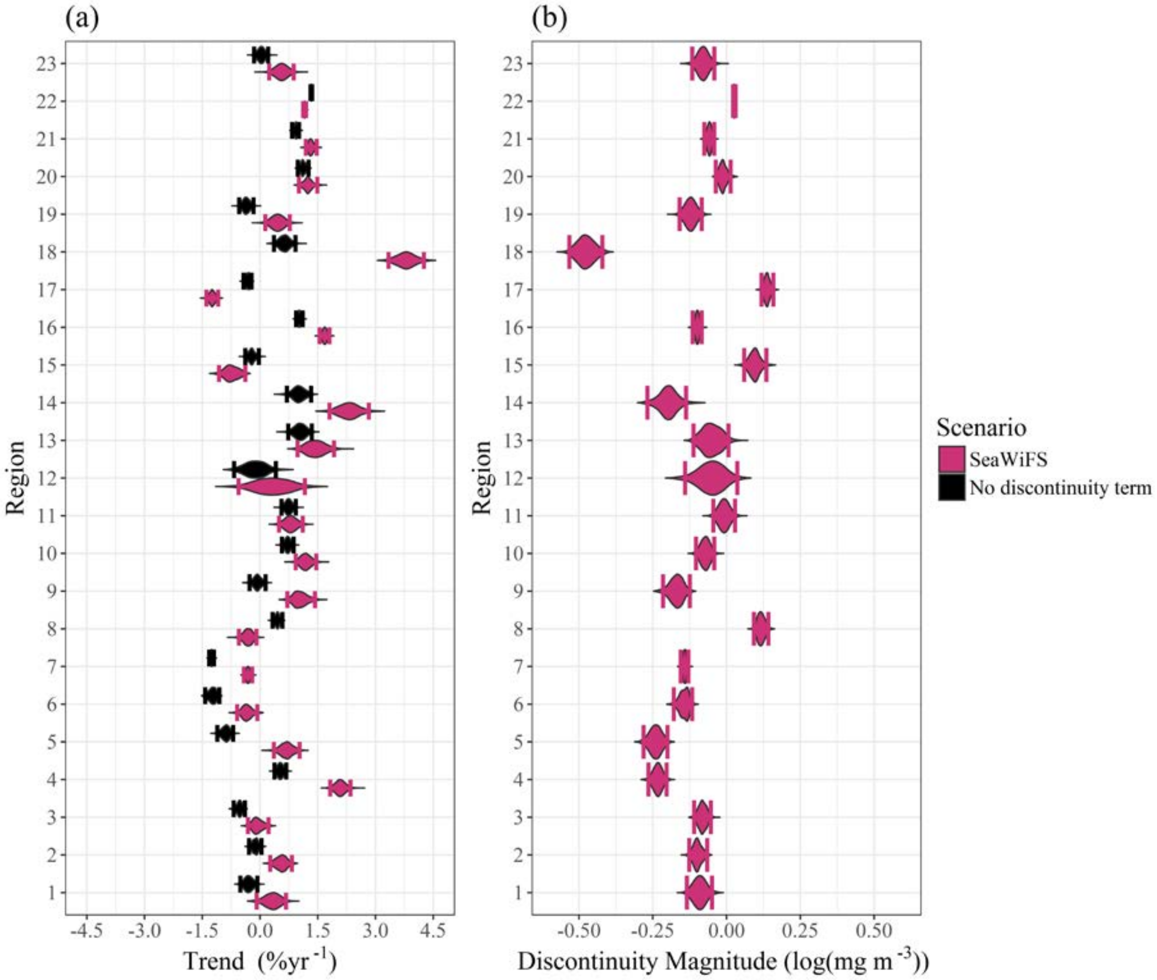

Posterior probability density of (a) the trend and (b) the discontinuity magnitude for each region in the SeaWiFS discontinuity scenario and the scenario with no discontinuities. The vertical lines represent the credible interval boundaries. There are two key differences: the increase in uncertainty when discontinuities are considered and the difference in the modal trend which can be up to 3.2 % yr^{-1}. 18 of 23 regions show a trend that is statistically likely to be different between the two scenarios. Region names can be found in Table 2.2.

C.4 Posterior Probability Densities for the MS-scenario

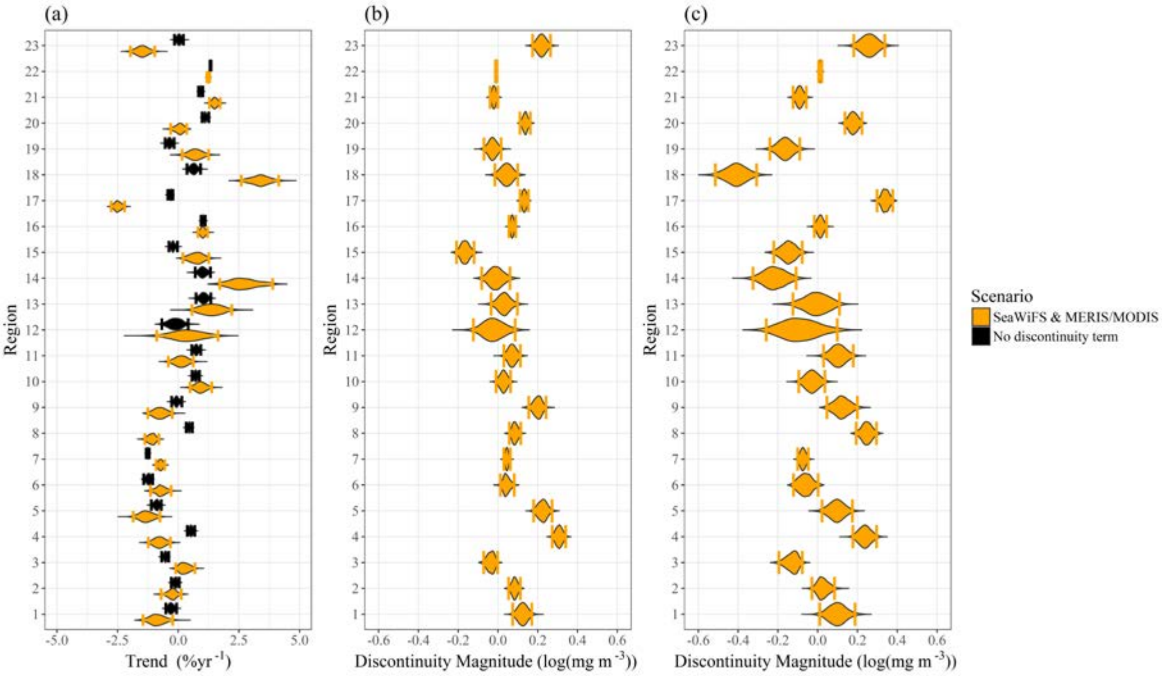

Posterior probability density of (a) the trend, (b) the discontinuity magnitude at the MERIS/MODIS discontinuity, and (c) the discontinuity magnitude at the SeaWiFS discontinuity for each region in the combined MERIS/MODIS and SeaWiFS discontinuity scenario and the scenario with no discontinuities. The vertical lines represent the credible interval boundaries. There are two key differences: the increase in uncertainty when discontinuities are considered and the difference in the modal trend which can be up to 2.8 % yr $^{-1}$. 13 of 23 regions show a trend that is statistically likely to be different between the two scenarios. Region names can be found in Table 2.2.

C.5 Posterior Probability Densities for the MV-scenario

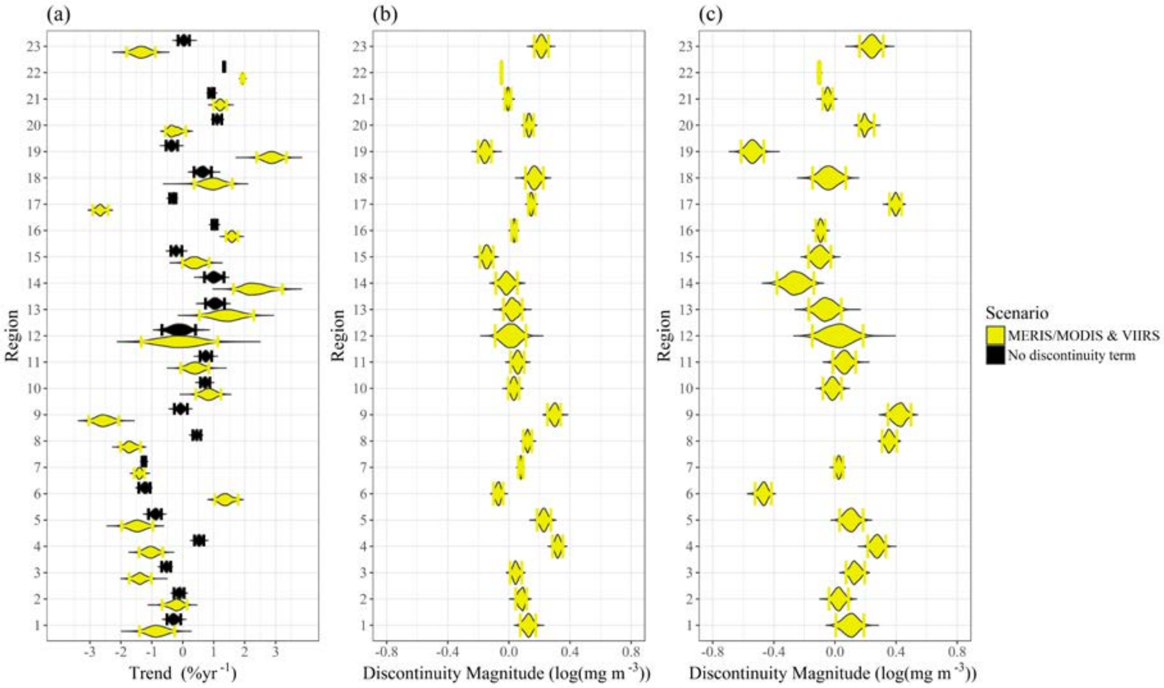

Posterior probability density of (a) the trend, (b) the discontinuity magnitude at the MERIS/MODIS discontinuity, and (c) the discontinuity magnitude at the VIIRS discontinuity for each region in the combined MERIS/MODIS and VIIRS discontinuity scenario and the scenario with no discontinuities. The vertical lines represent the credible interval boundaries. There are two key differences: the increase in uncertainty when discontinuities are considered and the difference in the modal trend which can be up to 3.2 % yr^{-1}. 13 of 23 regions show a trend that is statistically likely to be different between the two scenarios. Region names can be found in Table 2.2.

C.6 Posterior Probability Densities for the MSV-scenario

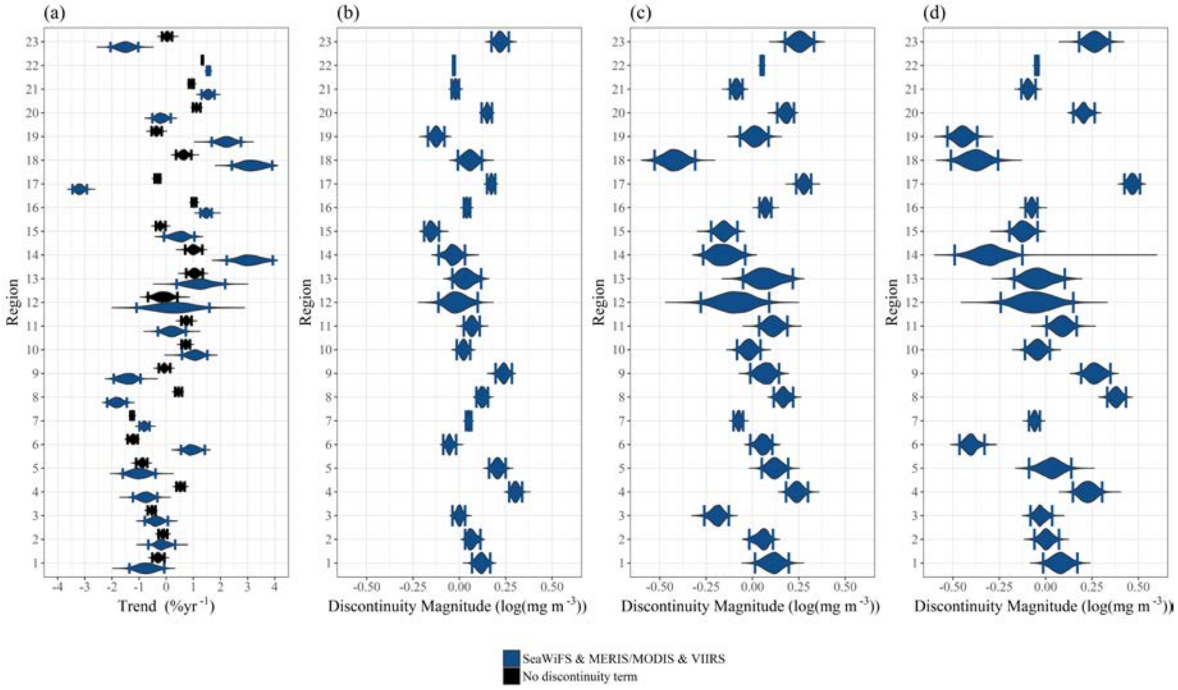

Posterior probability density of (a) the trend, (b) the discontinuity magnitude at the MERIS/MODIS discontinuity, (c) the discontinuity magnitude at the SeaWiFS discontinuity, and (d) the discontinuity magnitude at the VIIRS discontinuity for each region in the combined MERIS/MODIS, SeaWiFS, and VIIRS discontinuity scenario and the scenario with no discontinuities. The vertical lines represent the credible interval boundaries. There are two key differences: the increase in uncertainty when discontinuities are considered and the difference in the modal trend which can be up to 2.9 % yr^{-1}. 14 of 23 regions show a trend that is statistically likely to be different between the two scenarios. Region names can be found in Table 2.2.

List of References

Antoine, D., Morel, A., Gordon, H. R., Banzon, V. F., & Evans, R. H. (2005). Bridging ocean color observations of the 1980s and 2000s in search of long-term trends. Journal of Geophysical Research-Oceans, 110(C6), C06009. DOI: 10.1029/2004jc002620

Aumont, O., & Bopp, L. (2006). Globalizing results from ocean in situ iron fertilization studies. Global Biogeochemical Cycles, 20(2), GB2017. DOI: 10.1029/2005GB002591

Bakar, K. S., & Sahu, S. K. (2015). sp Timer: Spatio-Temporal Bayesian Modeling Using R. Journal of Statistical Software, 63(15), 1-32. DOI: 10.18637/jss.v063.i15

Banerjee, S., Gelfand, A. E., Finley, A. O., & Sang, H. (2008). Gaussian Predictive Process Models for Large Spatial Data Sets. Journal of the Royal Statistical Society B, 70, 825-848. DOI: 10.1111/j.1467-9868.2008.00663.x

Beaulieu, C., Henson, S. A., Sarmiento, J. L., Dunne, J. P., Doney, S. C., Rykaczewski, R. R., & Bopp, L. (2013). Factors challenging our ability to detect long-term trends in ocean chlorophyll. Biogeosciences, 10(4), 2711-2724. DOI: 10.5194/bg-10-2711-2013

Behrenfeld, M. J., R. T. O'Malley, E. S. Boss, T. K. Westberry, J. R. Graff, K. H. Halsey, A. J. Milligan, D. A. Siegel, and M. B. Brown (2016), Revaluating ocean warming impacts on global phytoplankton, Nat Clim Change, 6(3), 323-330. DOI: 10.1038/Nclimate2838.

Behrenfeld, M. J., O'Malley, R. T., Siegel, D. A., McClain, C. R., Sarmiento, J. L., Feldman, G. C., . . . Boss, E. S. (2006). Climate-driven trends in contemporary ocean productivity. Nature, 444(7120), 752-755. DOI: 10.1038/nature05317

Behrenfeld, M. J., Randerson, J. T., McClain, C. R., Feldman, G. C., Los, S. O., Tucker, C. J., . . . Pollack, N. H. (2001). Biospheric primary production during an ENSO transition. Science, 291(5513), 2594-2597. DOI: 10.1126/science.1055071

Bélanger, S., Babin, M., & Tremblay, J. (2013). Increasing cloudiness in Arctic damps the increase in phytoplankton primary production due to sea ice receding. Biogeosciences, 10(6), 4087-4101. DOI: 10.5194/bg-10-4087-2013

Boatman, T. G., Lawson, T., & Geider, R. J. (2017). A Key Marine Diazotroph in a Changing Ocean: The Interacting Effects of Temperature, CO2 and Light on the Growth of Trichodesmium erythraeum IMS101. Plos One, 12(1), e0168796. DOI: 10.1371/journal.pone.0168796

Bojinski, S., Verstraete, M., Peterson, T. C., Richter, C., Simmons, A., & Zemp, M. (2014). The Concept of Essential Climate Variables in Support of Climate Research, Applications, and Policy. Bulletin of the American Meteorological Society, 95(9), 1431-1443. DOI: 10.1175/Bams-D-13-00047.1

Bopp, L., Aumont, O., Belviso, S., & Monfray, P. (2003). Potential impact of climate change on marine dimethyl sulfide emissions. Tellus Series B-Chemical and Physical Meteorology, 55(1), 11-22. DOI: 10.1034/j.1600-0889.2003.042.x

Bopp, L., Monfray, P., Aumont, O., Dufresne, J. L., Le Treut, H., Madec, G., . . . Orr, J. C. (2001). Potential impact of climate change on marine export production. Global Biogeochemical Cycles, 15(1), 81-99. DOI: 10.1029/1999gb001256

Bopp, L., Resplandy, L., Orr, J. C., Doney, S. C., Dunne, J. P., Gehlen, M., . . . Vichi, M. (2013). Multiple stressors of ocean ecosystems in the 21st century: projections with CMIP5 models. Biogeosciences, 10(10), 6225-6245. DOI: 10.5194/bg-10-6225-2013

Boyce, D. G., Dowd, M., Lewis, M. R., & Worm, B. (2014). Estimating global chlorophyll changes over the past century. Progress in Oceanography, 122, 163-173. DOI: 10.1016/j.pocean.2014.01.004

Boyce, D. G., Lewis, M. R., & Worm, B. (2010). Global phytoplankton decline over the past century. Nature, 466(7306), 591-596. DOI: 10.1038/Nature09268

Boyce, D. G., & Worm, B. (2015). Patterns and ecological implications of historical marine phytoplankton change. Marine Ecology Progress Series, 534, 251-272. DOI: 10.3354/meps11411

Boyer, T. P., Antonov, J. I., Baranova, O. K., Coleman, C., Garcia, H. E., Grodsky, A., . . . Zweng, M. M. (2013). World Ocean Database 2013. In S. Levitus & A. Mishonov (Eds.), NOAA Atlas NESDIS 72 (pp. 209). Silver Spring, MD. DOI: 10.7289/V54Q7S16

Brewin, R. J. W., Mélin, F., Sathyendranath, S., Steinmetz, F., Chuprin, A., & Grant, M. (2014). On the temporal consistency of chlorophyll products derived from three ocean-colour sensors. Isprs Journal of Photogrammetry and Remote Sensing, 97, 171-184. DOI: 10.1016/j.isprsjprs.2014.08.013

Bryant, D. A. (2003). The beauty in small things revealed. Proceedings of the National Academy of Sciences of the United States of America, 100(17), 9647-9649. DOI: 10.1073/pnas.1834558100

Cabré, A., Marinov, I., & Leung, S. (2015). Consistent global responses of marine ecosystems to future climate change across the IPCC AR5 earth system models. Climate Dynamics, 45(5-6), 1253-1280. DOI: 10.1007/s00382-014-2374-3

Campbell, J. W. (1995). The lognormal distribution as a model for bio-optical variability in the sea. Journal of Geophysical Research: Oceans, 100(C7), 13237-13254. DOI: 10.1029/95JC00458

Chandler, R. E., & Scott, E. M. (2011). Other Issues. Statistical methods for trend detection and analysis in the environmental sciences, 235-263, Chichester, West Sussex, U.K.: Wiley.

Charlson, R. J., Lovelock, J. E., Andreae, M. O., & Warren, S. G. (1987). Oceanic Phytoplankton, Atmospheric Sulfur, Cloud Albedo and Climate. Nature, 326(6114), 655-661. DOI: 10.1038/326655a0

Chassot, E., Bonhommeau, S., Dulvy, N. K., Mélin, F., Watson, R., Gascuel, D., & Le Pape, O. (2010). Global marine primary production constrains fisheries catches. Ecology Letters, 13(4), 495-505. DOI: 10.1111/j.1461-0248.2010.01443.x

Cheung, W. W. L., Lam, V. W. Y., Sarmiento, J. L., Kearney, K., Watson, R., Zeller, D., & Pauly, D. (2010). Large-scale redistribution of maximum fisheries catch potential in the global ocean under climate change. Global Change Biology, 16(1), 24-35. DOI: 10.1111/j.1365-2486.2009.01995.x

Cheung, W. W. L., Watson, R., & Pauly, D. (2013). Signature of ocean warming in global fisheries catch. Nature, 497(7449), 365. DOI: 10.1038/nature12156

Christensen, J. H., K. Krishna Kumar, E. Aldrian, S.-I. An, I.F.A. Cavalcanti, M. de Castro, . . . Zhou, T. (2013). Climate Phenomena and their Relevance for Future Regional Climate Change. In T. F. Stocker, D. Qin, G.-K. Plattner, M. Tignor, S.K. Allen, J. Boschung, A. Nauels, Y. Xia, V. Bex, & P. M. Midgley (Eds.), Climate Change 2013: The Physical Science Basis. Contribution of Working Group I to the

Fifth Assessment Report of the Intergovernmental Panel on Climate Change (pp. 1029–1136). Cambridge: Cambridge University Press.

Chuprin, A., Jackson, T., Grant, M., & Zühlke, M. (2017), System Prototype Specification (3.1.0). Ocean Colour Climate Change Initiative (OC_CCI) – Phase Two, Plymouth Marine Laboratory. Retrieved from http://www.esa-oceancolour-cci.org/?q=webfm_send/704

Coelho, C., Heim, B., Foerster, S., Brosinsky, A., & de Araújo, J. C. (2017). In Situ and Satellite Observation of CDOM and Chlorophyll-a Dynamics in Small Water Surface Reservoirs in the Brazilian Semiarid Region. Water, 9(12), 913. DOI: 10.3390/w9120913

Collins, M., R. Knutti, J. Arblaster, J.-L. Dufresne, T. Fichefet, P. Friedlingstein, . . . Wehner, M. (2013). Long-term Climate Change: Projections and Predictability. In T. F. Stocker, D. Qin, G.-K. Plattner, M. Tignor, S.K. Allen, J. Boschung, A. Nauels, Y. Xia, V. Bex, & P. M. Midgley (Eds.), Climate Change 2013: The Physical Science Basis. Contribution of Working Group I to the Fifth Assessment Report of the Intergovernmental Panel on Climate Change (pp. 1029–1136). Cambridge: Cambridge University Press.

Cressie, N. A. C., & Wikle, C. K. (2011). Space-time: the next frontier. Statistics for spatio-temporal data, 1-16, Hoboken, N.J.: Wiley.

Dandonneau, Y., Deschamps, P. Y., Nicolas, J. M., Loisel, H., Blanchot, J., Montel, Y., . . . Becu, G. (2004). Seasonal and interannual variability of ocean color and composition of phytoplankton communities in the North Atlantic, equatorial Pacific and South Pacific. Deep-Sea Research Part Ii-Topical Studies in Oceanography, 51(1-3), 303-318. DOI: 10.1016/j.dsr2.2003.07.018

Devred, E., Sathyendranath, S., & Platt, T. (2007). Delineation of ecological provinces using ocean colour radiometry. Marine Ecology Progress Series, 346, 1-13. DOI: 10.3354/meps07149

Ding, Q., Chen, X. J., Hilborn, R., & Chen, Y. (2017). Vulnerability to impacts of climate change on marine fisheries and food security. Marine Policy, 83, 55-61. DOI: 10.1016/j.marpol.2017.05.011

Djavidnia, S., Mélin, F., & Hoepffner, N. (2010). Comparison of global ocean colour data records. Ocean Science, 6(1), 61-76. DOI: 10.5194/os-6-61-2010

Doney, S. C. (1999). Major challenges confronting marine biogeochemical modeling. Global Biogeochemical Cycles, 13(3), 705-714. DOI: 10.1029/1999gb900039

Doney, S. C. (2006). Oceanography - Plankton in a warmer world. Nature, 444(7120), 695-696. DOI: 10.1038/444695a

Ducklow, H. W., Doney, S. C., & Steinberg, D. K. (2009). Contributions of Long-Term Research and Time-Series Observations to Marine Ecology and Biogeochemistry. Annual Review of Marine Science, 1, 279-302. DOI: 10.1146/annurev.marine.010908.163801

Dulvy, N. K., Rogers, S. I., Jennings, S., Stelzenmuller, V., Dye, S. R., & Skjoldal, H. R. (2008). Climate change and deepening of the North Sea fish assemblage: a biotic indicator of warming seas. Journal of Applied Ecology, 45(4), 1029-1039. DOI: 10.1111/j.1365-2664.2008.01488.x

Dunne, J. P., John, J. G., Shevliakova, E., Stouffer, R. J., Krasting, J. P., Malyshev, S. L., . . . Zadeh, N. (2013). GFDL’s ESM2 Global Coupled Climate–Carbon Earth System Models. Part II: Carbon System Formulation and Baseline Simulation Characteristics. Journal of Climate, 26(7), 2247-2267. DOI: 10.1175/jcli-d-12-00150.1

Durack, P. J., Wijffels, S. E., & Matear, R. J. (2012). Ocean Salinities Reveal Strong Global Water Cycle Intensification During 1950 to 2000. Science, 336(6080), 455-458. DOI: 10.1126/science.1212222

Edwards, K. F., Thomas, M. K., Klausmeier, C. A., & Litchman, E. (2016). Phytoplankton growth and the interaction of light and temperature: A synthesis at the species and community level. Limnology and Oceanography, 61(4), 1232-1244. DOI: 10.1002/lno.10282

England, M. H., McGregor, S., Spence, P., Meehl, G. A., Timmermann, A., Cai, W., . . . Santoso, A. (2014). Recent intensification of wind-driven circulation in the Pacific and the ongoing warming hiatus. Nature Clim. Change, 4(3), 222-227. DOI: 10.1038/nclimate2106

Eppley, R. W. (1972). Temperature and phytoplankton growth in the sea. Fish. Bull., 70, 1063.

Fay, A. R., & McKinley, G. A. (2014). Global open-ocean biomes: mean and temporal variability. Earth System Science Data, 6(2), 273-284. DOI: 10.5194/essd-6-273-2014

Field, C. B., Behrenfeld, M. J., Randerson, J. T., & Falkowski, P. (1998). Primary production of the biosphere: Integrating terrestrial and oceanic components. Science, 281(5374), 237-240. DOI: 10.1126/science.281.5374.237

Finley, A. O., Sang, H. Y., Banerjee, S., & Gelfand, A. E. (2009). Improving the performance of predictive process modeling for large datasets. Computational Statistics & Data Analysis, 53(8), 2873-2884. DOI: 10.1016/j.csda.2008.09.008

Floutsi, A. A., Korras-Carraca, M. B., Matsoukas, C., Hatzianastassiou, N., & Biskos, G. (2016). Climatology and trends of aerosol optical depth over the Mediterranean basin during the last 12 years (2002-2014) based on Collection 006 MODIS-Aqua data. Science of the Total Environment, 551, 292-303. DOI: 10.1016/j.scitotenv.2016.01.192

Ford, D., & Barciela, R. (2017). Global marine biogeochemical reanalyses assimilating two different sets of merged ocean colour products. Remote Sensing of Environment, 203, 40-54. DOI: 10.1016/j.rse.2017.03.040

Friedland, K. D., Stock, C., Drinkwater, K. F., Link, J. S., Leaf, R. T., Shank, B. V., . . . Fogarty, M. J. (2012). Pathways between Primary Production and Fisheries Yields of Large Marine Ecosystems. Plos One, 7(1). DOI: 10.1371/journal.pone.0028945

Fu, W. W., Randerson, J. T., & Moore, J. K. (2016). Climate change impacts on net primary production (NPP) and export production (EP) regulated by increasing stratification and phytoplankton community structure in the CMIP5 models. Biogeosciences, 13(18), 5151-5170. DOI: 10.5194/bg-13-5151-2016

Gaetan, C., Girardi, P., Pastres, R., & Mangin, A. (2016). Clustering Chlorophyll-a satellite data using quantiles. Ann. Appl. Stat., 10(2), 964-988. DOI: 10.1214/16-AOAS923

Galbraith, E. D., Carozza, D. A., & Bianchi, D. (2017). A coupled human-Earth model perspective on long-term trends in the global marine fishery. Nature Communications, 8. DOI: 10.1038/ncomms14884

Gelfand, A. E., & Smith, A. F. M. (1990). Sampling-Based Approaches to Calculating Marginal Densities. Journal of the American Statistical Association, 85(410), 398-409. DOI: 10.1080/01621459.1990.10476213

Geweke, J. (1992). Evaluating the accuracy of sampling-based approaches to calculating posterior moments. In Bayesian Statistics 4 (ed JM Bernado, JO Berger, AP Dawid and AFM Smith). Clarendon Press, Oxford, UK.

Giorgetta, M. A., Jungclaus, J., Reick, C. H., Legutke, S., Bader, J., Bottinger, M., . . . Stevens, B. (2013). Climate and carbon cycle changes from 1850 to 2100 in MPI-ESM simulations for the Coupled Model Intercomparison Project phase 5. Journal of Advances in Modeling Earth Systems, 5(3), 572-597. DOI: 10.1002/jame.20038

Grant, M., Jackson, T., Chuprin, A., Sathyendranath, S., Zühlke, M., Dingle, J., Storm, T., Boettcher, M., & Fomferra, N. (2017), Product User Guide (3.1.0). Ocean Colour Climate Change Initiative (OC_CCI) – Phase Two, Plymouth Marine Laboratory. Retrieved from http://www.esa-oceancolour-cci.org/?q=webfm_send/684

Gregg, W. W., & Casey, N. W. (2007). Modeling coccolithophores in the global oceans. Deep Sea Research Part II: Topical Studies in Oceanography, 54(5), 447-477. DOI: 10.1016/j.dsr2.2006.12.007

Gregg, W. W., & Casey, N. W. (2010). Improving the consistency of ocean color data: A step toward climate data records. Geophysical Research Letters, 37, L04605. DOI: 10.1029/2009gl041893

Gregg, W. W., Conkright, M. E., Ginoux, P., O'Reilly, J. E., & Casey, N. W. (2003). Ocean primary production and climate: Global decadal changes. Geophysical Research Letters, 30(15), 1809. DOI: 10.1029/2003gl016889

Gregg, W. W., & Rousseaux, C. S. (2014). Decadal trends in global pelagic ocean chlorophyll: A new assessment integrating multiple satellites, in situ data, and models. Journal of Geophysical Research-Oceans, 119(9), 5921-5933. DOI: 10.1002/2014jc010158

Gregg, W. W., Rousseaux, C. S., & Franz, B. A. (2017). Global trends in ocean phytoplankton: a new assessment using revised ocean colour data. Remote Sensing Letters, 8(12), 1102-1111. DOI: 10.1080/2150704X.2017.1354263

Grimaud, G. M., Mairet, F., Sciandra, A., & Bernard, O. (2017). Modeling the temperature effect on the specific growth rate of phytoplankton: a review. Reviews in Environmental Science and Bio-Technology, 16(4), 625-645. DOI: 10.1007/s11157-017-9443-0

Hammond, M. L., Beaulieu, C., Sahu, S. K., & Henson, S. A. (2017). Assessing trends and uncertainties in satellite-era ocean chlorophyll using space-time modeling. Global Biogeochemical Cycles, 31(7), 1103-1117. DOI: 10.1002/2016gb005600

Handcock, M. S., & Stein, M. L. (1993). A Bayesian-Analysis of Kriging. Technometrics, 35(4), 403-410. DOI: 10.2307/1270273

Handcock, M. S., & Wallis, J. R. (1994). An Approach to Statistical Spatial-Temporal Modeling of Meteorological Fields. Journal of the American Statistical Association, 89(426), 368-378. DOI: 10.2307/2290832

Hawkins, E., & Sutton, R. (2012). Time of emergence of climate signals. Geophysical Research Letters, 39, L01702. DOI: 10.1029/2011gl050087

Hays, G. C., Richardson, A. J., & Robinson, C. (2005). Climate change and marine plankton. Trends in Ecology & Evolution, 20(6), 337-344. DOI: 10.1016/j.tree.2005.03.004

Hegerl, G. C., Hoegh-Guldberg, O., Casassa, G., Hoerling, M., Kovats, S., Parmesan, C., . . . Stott, P. (2010). Good practice guidance paper on detection and attribution related to anthropogenic climate change. Paper presented at the IPCC Expert Meeting on Detection and Attribution Related to Anthropogenic Climate Change 2010, Geneva, Switzerland.

Henson, S. A., Beaulieu, C., & Lampitt, R. (2016). Observing climate change trends in ocean biogeochemistry: when and where. Global Change Biology, 22(4), 1561-1571. DOI: 10.1111/gcb.13152

Henson, S.A., Cole, H.S., Beaulieu, C., & Yool, A. (2013). The impact of global warming on seasonality of ocean primary production. Biogeosciences, 10(6), 4357-4369. DOI: 10.5194/bg-10-4357-2013

Henson, S. A., Cole, H. S., Hopkins, J., Martin, A. P., & Yool, A. (2018). Detection of climate change-driven trends in phytoplankton phenology. Global Change Biology, 24(1), e101-e111. DOI: 10.1111/gcb.13886

Henson, S. A., Dunne, J. P., & Sarmiento, J. L. (2009). Decadal variability in North Atlantic phytoplankton blooms. Journal of Geophysical Research-Oceans, 114, C04013. DOI: 10.1029/2008jc005139

Henson, S. A., Sanders, R., Madsen, E., Morris, P. J., Le Moigne, F., & Quartly, G. D. (2011). A reduced estimate of the strength of the ocean's biological carbon pump. Geophysical Research Letters, 38, L04606. DOI: 10.1029/2011gl046735

Henson, S. A., Sarmiento, J. L., Dunne, J. P., Bopp, L., Lima, I., Doney, S. C., . . . Beaulieu, C. (2010). Detection of anthropogenic climate change in satellite records of ocean chlorophyll and productivity. Biogeosciences, 7(2), 621-640. DOI: 10.5194/bg-7-621-2010

Hoegh-Guldberg, O., Cai, R., Poloczanska, E. S., Brewer, P. G., Sundby, S., Hilmi, K., . . . Jung, S. (2014). The Ocean. In V. R. Barros, C. B. Field, D. J. Dokken, M. D. Mastrandrea, K. J. Mach, T. E. Bilir, M. Chatterjee, K. L. Ebi, Y. O. Estrada, R. C. Genova, B. Girma, E. S. Kissel, A. N. Levy, S. MacCracken, P. R. Mastrandrea, & L. L. White (Eds.), Climate Change 2014: Impacts, Adaptation, and Vulnerability. Part B: Regional Aspects. Contribution of Working Group II to the Fifth Assessment Report of the Intergovernmental Panel of Climate Change (pp. 1682). Cambridge, United Kingdom and New York, NY, USA: Cambridge University Press.

Hyde, K. J. W., O'Reilly, J. E., & Oviatt, C. A. (2007). Validation of SeaWiFS chlorophyll a in Massachusetts Bay. Continental Shelf Research, 27(12), 1677-1691. DOI: 10.1016/j.csr.2007.02.002

Ilyina, T., Six, K. D., Segschneider, J., Maier-Reimer, E., Li, H., & Núñez-Riboni, I. (2013). Global ocean biogeochemistry model HAMOCC: Model architecture and performance as component of the MPI-Earth system model in different CMIP5 experimental realizations. Journal of Advances in Modeling Earth Systems, 5(2), 287-315. DOI: 10.1029/2012MS000178

Irwin, A. J., & Oliver, M. J. (2009). Are ocean deserts getting larger? Geophysical Research Letters, 36, L18609. DOI: 10.1029/2009gl039883

Jin, X., & Gruber, N. (2003). Offsetting the radiative benefit of ocean iron fertilization by enhancing N2O emissions. Geophysical Research Letters, 30(24), 2249. DOI: 10.1029/2003gl018458

Kaufman, Y., Koren, I., Remer, L., Tanré, D., Ginoux, P., & Fan, S. (2005). Dust transport and deposition observed from the Terra-Moderate Resolution Imaging Spectroradiometer (MODIS) spacecraft over the Atlantic Ocean. Journal of Geophysical Research: Atmospheres, 110(D10). DOI: 10.1029/2003JD004436

Keller, M. D., Bellows, W. K., & Guillard, R. R. L. (1989). Dimethyl Sulfide Production in Marine-Phytoplankton. Acs Symposium Series, 393, 167-182.

Kirtman, B., S.B. Power, J.A. Adedoyin, G.J. Boer, R. Bojariu, I. Camilloni, . . . Wang, H. J. (2013). Near-term Climate Change: Projections and Predictability. In T. F. Stocker, D. Qin, G.-K. Plattner, M. Tignor, S.K. Allen, J. Boschung, A. Nauels, Y. Xia, V. Bex, & P. M. Midgley (Eds.), Climate Change 2013: The Physical Science Basis. Contribution of Working Group I to the Fifth Assessment Report of the Intergovernmental Panel on Climate Change (pp. 953–1028). Cambridge: Cambridge University Press.

Krumhardt, K. M., Lovenduski, N. S., Long, M. C., & Lindsay, K. (2017). Avoidable impacts of ocean warming on marine primary production: Insights from the CESM ensembles. Global Biogeochemical Cycles, 31(1), 114-133. DOI: 10.1002/2016gb005528

Kruschke, J. K. (2015). Credibility, Models, and Parameters. Doing Bayesian data analysis: a tutorial with R, JAGS, and Stan (Edition 2. ed.), 15-32. Boston: Academic Press.

Laufkötter, C., Vogt, M., & Gruber, N. (2013). Long-term trends in ocean plankton production and particle export between 1960–2006. Biogeosciences, 10(11), 7373-7393. DOI: 10.5194/bg-10-7373-2013

Laufkötter, C., Vogt, M., Gruber, N., Aita-Noguchi, M., Aumont, O., Bopp, L., . . . Hashioka, T. (2015). Drivers and uncertainties of future global marine primary production in marine ecosystem models. Biogeosciences, 12, 6955-6984. DOI: 10.5194/bg-12-6955-2015

Lavender, S., Jackson, T., & Sathyendranath, S. (2015). The Ocean Colour Climate Change Initiative. Ocean Challenge, 21(1), 29-31.

Law, C. S. (2008). Predicting and monitoring the effects of large-scale ocean iron fertilization on marine trace gas emissions. Marine Ecology Progress Series, 364, 283-288. DOI: 10.3354/meps07549

Lee, Y.-H., and S. J. Haberman (2013), Harmonic Regression and Scale Stability, Psychometrika, 78(4), 815-829. DOI: 10.1007/s11336-013-9337-1.

Levasseur, M. (2013). Impact of Arctic meltdown on the microbial cycling of sulphur. Nature Geoscience, 6(9), 691-700. DOI: 10.1038/Ngeo1910

Levine, A. F. Z., & McPhaden, M. J. (2016). How the July 2014 easterly wind burst gave the 2015-2016 El Nino a head start. Geophysical Research Letters, 43(12), 6503-6510. DOI: 10.1002/2016gl069204

Lewis, K. M., Mitchell, B. G., van Dijken, G. L., & Arrigo, K. R. (2016). Regional chlorophyll a algorithms in the Arctic Ocean and their effect on satellite-derived primary production estimates. Deep-Sea Research Part Ii-Topical Studies in Oceanography, 130, 14-27. DOI: 10.1016/j.dsr2.2016.04.020

Longhurst, A. (1995). Seasonal cycles of pelagic production and consumption. Progress in Oceanography, 36(2), 77-167. DOI: 10.1016/0079-6611(95)00015-1

Longhurst, A. (1998). Provinces: the secondary compartments. Ecological Geography of the Sea, 103-114, San Diego: Academic Press.

Lopez-Urrutia, A., San Martin, E., Harris, R. P., & Irigoien, X. (2006). Scaling the metabolic balance of the oceans. Proceedings of the National Academy of Sciences of the United States of America, 103(23), 8739-8744. DOI: 10.1073/pnas.0601137103

Maritorena, S., d'Andon, O. H. F., Mangin, A., & Siegel, D. A. (2010). Merged satellite ocean color data products using a bio-optical model: Characteristics, benefits and issues. Remote Sensing of Environment, 114(8), 1791-1804. DOI: 10.1016/j.rse.2010.04.002

Maritorena, S., & Siegel, D. A. (2005). Consistent merging of satellite ocean color data sets using a bio-optical model. Remote Sensing of Environment, 94(4), 429-440. DOI: 10.1016/j.rse.2004.08.014

Maritorena, S., Siegel, D. A., & Peterson, A. R. (2002). Optimization of a semianalytical ocean color model for global-scale applications. Applied Optics, 41(15), 2705-2714. DOI: 10.1364/Ao.41.002705

Martinez, E., Antoine, D., D'Ortenzio, F., & Gentili, B. (2009). Climate-Driven Basin-Scale Decadal Oscillations of Oceanic Phytoplankton. Science, 326(5957), 1253-1256. DOI: 10.1126/science.1177012

Martinez, E., Raitsos, D. E., & Antoine, D. (2016). Warmer, deeper, and greener mixed layers in the North Atlantic subpolar gyre over the last 50years. Global Change Biology, 22(2), 604-612. DOI: 10.1111/gcb.13100

McClain, C. R. (2009). A Decade of Satellite Ocean Color Observations. Annual Review of Marine Science, 1, 19-42. DOI: 10.1146/annurev.marine.010908.163650

McClain, C. R., Signorini, S. R., & Christian, J. R. (2004). Subtropical gyre variability observed by ocean-color satellites. Deep-Sea Research Part Ii-Topical Studies in Oceanography, 51(1-3), 281-301. DOI: 10.1016/j.dsr2.2003.08.002

Mcowen, C. J., Cheung, W. W. L., Rykaczewski, R. R., Watson, R. A., & Wood, L. J. (2015). Is fisheries production within Large Marine Ecosystems determined by bottom-up or top-down forcing? Fish and Fisheries, 16(4), 623-632. DOI: 10.1111/faf.12082

Mélin, F. (2016). Impact of inter-mission differences and drifts on chlorophyll-a trend estimates. International Journal of Remote Sensing, 37(10), 2233-2251. DOI: 10.1080/01431161.2016.1168949

Mélin, F., & Sclep, G. (2012), Band Shift Correction (1.0). Ocean Colour Climate Change Initiative (OC_CCI) – Phase One, Plymouth Marine Laboratory. Retrieved From http://www.esa-oceancolour-cci.org/?q=webfm_send/226

Mélin, F., & Sclep, G. (2015). Band shifting for ocean color multi-spectral reflectance data. Optics Express, 23(3), 2262-2279. DOI: 10.1364/Oe.23.002262

Mélin, F., Vantrepotte, V., Chuprin, A., Grant, M., Jackson, T., & Sathyendranath, S. (2017). Assessing the fitness-for-purpose of satellite multi-mission ocean color climate data records: A protocol applied to OC-CCI chlorophyll-a data. Remote Sensing of Environment, 203, 139-151. DOI: 10.1016/j.rse.2017.03.039

Mélin, F., Zibordi, G., & Berthon, J.-F. (2007). Assessment of satellite ocean color products at a coastal site. Remote Sensing of Environment, 110(2), 192-215. DOI: 10.1016/j.rse.2007.02.026

Moore, C. M., Mills, M. M., Arrigo, K. R., Berman-Frank, I., Bopp, L., Boyd, P. W., . . . Ulloa, O. (2013). Processes and patterns of oceanic nutrient limitation. Nature Geoscience, 6(9), 701-710. DOI: 10.1038/Ngeo1765

Moore, G., Våge, K., Pickart, R., & Renfrew, I. (2015). Decreasing intensity of open-ocean convection in the Greenland and Iceland seas. Nature Climate Change, 5, 877–882. DOI: 10.1038/nclimate2688

Nakano, H., Tsujino, H., Hirabara, M., Yasuda, T., Motoi, T., Ishii, M., & Yamanaka, G. (2011). Uptake mechanism of anthropogenic CO2 in the Kuroshio Extension region in an ocean general circulation model. Journal of Oceanography, 67(6), 765-783. DOI: 10.1007/s10872-011-0075-7

Palmer, J. R., & Totterdell, I. J. (2001). Production and export in a global ocean ecosystem model. Deep Sea Research Part I: Oceanographic Research Papers, 48(5), 1169-1198. DOI: 10.1016/S0967-0637(00)00080-7

Pinsky, M. L., & Fogarty, M. (2012). Lagged social-ecological responses to climate and range shifts in fisheries. Climatic Change, 115(3-4), 883-891. DOI: 10.1007/s10584-012-0599-x

Polovina, J. J., Howell, E. A., & Abecassis, M. (2008). Ocean's least productive waters are expanding. Geophysical Research Letters, 35(3), L03618. DOI: 10.1029/2007gl031745

Racault, M. F., Le Quere, C., Buitenhuis, E., Sathyendranath, S., & Platt, T. (2012). Phytoplankton phenology in the global ocean. Ecological Indicators, 14(1), 152-163. DOI: 10.1016/j.ecolind.2011.07.010

Racault, M. F., Sathyendranath, S., Brewin, R. J. W., Raitsos, D. E., Jackson, T., & Platt, T. (2017). Impact of El Niño Variability on Oceanic Phytoplankton. Frontiers in Marine Science, 4(133). DOI: 10.3389/fmars.2017.00133

Raitsos, D. E., Pradhan, Y., Lavender, S. J., Hoteit, I., McQuatters-Gollop, A., Reid, P. C., & Richardson, A. J. (2014). From silk to satellite: half a century of ocean colour anomalies in the Northeast Atlantic. Global Change Biology, 20(7), 2117-2123. DOI: 10.1111/gcb.12457

Raitsos, D. E., Reid, P. C., Lavender, S. J., Edwards, M., & Richardson, A. J. (2005). Extending the SeaWiFS chlorophyll data set back 50 years in the northeast Atlantic. Geophysical Research Letters, 32(6), L06603. DOI: 10.1029/2005gl022484

Reygondeau, G., Longhurst, A., Martinez, E., Beaugrand, G., Antoine, D., & Maury, O. (2013). Dynamic biogeochemical provinces in the global ocean. Global Biogeochemical Cycles, 27(4), 1046-1058. DOI: 10.1002/gbc.20089

Reynolds, R. W., Rayner, N. A., Smith, T. M., Stokes, D. C., & Wang, W. Q. (2002). An improved in situ and satellite SST analysis for climate. Journal of Climate, 15(13), 1609-1625. DOI: 10.1175/1520-0442(2002)015<1609:Aiisas>2.0.Co;2

Richardson, A. J., Walne, A. W., John, A. W. G., Jonas, T. D., Lindley, J. A., Sims, D. W., . . . Witt, M. (2006). Using continuous plankton recorder data. Progress in Oceanography, 68(1), 27-74. DOI: 10.1016/j.pocean.2005.09.011

Rhein, M., Rintoul, S. R., Aoki, S., Campos, E., Chambers, D., Feely, R. A., . . . Wang, F. (2013). Observations: Ocean. In T. F. Stocker, D. Qin, G.-K. Plattner, M. Tignor, S. K. Allen, J. Boschung, A. Nauels, Y. Xia, V. Bex, & P. M. Midgley (Eds.), Climate Change 2013: The Physical Science Basis. Contribution of Working Group I to the Fifth Assessment Report of the Intergovernmental Panel on Climate Change (pp. 255–316). Cambridge, United Kingdom and New York, NY, USA: Cambridge University Press.

Rogelj, J., Meinshausen, M., & Knutti, R. (2012). Global warming under old an new scenarios using IPCC climate sensitivity range estimates. Nature Climate Change, 2(4), 248-253. DOI: 10.1038/Nclimate1385

Rushworth, A., Lee, D., & Mitchell, R. (2014). A spatio-temporal model for estimating the long-term effects of air pollution on respiratory hospital admissions in Greater London. Spatial and Spatio-temporal Epidemiology, 10(Supplement C), 29-38. DOI: 10.1016/j.sste.2014.05.001

Rykaczewski, R. R., & Dunne, J. P. (2011). A measured look at ocean chlorophyll trends. Nature, 472(7342), E5-E6. DOI: 10.1038/Nature09952

Saba, V. S., Friedrichs, M. A. M., Carr, M. E., Antoine, D., Armstrong, R. A., Asanuma, I., . . . Yool, A. (2010). Challenges of modeling depth-integrated marine primary productivity over multiple decades: A case study at BATS and HOT. Global Biogeochemical Cycles, 24, GB3020. DOI: 10.1029/2009gb003655

Sahu, S. K., & Bakar, K. S. (2012). Hierarchical Bayesian autoregressive models for large space-time data with applications to ozone concentration modelling.

Applied Stochastic Models in Business and Industry, 28(5), 395-415. DOI: 10.1002/asmb.1951

Sarmiento, J. L., & Gruber, N. (2006). Carbon cycle. Ocean biogeochemical dynamics, 318-358, Princeton: Princeton University Press.

Sarmiento, J. L., Slater, R., Barber, R., Bopp, L., Doney, S. C., Hirst, A. C., . . . Stouffer, R. (2004). Response of ocean ecosystems to climate warming. Global Biogeochemical Cycles, 18(3). DOI: 10.1029/2003gb002134

Saulquin, B., Fablet, R., Mangin, A., Mercier, G., Antoine, D., & Fanton d'Andon, O. (2013). Detection of linear trends in multisensor time series in the presence of autocorrelated noise: Application to the chlorophyll-a SeaWiFS and MERIS data sets and extrapolation to the incoming Sentinel 3-OLCI mission. Journal of Geophysical Research: Oceans, 118(8), 3752-3763. DOI: 10.1002/jgrc.20264

Schollaert, S. E., Yoder, J. A., O'Reilly, J. E., & Westphal, D. L. (2003). Influence of dust and sulfate aerosols on ocean color spectra and chlorophyll a concentrations derived from SeaWiFS off the U. S. east coast. Journal of Geophysical Research-Oceans, 108(C6), 3191. DOI: 10.1029/2000jc000555

Séférian, R., Bopp, L., Gehlen, M., Orr, J. C., Ethé, C., Cadule, P., . . . Madec, G. (2013). Skill assessment of three earth system models with common marine biogeochemistry. Climate Dynamics, 40(9-10), 2549-2573. DOI: 10.1007/s00382-012-1362-8

Sherman, K., Belkin, I. M., Friedland, K. D., O'Reilly, J., & Hyde, K. (2009). Accelerated Warming and Emergent Trends in Fisheries Biomass Yields of the World's Large Marine Ecosystems. Ambio, 38(4), 215-224. DOI: 10.1579/0044-7447-38.4.215

Siegel, D. A., Behrenfeld, M., Maritorena, S., McClain, C. R., Antoine, D., Bailey, S. W., . . . Yoder, J. A. (2013). Regional to global assessments of phytoplankton dynamics from the SeaWiFS mission. Remote Sensing of Environment, 135, 77-91. DOI: 10.1016/j.rse.2013.03.025

Signorini, S. R., Franz, B. A., & McClain, C. R. (2015). Chlorophyll variability in the oligotrophic gyres: mechanisms, seasonality and trends. Frontiers in Marine Science, 2(1). DOI: 10.3389/fmars.2015.00001

Sournia, A., Chretiennotdinet, M. J., & Ricard, M. (1991). Marine-Phytoplankton - How Many Species in the World Ocean. Journal of Plankton Research, 13(5), 1093-1099. DOI: 10.1093/plankt/13.5.1093

Sravanthi, N., Ali, P. Y., & Narayana, A. C. (2017). Merging gauge data and models with satellite data from multiple sources to aid the understanding of long-term trends in chlorophyll-a concentrations. Remote Sensing Letters, 8(5), 419-428. DOI: 10.1080/2150704x.2016.1278308

Steinacher, M., Joos, F., Frolicher, T. L., Bopp, L., Cadule, P., Cocco, V., . . . Segschneider, J. (2010). Projected 21st century decrease in marine productivity: a multi-model analysis. Biogeosciences, 7(3), 979-1005. DOI: 10.5194/bg-7-979-2010

Steinacher, M., Joos, F., Frolicher, T. L., Plattner, G. K., & Doney, S. C. (2009). Imminent ocean acidification in the Arctic projected with the NCAR global coupled carbon cycle-climate model. Biogeosciences, 6(4), 515-533. DOI: 10.5194/bg-6-515-2009

Stock, C. A., John, J. G., Rykaczewski, R. R., Asch, R. G., Cheung, W. W. L., Dunne, J. P., . . . Watson, R. A. (2017). Reconciling fisheries catch and ocean productivity. Proceedings of the National Academy of Sciences, 114(8), E1441-E1449. DOI: 10.1073/pnas.1610238114

Taylor, K. E. (2001). Summarizing multiple aspects of model performance in a single diagram. Journal of Geophysical Research: Atmospheres, 106(D7), 7183-7192. DOI: 10.1029/2000JD900719

Taylor, K. E., Stouffer, R. J., & Meehl, G. A. (2012). An Overview of Cmip5 and the Experiment Design. Bulletin of the American Meteorological Society, 93(4), 485-498. DOI: 10.1175/Bams-D-11-00094.1

Thomas, M. K., Kremer, C. T., Klausmeier, C. A., & Litchman, E. (2012). A Global Pattern of Thermal Adaptation in Marine Phytoplankton. Science, 338(6110), 1085-1088. DOI: 10.1126/science.1224836

Uz, S. S., Busalacchi, A. J., Smith, T. M., Evans, M. N., Brown, C. W., & Hackert, E. C. (2017). Interannual and Decadal Variability in Tropical Pacific Chlorophyll from a Statistical Reconstruction: 1958-2008. Journal of Climate, 30(18), 7293-7315. DOI: 10.1175/Jcli-D-16-0202.1

Valente, A., Sathyendranath, S., Brotas, V., Groom, S., Grant, M., Taberner, M., . . . Zibordi, G. (2016). A compilation of global bio-optical in situ data for ocean-colour satellite applications. Earth System Science Data, 8(1), 235-252. DOI: 10.5194/essd-8-235-2016

Vantrepotte, V., & Mélin, F. (2011). Inter-annual variations in the SeaWiFS global chlorophyll a concentration (1997–2007). Deep Sea Research Part I: Oceanographic Research Papers, 58(4), 429-441. DOI: 10.1016/j.dsr.2011.02.003

Vichi, M., Manzini, E., Fogli, P. G., Alessandri, A., Patara, L., Scoccimarro, E., . . . Navarra, A. (2011). Global and regional ocean carbon uptake and climate change: sensitivity to a substantial mitigation scenario (vol 37, pg 1929, 2011). Climate Dynamics, 37(11-12), 2551-2551. DOI: 10.1007/s00382-011-1144-8

Vichi, M., Pinardi, N., & Masina, S. (2007). A generalized model of pelagic biogeochemistry for the global ocean ecosystem. Part I: Theory. Journal of Marine Systems, 64(1), 89-109. DOI: 10.1016/j.jmarsys.2006.03.006

Volk, T., & Hoffert, M. I. (2013). Ocean Carbon Pumps: Analysis of Relative Strengths and Efficiencies in Ocean-Driven Atmospheric CO2 Changes. The Carbon Cycle and Atmospheric CO2: Natural Variations Archean to Present (pp. 99-110): American Geophysical Union.

Weatherhead, E. C., Reinsel, G. C., Tiao, G. C., Meng, X. L., Choi, D. S., Cheang, W. K., . . . Frederick, J. E. (1998). Factors affecting the detection of trends: Statistical considerations and applications to environmental data. Journal of Geophysical Research-Atmospheres, 103(D14), 17149-17161. DOI: 10.1029/98jd00995

Wernand, M. R., van der Woerd, H. J., & Gieskes, W. W. C. (2013). Trends in Ocean Colour and Chlorophyll Concentration from 1889 to 2000, Worldwide. Plos One, 8(6), 3766. DOI: 10.1371/journal.pone.0063766

Wikle, C. K., Berliner, L. M., & Cressie, N. (1998). Hierarchical Bayesian space-time models. Environmental and Ecological Statistics, 5(2), 117-154. DOI: 10.1023/A:1009662704779

Wilkie, C. J., Scott, E. M., Miller, C., Tyler, A. N., Hunter, P. D., & Spyrakos, E. (2015). Data fusion of remote-sensing and in-lake chlorophyll(a) data using statistical downscaling. Spatial Statistics Conference 2015, Part 1, 26, 123-126. DOI: 10.1016/j.proenv.2015.05.014

Wolter, K., & Timlin, M. S. (1998). Measuring the strength of ENSO events: How does 1997/98 rank? Weather, 53(9), 315-324. DOI: 10.1002/j.1477-8696.1998.tb06408.x